UNIVERSIDAD DE INVESTIGACIÓN DE TECNOLOGÍA EXPERIMENTAL YACHAY

Escuela de Ciencias Físicas y Nanotecnología

TÍTULO: Physical and Electrochemical Characterization of the Photochemically Growth of Silver Nanoplates on Graphene Oxide.

Trabajo de integración curricular presentado como requisito para la obtención
del título de Ingeniero en Nanotecnología.

Autor:

Lasso López Esteban David

Tutor:

Ph.D – Briceño Araujo Sarah

Urcuquí, Julio 2020

UNIVERSIDAD
YACHAY
TECH

SECRETARÍA GENERAL
(Vicerrectorado Académico/Cancillería)
ESCUELA DE CIENCIAS FÍSICAS Y NANOTECNOLOGÍA
CARRERA DE NANOTECNOLOGÍA
ACTA DE DEFENSA No. UITEY-PHY-2020-00008-AD

A los 30 días del mes de abril de 2020, a las 15:00 horas, de manera virtual mediante videoconferencia, y ante el Tribunal Calificador, integrado por los docentes:

Presidente Tribunal de Defensa	Dra. GONZALEZ VAZQUEZ, GEMA , Ph.D.
Miembro No Tutor	Dra. VARELA SALAZAR, SOLMAR ALEXANDRA , Ph.D.
Tutor	Dra. BRICEÑO ARAUJO, SARAH ELISA , Ph.D.

El(la) señor(ita) estudiante **LASSO LOPEZ, ESTEBAN DAVID**, con cédula de identidad No. **1722630504**, de la **ESCUELA DE CIENCIAS FÍSICAS Y NANOTECNOLOGÍA**, de la Carrera de **NANOTECNOLOGÍA**, aprobada por el Consejo de Educación Superior (CES), mediante Resolución **RPC-SO-13-No.156-2015**, realiza a través de videoconferencia, la sustentación de su trabajo de titulación denominado: **Physical and Electrochemical Characterization of the Photochemically Growth of Silver Nanoplates on Graphene Oxide**, previa a la obtención del título de **INGENIERO/A EN NANOTECNOLOGÍA**.

El citado trabajo de titulación, fue debidamente aprobado por el(los) docente(s):

Tutor	Dra. BRICEÑO ARAUJO, SARAH ELISA , Ph.D.

Y recibió las observaciones de los otros miembros del Tribunal Calificador, las mismas que han sido incorporadas por el(la) estudiante.

Previamente cumplidos los requisitos legales y reglamentarios, el trabajo de titulación fue sustentado por el(la) estudiante y examinado por los miembros del Tribunal Calificador. Escuchada la sustentación del trabajo de titulación a través de videoconferencia, que integró la exposición de el(la) estudiante sobre el contenido de la misma y las preguntas formuladas por los miembros del Tribunal, se califica la sustentación del trabajo de titulación con las siguientes calificaciones:

Tipo	Docente	Calificación
Presidente Tribunal De Defensa	Dra. GONZALEZ VAZQUEZ, GEMA , Ph.D.	9,6
Miembro Tribunal De Defensa	Dra. VARELA SALAZAR, SOLMAR ALEXANDRA , Ph.D.	9,9
Tutor	Dra. BRICEÑO ARAUJO, SARAH ELISA , Ph.D.	9,0

Lo que da un promedio de: **9.5 (Nueve punto Cinco)**, sobre 10 (diez), equivalente a: **APROBADO**

Para constancia de lo actuado, firman los miembros del Tribunal Calificador, el/la estudiante y el/la secretario ad-hoc.

Certifico que *en cumplimiento del Decreto Ejecutivo 1017 de 16 de marzo de 2020, la defensa de trabajo de titulación (o examen de grado modalidad teórico práctica) se realizó vía virtual, por lo que las firmas de los miembros del Tribunal de Defensa de Grado, constan en forma digital.*

LASSO LOPEZ, ESTEBAN DAVID
Estudiante

Dra. GONZALEZ VAZQUEZ, GEMA , Ph.D.
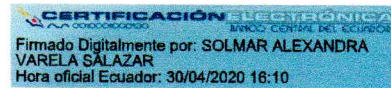**Presidente Tribunal de Defensa**

Firmado electrónicamente por:
GEMA GONZALEZ

Dra. BRICEÑO ARAUJO, SARAH ELISA , Ph.D.
Tutor

Dra. VARELA SALAZAR, SOLMAR ALEXANDRA , Ph.D.
Miembro No Tutor

CIFUENTES TAFUR, EVELYN CAROLINA
Secretario Ad-hoc

AUTORÍA

Yo, **ESTEBAN DAVID LASSO LÓPEZ**, con cédula de identidad 1722630504, declaro que las ideas, juicios, valoraciones, interpretaciones, consultas bibliográficas, definiciones y conceptualizaciones expuestas en el presente trabajo; así cómo, los procedimientos y herramientas utilizadas en la investigación, son de absoluta responsabilidad de el/la autora (a) del trabajo de integración curricular. Así mismo, me acojo a los reglamentos internos de la Universidad de Investigación de Tecnología Experimental Yachay.

Urcuquí, Julio 2020.

Esteban David Lasso López
CI: 1722630504

AUTORIZACIÓN DE PUBLICACIÓN

Yo, **ESTEBAN DAVID LASSO LÓPEZ,** con cédula de identidad 1722630504, cedo a la Universidad de Investigación de Tecnología Experimental Yachay, los derechos de publicación de la presente obra, sin que deba haber un reconocimiento económico por este concepto. Declaro además que el texto del presente trabajo de titulación no podrá ser cedido a ninguna empresa editorial para su publicación u otros fines, sin contar previamente con la autorización escrita de la Universidad.

Asimismo, autorizo a la Universidad que realice la digitalización y publicación de este trabajo de integración curricular en el repositorio virtual, de conformidad a lo dispuesto en el Art. 144 de la Ley Orgánica de Educación Superior

Urcuquí, Julio 2020.

Esteban David Lasso López
CI: 1722630504

Acknowledgments

Resumen

Recientemente, el grafeno oxidado (GO) ha atraído considerable atención dado sus varias aplicaciones en sistemas electroquímicos y como material de soporte para varias nanopartículas metálicas. En este trabajo, reportamos el crecimiento fotoquímico de nanoplatos de plata sobre grafeno oxidado con el uso de dos metodologías: *In-situ y Exsitu*. La síntesis de Nanoplatos triangulares de plata (Ns-TP) sobre GO fue realizado con el uso de un método fotoquímico de reducción modificado utilizando diferentes longitudes de onda de irradiación (440, 540, 650, 200-600 nm). El nanocompuesto Ns-TP/GO fue caracterizado usando: Microscopía electrónica de Barrido (MEB), microscopía electrónica de transmisión (MET), espectroscopía de Raman, espectroscopía UV-vis y voltametría cíclica (VC). Encontramos que las bandas plasmónicas de los Ns-TP pueden controlarse utilizando una longitud de onda específica sin que sea relevante la presencia de GO en la solución. También, los nanoplatos de plata se formaron y depositaron sobre GO para ambas metodologías. Se encontró que el método *In-situ* promueve una distribución de tamaños más homogénea de nanoplatos triangulares. El análisis de Raman mostro un incremento en la señal Raman dado la presencia de plata en el Grafeno. Además, la síntesis *In-situ* revelo que introduce un mayor numero de defectos sobre la superficie de GO (I_D/I_G ratio). Se realizo la deposición electroquímica de Ns-TP sobre un micro-electrodo de grafito en el cual los nanoplatos incrementaron su conductividad y corriente denotando un mayor incremento para los nanoplatos sintetizados con el método In-situ en especial aquellos irradiados con una longitud de onda de 540 nm.

Palabras clave: Nanotecnología, síntesis fotoquímica, nanoplatos de plata, grafeno oxidado.

Abstract

Recently, Graphene Oxide (GO) has attracted considerable attention for various applications involved in electrochemical systems and as a support material for several metallic nanoparticles. In this work, we report the photochemical growth of silver nanoplates on graphene oxide (GO) by the use of a *In-situ* and *Ex-situ* method. The synthesis of Triangular Silver Nanoplates (T-SNPs) on GO was made by using a modified photochemical-reduction method at different irradiation wavelengths (440, 540, 650, and 200-600 nm). T SNPs/GO nanocomposite was characterized using: Scanning Electron Microscopy (SEM), Transmission Electron Microscopy (TEM), Raman spectroscopy, UV-vis spectroscopy, and Cyclic Voltammetry (CV). It was found that plasmonic bands of T-SNPs can be tuned using specific light wavelengths regardless of the presence of GO in the solution. Also, silver nanoplates were formed and deposited on GO for both methodologies. We have also found that the *In-situ* method promotes a narrow size distribution of silver nanoplates. Raman analysis shows an increase in the Raman signal due to the presence of silver and *In-situ* synthesis reveals to introduce more defects to the GO surface (I_D/I_G ratio). The electrochemical deposition of T-SNPs to a graphite micro-electrode increase the conductivity and overall, the silver nanoplates prepared by the *In-situ* method give a higher current on average, especially the ones that were grown by a light source of 540 nm wavelength.

Contents

List of Figures

List of Tables

Chapter 1

Introduction

Silver nanoparticles (AgNPs) and silver-based nanocomposites are of particular interest due to their potentially wide applications as an amperometric sensor, energy storage devices and, catalysis.[1] Nanoparticles, over the years, have been converted into several anisotropic shapes such as nanoprisms, disks, rings, cubes, wires, and rods which have been synthesized through various methods. The optical, electronic, magnetic, and catalytic properties on such nanostructures can be tuned to be distinctive from the properties of the bulk material.[2–5].

Triangular Silver Nanoplates (T-SNPs) are one of many silver anisotropic structures characterized for its narrow thickness and large triangular surface. They are two-dimensional plasmonic nanostructures that have attracted intense attention due to their strong shape-dependent optical properties.[6–9] An extreme degree of anisotropy can be found in these structures which favors a high tunability of their Localized Surface Plasmon Resonance (LSPR) and therefore generates maximum electromagnetic-field enhancement[10]. This is especially true around the tips of the silver triangles where an incident electric field gets amplified. It is now well-established that, by decreasing the size of metallic particles to the nanometer regime, one can alter its properties, however, shape-dependent properties are still not fully understood due to the variety of shapes that exist and the vast number of factors that affects their growth and make replication difficult.[11] It has also been identified that Ag is a highly active electrocatalyst in alkaline solutions for the oxidation of small organic molecules, due to the formation of reactive adsorbed OH species that influence the kinetics of the reaction.[5,12,13] Given the range of applications in which silver is relevant, better control of its properties would have profound economic implications.[14,15]

On the other hand, graphene has been attracting considerable attention for its extraordinary electronic, physical, optical, and magnetic properties[16–18], and also the ability to become a new type of substrate in which to grow and anchor metal nanoparticles for the manufacture of a high-performance optic, electronic, or electrochemical devices.[19–22] Properties of AgNPs could be enhanced by the graphene sheets and regulated by changing the size and density of the deposited AgNPs.[13,16] GO supported metal nanocomposites is a class of hybrid materials that combines the advantages of both graphene electrical properties and active metal nanoparticles which shown extensive applications in many advanced fields such as memory electronic, optoelectronic, transistors, catalysis, energy storage, electrochemical sensors and biosensors.[5,23–25]

The development of nanomaterials has open a gate to built portable and flexible sensors with high sensitivity and selectivity of various compounds. Several techniques have been used to characterize and analyze the formation of GO flakes decorated with AgNPs at different sizes. In the past few years, hybrid materials have been reported to consist of graphene oxide and various nanoparticles, such as gold, platinum, palladium, and so on.[26–29] Nonetheless, there are few works about the composites of Ag and graphene oxide, and most of them are produced by reducing silver salt on graphene oxide by chemical methods.[30,31] Recent works have tried to deposited silver related nanostructures on graphene oxide sheet. For instance, silver nanocrystal has been deposited using an approach that relies on two potential pulses that can independently control the nucleation and subsequent growth processes of AgNPs.[5] Others have growth AgNPs on the surfaces of graphene[30,32,33] using poly(N-vinyl-2-pyrrolidone) as a reductant and stabilizer.[34]

In this work, Triangular Silver Nanoplates/Graphene Oxide nanocomposite (T-SNPs/GO) has been synthesized by two distinct photochemical methods (*Ex-situ* and *In-situ*), using different irradiation light wavelengths to control the size of the T-SNPs, we analyze the effects of GO as a substrate and nucleation site for the growth of silver nanoplates as a function of the wavelength. Here, the electrochemical properties of AgNPs and T-SNPs has been investigated to relate the shape-size dependent properties in processes like oxidation and reduction and their possible applications in their related fields, and also to start a route for the synthesis of such nanocomposite utilizing a photochemical method. It is found that AgNPs were successfully synthetized into T-SNPs using the two proposed methods. Uv-vis spectroscopy shows that AgNPs have been converted in the presence of GO. The Uv-vis spectra of T-SNPs/GO composite have the reported absorption peaks that determine the presence of the nanoplates, and indicates the control acquired in the photochemical method through the use of several light wavelengths of irradiation which control the localized surface plasmon resonance (LSPR) of the mentioned anisotropic silver structures. Additionally, SEM and TEM images suggest that the *In-situ* method promotes a higher yield of silver nanoplates. The Raman analysis of the samples shows that *In-situ* synthesis introduces more defects to the GO surface (I_D/I_G ratio) than the *ex-situ* method. Overall, the *In-situ* samples give a higher current on average indicated by cyclic voltammetry and, especially the highest current was observed by the sample that was irradiated with a light source of 540 nm (green) wavelength. The size-shape dependent properties and the GO presence are discussed and relate to the observation obtained from the different characterization techniques.

1.1   Nanoscience

Nanoscience is the study of phenomena and the manipulation of matter at atomic, molecular and macromolecular scales, where properties differ significantly from those at a larger scale[35]. The importance of nanoscience is that allow the creation of new materials with outstanding properties. These new materials can be design and produce to have numerous advantages in relation with preexisting materials. One of the aim of nanoscience is to replace many scarce non-renewable resources that are utilized in the fabrication of materials with resources that are more abundant, renewable and sustainable. Thus, nanoscience refers to the study and manipulation of matter to create new application that will help to solve problems of our current world as well to open new possibilities of discovery and science.[36] Still, nanoscience is a novel field that is still growing and changing with several areas of research that are still in development, while others are being created with the advance of new techniques for the production and analysis of nanomaterials.
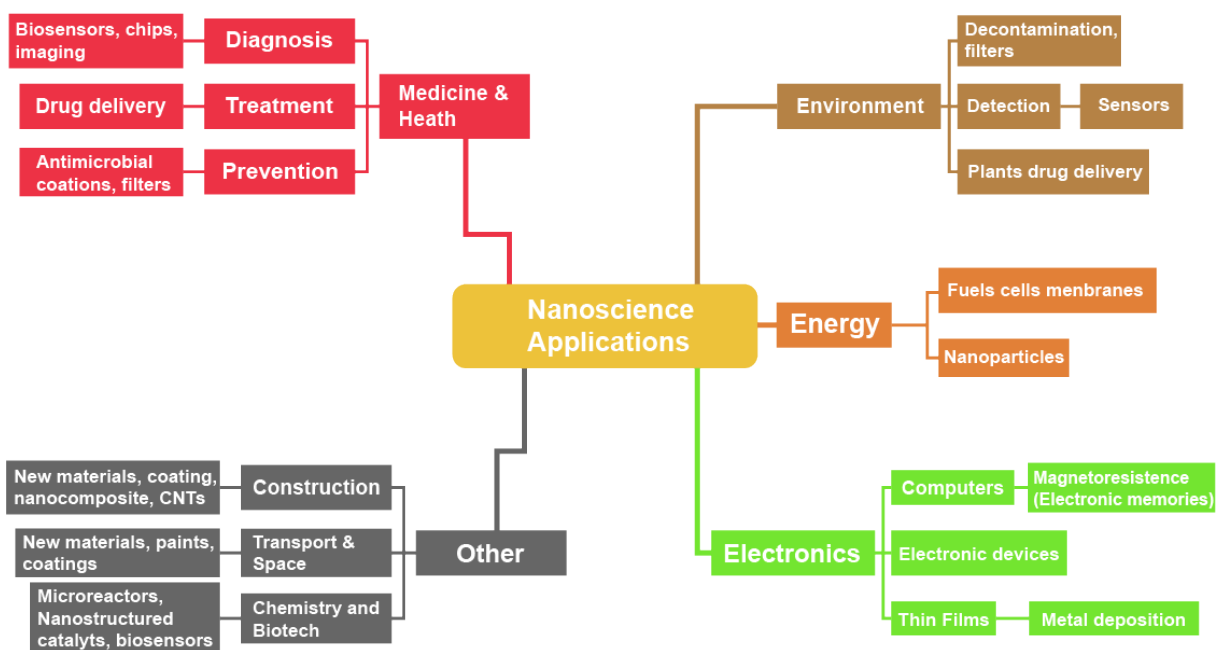
Figure 1.1: Concept map that indicates the several fields in which nanoscience is nowadays applied.

The term "nano" refers to the metric prefix 10^{-9}. The prefix can be ascribed to any unit of measure, which is related to small quantities of any kind. In nanoscience and nanotechnology, nanometers or 10^{-9} m are especially important to describe any effect or phenomena that are found at such scale. Over the years, many applications have

been developed in the branch of nanotechnology, in which many areas are involved (see Figure 1.1). Research is still ongoing, so many other fields should be expected to utilize nanomaterials. For instance, this works is located in the field of chemistry and biotech were nanomaterials are being develop to create microreactors, nanostructured catalysts, biosensors, amperometric sensors and electrochemical sensors. Nevertheless, the materials discussed here can find its route to other areas such as fuel cells and electronic devices.

1.2   Nanomaterials

Nanomaterials describe materials of which at least one of its dimension should be between 1 to 100 nm. This size rage is usually defined as the nanoscale.[37] At this scale, quantum effects are present in the study of properties and structure of a material. These factors determine the properties of a material (strength, heat transfer, conductivity, elasticity, color). Some key attributes are attributed to nanomaterials, such as a grain size on the order of nanometers, a large specific surface area, structural and nonstructural applications with more stronger and more ductile materials which are also chemically active.[35]

In the last years, technology has been escalating very quickly, and the word are starting to be used more often, the word nanomaterial has started to shine in reports and publications. Nanomaterials are not new at all and can be found in everyday lives. For example, nanomaterials exist in nature, in volcanic ashes, sea sprays, and smoke[38]. On the other hand, manufactured nanomaterials have existed as early as the 4th century, also known as the Roman era nanotechnology, were the Lycurgus Cup, a glass cup with tiny proportions of gold and silver nanoparticles was made. The use of nanoparticles was widely spread through many fields like art and even science, and by the 1600s, it was usual for the alchemist to create gold nanoparticles for stained glass.

Nowadays, there are far more usages across many fields; nanomaterials thus represent a growing class of material already introduced into several business sectors. For example, in the early 20th century, tire manufacturers used carbon black in car tires, principally for physical reinforcement (e.g., abrasion resistance, tensile strength) and thermal conductivity to help spread heat load.[39] Then, the invention of the Scanning Tunneling Microscope in 1981 and the further improvements in the years after has allow to reach the sophistication and operation of nowadays machines.[40] The innovations on this area allowed the discovery of materials that were already theorized like fullerenes which were finally discover in 1985[41] Similar discoveries mark the beginning on the current state in nanoscience and start a revolution that led scientists to research nanomaterials in order to understand and control their properties and harness their power.

1.2.1   Graphene (GR)

Graphene (GR) was discovered and isolated in 2004 by A. K. Geim and K. S. Novoselov by a mechanical exfoliation method and is the simplest form of carbon and definitely the thinnest material ever produced. It has one-atom-thick planar sheets of sp^2 bonded carbon atoms densely packed in a honeycomb crystal lattice.[42] Graphene is an excellent electronic material and has been considered as a promising candidate for the post-silicon age. It has a huge potential in the electronic device community, for example, field-effect transistor, transparent electrode. Despite

intense interest and remarkably rapid progress in the field of graphene-related research, there is still a long way to GO for the widespread uses of graphene. It is primarily due to the difficulty of reliably producing high-quality samples, especially in a scalable way, and of controllably tuning the bandgap of graphene.[43] All of its exceptional properties have opened up new avenues for the use of GR in nano-devices and nano-systems. As in any material, the properties of GR comes from its geometrical and electronic structures.
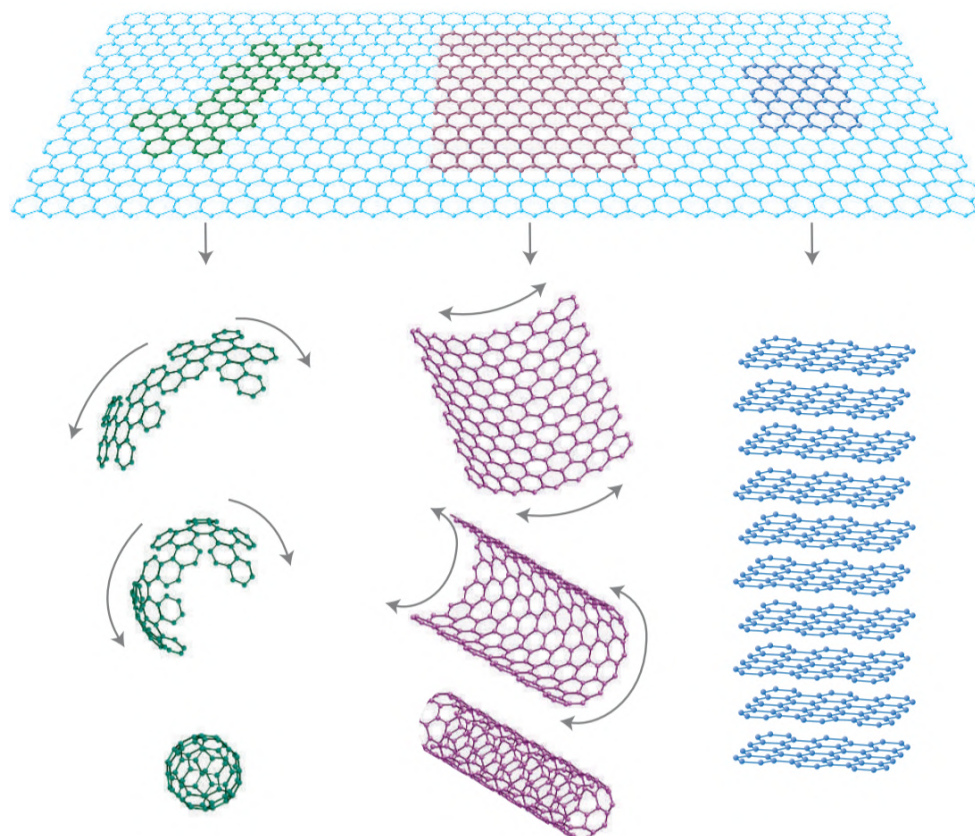
Figure 1.2: Mother of all graphitic forms. Graphene is a 2D building material for carbon materials of other dimensionalities. It can be curve up into 0D buckyballs, rolled into 1D nanotubes or stacked into 3D graphite.[42]

Graphene can also be considered as the parental compound for all the other carbon allotropes of other dimensionalities (Figure 1.2) The wrapping of graphene, introducing curvature in terms of intervening five-membered rings, leads to fullerene. Rolling of graphene segments with different boundaries results in carbon nanotubes of varying chiralities. Three-dimensional graphite can be obtained by the stacking of graphene layers, stabilized by weak van der Waals interactions.[42]

Figure 1.3 show the honeycomb lattice GR were carbon atoms are at the edges of hexagons connected by sp^2 bonds in a plane. The sp^2 interactions result in three bonds called σ-bonds, which are the strongest type of covalent

bond. The σ-bonds have the electrons localized along the plane connecting carbon atoms and are responsible for the great strength and mechanical properties of graphene and Carbon Nanotubes (CNTs). On the other hand, the 2pz electrons form covalent bonds called π-bonds, where the electron cloud is distributed normally to the plane connecting carbon atoms. The 2pz electrons are weakly bound to the nuclei and, hence, are relatively delocalized. These delocalized electrons are the ones responsible for the electronic properties of graphene and CNTs. [44] The ideal graphene sheets that can be achieved by this mechanical exfoliation technique have proven to be: highly ordered, exhibit outstanding surface areas ($2630 m^2\ g^{-1}$), high Young's modulus (1 TPa), high thermal conductivity (5000 W mK^{-1}), strong chemical durability and high electron mobility ($2.5\ 10^5\ cm^{-1}\ V^{-1}\ s^{-1}$). [45]
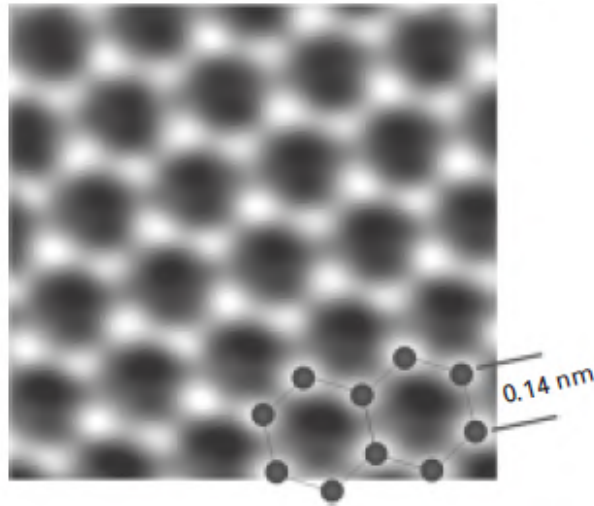
Figure 1.3: Transmission electron microscope image showing the carbon atoms, bonds and, the distant between carbon atom inside the honeycomb lattice. [44]

1.2.2   Graphene: Lattice and Reciprocal Lattice

Graphene has carbon atoms placed at the edges of hexagons, normally know as a honeycomb lattice. The lattice is shown in Figure 1.4 a) using a simplified model where the blue dots represent carbon atoms and the lines joining them indicate the σ-bonds between atoms. The carbon-carbon bond length is approximately $a_{c-c} = 1.42$ Å. The honeycomb lattice can be characterized as a Bravais lattice with a basis of two atoms, indicated as A and B in Figure 1.4 a), and these contribute with a total of two π electrons per unit cell to the electronic properties of graphene.

   The underlying Bravais lattice is a hexagonal lattice and the primitive unit cell can be considered an equilateral parallelogram with side a = $\sqrt{3}a_{c-c} = 2.46$ Å . The primitive unit vectors as defined in Figure 1.4 a) are:

$$\mathbf{a_1} = \left(\frac{\sqrt{3}a}{2}, \frac{a}{2}\right), \quad \mathbf{a_2} = \left(\frac{\sqrt{3}a}{2}, -\frac{a}{2}\right) \tag{1.1}$$

with $|\mathbf{a_1}| = |\mathbf{a_2}| = a$. Each carbon atom is bonded to its three nearest neighbors and the vectors describing the separation between a type A atom and the nearest neighbor type B atoms as shown in Figure 1.4 a) are:
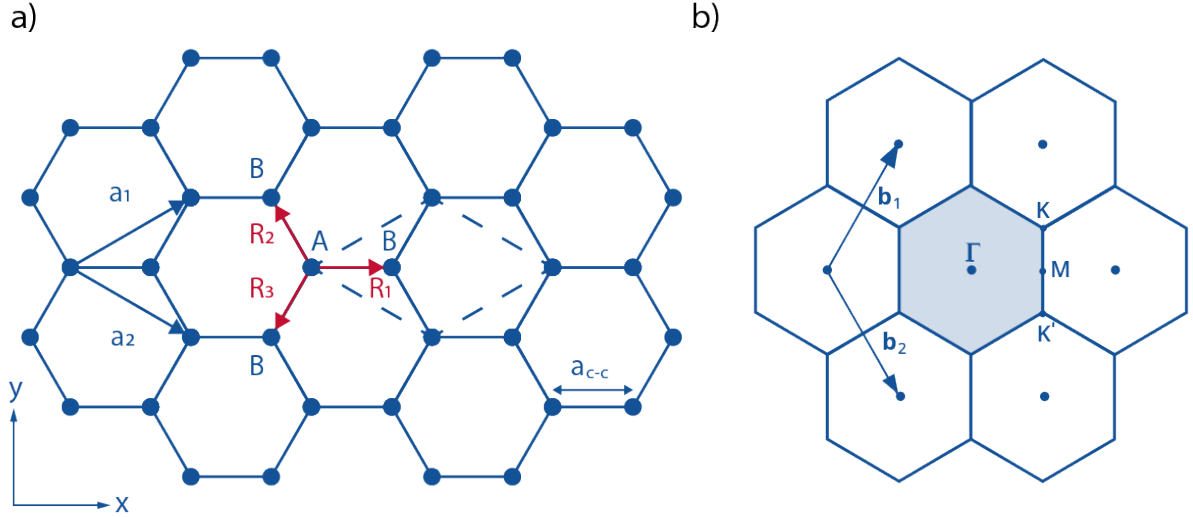
Figure 1.4: a) The honeycomb lattice of graphene. The primitive unit cell is the equilateral parallelogram (dashed lines) with a basis of two atoms denoted as A and B. b) The reciprocal lattice of graphene. The first Brillouin zone is the shaded hexagon with the high symmetry points labeled as Γ, M, and K located at the center, midpoint of the side, and corner of the hexagon respectively. The K'-point, which is also an hexagonal corner (adjacent to the K-point), is essentially equivalent to the K-point for most purposes [44]

$$\mathbf{R_1} = \left(\frac{a}{\sqrt{3}}, 0\right), \quad \mathbf{R_2} = -\mathbf{a_2} + \mathbf{R_1} = \left(-\frac{a}{2\sqrt{3}}, -\frac{a}{2}\right), \quad \mathbf{R_3} = -\mathbf{a_1} + \mathbf{R_1} = \left(-\frac{a}{2\sqrt{3}}, \frac{a}{2}\right) \tag{1.2}$$

with $|\mathbf{R_1}| = |\mathbf{R_2}| = |\mathbf{R_3}| = a_{CC}$.

The reciprocal lattice of graphene shown in Figure 1.4 b) is also a hexagonal lattice, but rotated 90° with respect to the direct lattice. The reciprocal lattice vectors are:

$$\mathbf{b_1} = \left(\frac{2\pi}{\sqrt{3}a}, \frac{2\pi}{a}\right), \quad \mathbf{b_2} = \left(\frac{2\pi}{\sqrt{3}a}, -\frac{2\pi}{a}\right) \tag{1.3}$$

with $|\mathbf{b_1}| = |\mathbf{b_2}| = 4\pi/\sqrt{3}a$. The Brillouin zone, which is a central concept in describing the electronic bands of solids, is shown as the shaded hexagon in Figure 1.4 b) with sides of length $b_{BZ} = |b_1|\sqrt{3} = 4\pi/3a$ and area equal to $8\pi^2/\sqrt{3}a^2$. There are three key locations of high symmetry in the Brillouin zone which are useful to memorize in discussing the band structure of graphene. In Figure 1.4 b), these locations are identified by convention as the

Γ-point, the M-point, and the K-point. The Γ-point is at the center of the Brillouin zone, and the vectors describing the location of the other points with respect to the zone center are:

$$\Gamma M = \left(\frac{2\pi}{\sqrt{3}a}, 0\right), \quad \Gamma K = \left(\frac{2\pi}{\sqrt{3}a}, \frac{2\pi}{3a}\right). \tag{1.4}$$

with $|\Gamma M| = 2/\sqrt{3}a$, $|\Gamma \mathbf{K}| = 4\pi/3a$, and $|M\mathbf{K}| = 2/3a$. There are six K-points and six M-points within the Brillouin zone. The unique solutions for the energy bands of crystalline solids are found within the Brillouin zone and sometimes the dispersion is graphed along the high symmetry directions as a matter of practical convenience. Furthermore, sometimes the reciprocal lattice is refer to the k-space while the vector that locates any point within the Brillouin zone is the wavevector $\mathbf{k}$.

Band Structure and Dirac Cones

It is a triangular lattice with two atoms per unit cell, type A and type B. Hence, the wave function in a unit cell can be written as a vector (ΨA, ΨB) of amplitudes on the two sites A and B. Taking a simple tight-binding model where electrons can hop between neighboring sites one obtains the Bloch Hamiltonian:

$$H_0(\mathbf{k}) = \begin{pmatrix} 0 & h(\mathbf{k}) \\ h^\dagger(\mathbf{k}) & 0 \end{pmatrix} \tag{1.5}$$

with $\mathbf{k} = (k_x, k_y)$ and

$$h(\mathbf{k}) = t_1 \sum_i exp(i\mathbf{k} \cdot \mathbf{a}_i) \tag{1.6}$$

Here a_i are the three vectors in Figure 1.4 , connecting nearest neighbors of the lattice [we set the lattice spacing to one, so that for instance $a_1 = (1, 0)$]. Introducing a set of Pauli matrices σ which act on the sublattice degree of freedom, we can write the Hamiltonian in a compact form as

$$H_0(\mathbf{k}) = t_1 \sum_i \exp\left(\sigma_x \cos\left(\mathbf{k} \cdot \mathbf{a}_i\right) - \sigma_y \sin\left(\mathbf{k} \cdot \mathbf{a}_i\right)\right) \tag{1.7}$$

The energy spectrum $E(\mathbf{k}) = \pm|h(\mathbf{k})|$ gives rise to the famous band structure of graphene, with the two bands touching at the six corners of the Brillouin zone (Figure 1.5). Theoretical models of graphene have successfully predicted its properties. Thus, it is an essential part to understand the observations and interpret the results obtained experimentally.

Graphene show to have a unique structure that can be synthetize by various methods. It is a better conductor of heat and charge than metals due to the symmetry at the K-point in the Brillouin zone which generates the formation of Dirac cones allowing the charge transfer paralell to the plane by transfering electrons throught 2pz orbitals. Also is the strongest and lightest material ever created due to its hexagonal lattice made from the sp^2 hybrization creating σ covalent bonds between carbon atoms in a plane.
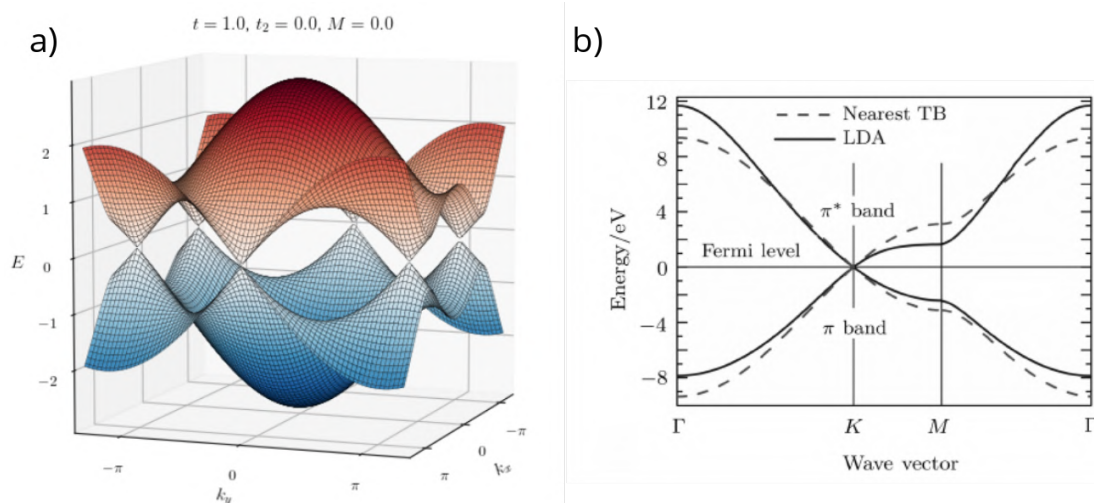
Figure 1.5: a) Only two of these six Dirac cones are really distinct, the ones at $K = (2/3, 2/33)$ and $K = (2/3, 2/33)$. All the others can be obtained by adding some reciprocal lattice vector to K and K',[46] b) The band structure of graphene along three high-symmetry lines. Dashed and solid lines represent the nearest-neighbor tight binding (TB)[47] and local density approximation (LDA).[48]

1.2.3 Graphene Oxide (GO)

Graphene oxide (GO) resembles a single monomolecular layer of graphite (graphene) with various oxygen-containing functionalities such as epoxide, carboxyl, carbonyl, and other hydroxyl groups (Figure 1.6).[49] In contrast, graphene is a 2D crystal made entirely from carbon with outstanding mechanical and electrical properties that exist due to a theoretical perfect lattice. The hexagonal lattice and the location of the three high symmetry points inside the Brillouin zone give graphene its conductive behavior. The presence of the oxygen-containing functionalities and other defects like vacancies reduce the strength and conductivity of the material. Hence, GO can be described as a random distribution of oxidized areas with oxygen-containing functional groups combined with nonoxidized regions where most of the carbon atoms preserve sp^2 hybridization (Figure 1.6).[50] GO can be reduced with a suitable process. The reduced graphene oxide (rGO) formed is almost identical to graphene but contains residual oxygen and other functional groups, as well as structural defects. However, the reduction process can partially restore the GO structures and, in the same way, restore the properties to be more similar to GR. GO, and rGO have been used in polymer composite materials, nanocomposite materials, energy storage, biomedical applications, and catalysis.[51–53] The interest of using GO instead of Graphene rises from two major characteristics: (i) it can be produced using cheaper graphite as the raw material, and by using cost-effective chemical methods with a high yield and (ii) due to its oxygen groups it is highly hydrophilic and can form stable aqueous colloids that allow the assembly of macroscopic structures by simple and cheap solution processes.[50,54] Graphene oxide sheets show elastic modulus of 30-40 GPa, the strength of 120 MPa, and toughness of 0.26 MJ m^3.[55] Similar materials that used reduced graphene oxide

achieved around 40 GPa elastic modulus, 300 MPa of ultimate strength, and higher toughness of 1.22 MJ m^{e3}.[56]
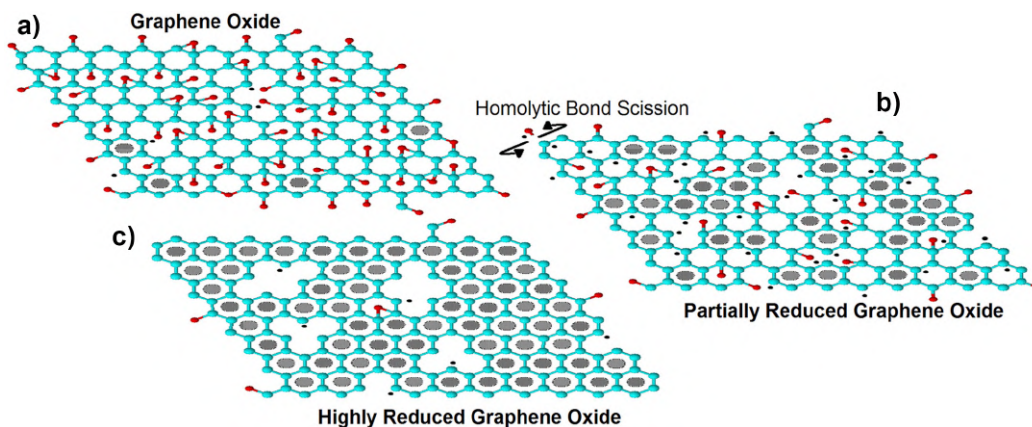
Figure 1.6: a) Illustration of Graphene Oxide (GO) honeycomb lattice containing defects and different oxygen groups. b) Illustration of partially reduced GO (prGO) containing less defects and oxygen groups than GO. c) Highly reduced GO (hrGO) showing the restoration of the hexagonal rings and the elimination of more oxygen groups.

These characteristics have led to a new line of study that focuses its attention to GO instead of GR. Additionally, GO can be doped with other atoms to change or improve its properties, while other approaches focus on the use of other nanomaterials like metallic nanoparticles to improve specific properties of each material. Thus combining their properties and producing nanocomposites that are more feasible to produce and will compensate for the lack of perfect lattices or any other unwanted result produced in the synthesis or fabrication of nano-devices. Graphene oxide sheets can be fabricated by several methods including vacuum-assisted assembly technique[55,57,58] but in general it can be synthesized by either the Brodie,[59] Staudenmaier,[60] or Hummers method,[61] including some variation of these methods. All three methods involve oxidation of graphite to various levels.

1.2.4   Silver Nanoparticles (AgNPs)

Silver nanoparticles (AgNPs) range in size between 1 to 100 nm. They are synthesized by the reduction of silver ions that nucleate and form quasi-spherical nanoparticles (Figure 1.7). Also, AgNPs have attracted increasing interest due to their chemical stability, catalytic activity, localized surface plasma resonance, and high conductivity.[3]. Silver nanoparticles can be produced in different ways, using physical, chemical, photochemical, or biological routes[62]. There are different chemical protocols available to obtain uniform particles with a narrow size distribution at a low cost. All involve a silver precursor such as $AgNO_3$ and a reducing agent like $NaBH_4$, citrate or ascorbate in poly(vinylpyrrolidone) solution.[63,64]
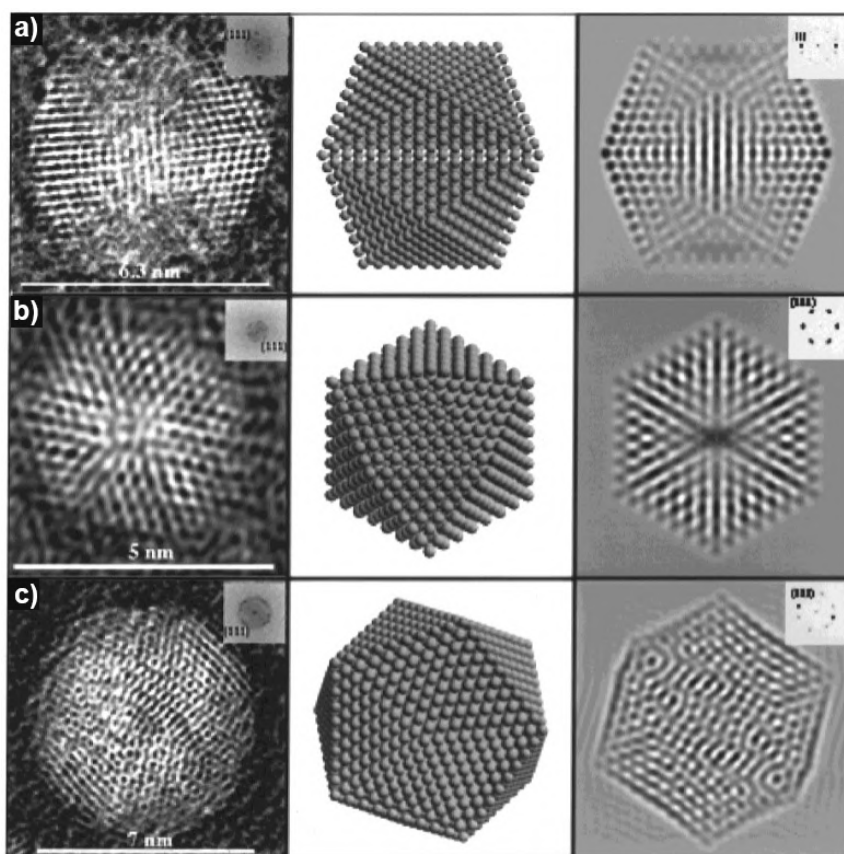
Figure 1.7: Left: High resolution images of icosahedra AgNPs. They were produced at a citrate concentration of 1.5×10^{-4} M. a) a strong pair of (111) reflections and two diffuse pairs of reflections, b) three pairs of (111) reflections, c) five pairs of the (111) family and five weaker pairs of the (200) family of reflections. Middle: ideal models calculated with molecular simulations program Cerius 3.8. Right: multislice calculations.[65]

1.2.5   Formation of AgNPs via Citrate intervention

Trisodium citrate (TSC) is know as a caping agent used to control the shape and size of AgNPs. As describe before AgNPs are obtained from a precursor that typically is a soluble silver salt like $AgNO_3$, and then reduced by a reducing agent. In the reaction, TSC plays an important role as stabilizer where clear yellow solutions are obtained in its presence, whereas gray solutions or precipitated silver results in its absence.[65]
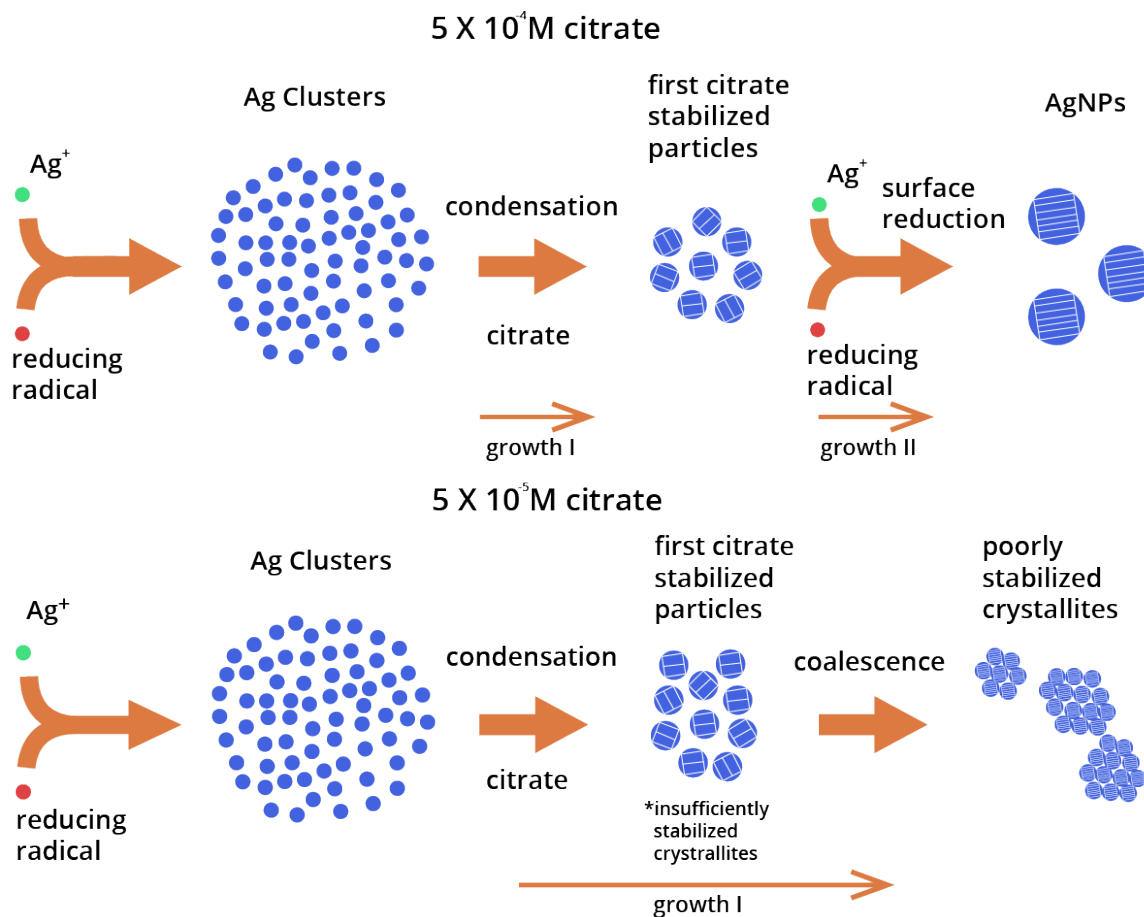
Figure 1.8:   Illustration of important routes of particle growth at two citrate concentrations. At the higher citrate concentration, the stages of nucleation and growth are well separated. At the lower citrate concentration, coalescence reactions of growing particles contribute to particle enlargement.

TSC exerts a drastic effect on the size and size distribution of the silver particles that are formed under otherwise constant conditions, i.e., constant Ag^+ concentration and constant rate of reduction. Concerning the morphology of the silver particles produced, there exists a rather narrow range of TSC concentration of 1.5×10^{-4} M, where

well-separated particles with a narrow size distribution are produced. On the other hand, a low concentrantion in the range of The particles formed at lower TSC concentrations have many imperfections and often consist of several crystallites. At too high TSC concentration, large lumps often are formed because of the coalescence of destabilized particles (Figure 1.8).[65]

1.2.6   Optical Properties-Surface Plasmon Resonance (SPR)

The surface plasmon polariton is a non-radiative electromagnetic surface wave that propagates in a direction parallel to the negative permitivity/dielectric material interface. The electron cloud of the nanoparticles start to oscillate coherently with the wavelength of irradiation causing a temporal dipole around the particle (Figure 1.9). Since the wave is on the boundary of the conductor and the external medium (air, water or vacuum for example), these oscillations are very sensitive to any change of this boundary, for example the adsorption of molecules to the conducting surface.[66] This physical effect is common in metallic nanoparticles, and is produced by the smaller length of nanoparticles in comparision with the wavelength of visible light, which is larger than the length of the diameter of metallic nanoparticles.[65]
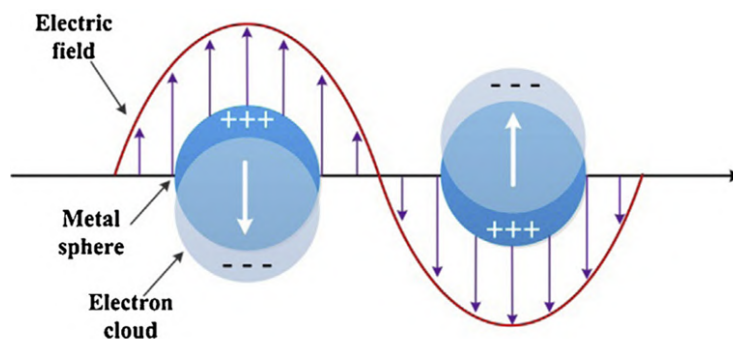
Figure 1.9: Illustration of the excitation of localized surface plasmon resonance.[67]

Due to surface plasmons, metallic nanoparticles have been employed to create SPR sensors where nanoparticles are used in the optical reader of the device. Surface plasmon propagates along a thin metal film and its field probes the medium adjacent to the metal surface. Any change in the refractive index in the proximity of the metal surface results in a change in the velocity of the surface plasmon. This change in the propagation can be determined from the characteristics of the light wave coupled to the surface plasmon. Biorecognition elements specific to analyte molecules are immobilized on the surface of the metal to capture them. The binding gives rise to a refractive index change close to the sensor surface, which can be measured by the optical reader and work as a signal to recognise the type of analyte molecules present in the solution.

1.2.7   Localized Surface Plasmon Resonance (LSPR)

Localized surface plasmon resonances (LSPRs) are collective electron charge oscillations in metallic nanoparticles that are excited by light. They exhibit enhanced near-field amplitude at the resonance wavelength. This field is highly localized at the nanoparticle and decays rapidly away from the nanoparticle/dieletric interface into the dielectric background, though far-field scattering by the particle is also enhanced by the resonance (Figure 1.10). Light intensity enhancement is a very important aspect of LSPRs and its localization means that LSPR has very high spatial resolution (subwavelength), limited only by the size of nanoparticles.[66,68]
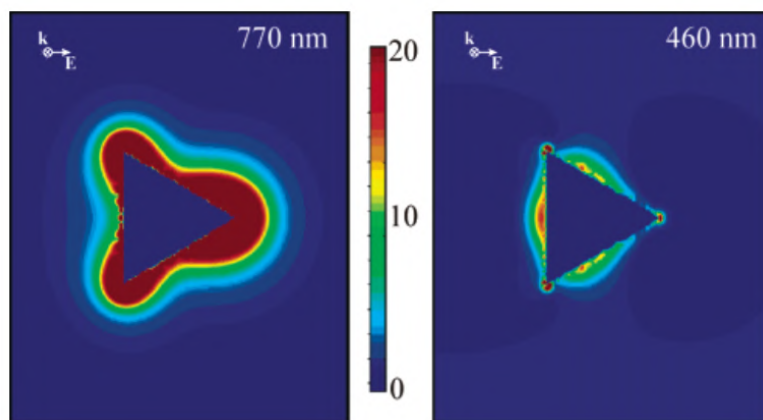
Figure 1.10: E-field enhancement contours external to the Ag trigonal prism, for a plane that is perpendicular to the trigonal axis and that passes midway through the prism. The light is chosen to have **k** along the trigonal axis and **E** along the abscissa. Wavelength of irradiation (Left: 770 nm. Right: 460 nm). Side length = 100 nm, and thickness = 16 nm.[10]

1.2.8   Triangular Silver Nanoplates (T-SNPs)

Silver Triangular Nanoplates (T-SNPs), also referred to as nanoprisms or triangular plates, are two-dimensional plasmonic nanostructures obtained by the controlled reduction of silver ions into the surface of silver nanoparticles.[3] T-SNPs can be easily characterized using TEM since the shape of a triangle in the silver structure is well defined (Figure 1.11). There exist many routes to synthesize T-SNPs, including chemical, electrochemical, and photochemical methods.[2,3,69]

T-SNPs have draw intense attention due to their strong shape-dependent optical properties and related applications.[10] When the aspect ratio of silver nanoplates follows a much larger longitude than the thickness, they possess an severe degree of anisotropy, which favors a high tunability of their LSPRs and therefore generates maximum electromagnetic-field enhancement.[10] There are vital factors that influence the amount of light absorbed/scattered. The first factor is the size of metal nanoparticles. Second is the shape/geometry of nanoparticles that may enhance
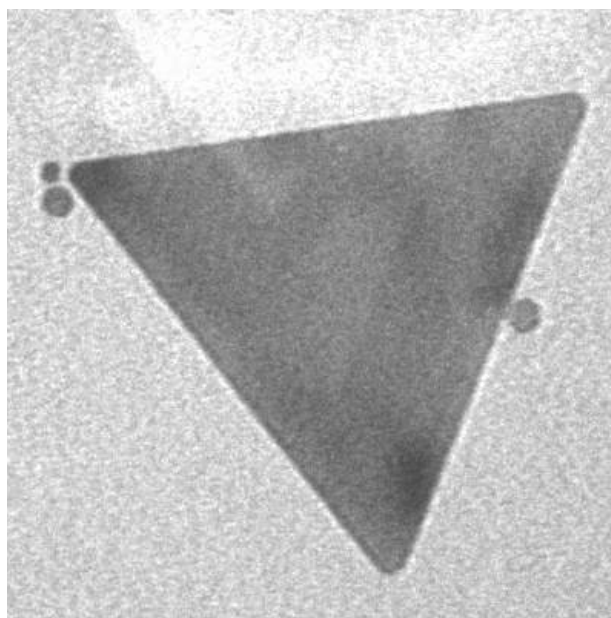
Figure 1.11: TEM micrograph of a T-SNP with some smaller plates at side and edges.

the polarizability at the edges/spikes of the nanostructure. The third factor is the composition of the material, where for instance, Ag will have higher scattering efficiency than Au due to lower Ohmic losses. The fourth factor is the permittivity of the medium around the metal nanoparticle. Tuning the size, shape, composition, and common origin for metal nanostructures enables the utilization of plasmonic nanoparticles via different strategies.

The ability to produce silver (Ag) nanoplates has been a key factor allowing for advancements in the surface enhanced Raman spectroscopy (SERS) and catalysis.[70] In particular, nanodisks (also referred to as nanoplates) constitute a special class of anisotropic structures with highly tunable plasmonic properties, and show promising applicability in many fields such as catalysis, sensing and biomedicine.[15,71,72]

1.2.9   Formation of Triangular Silver Nanoplates and LSPR

Much effort has been made and many hypotheses have been proposed to explain the formation of such highly anisotropic structures. The most accepted theory at the early stages of research was the "face-blocking theory", in which a capping agent selectively binds to a particular crystal facet of the growing nanocrystal and thus reduces the growth rate of that facet relative to the others.[11,20] However, it has been gradually realized that preferential anisotropic growth dependents not only upon the selective adhesion of capping ligands but also on the crystal symmetry of the starting nuclei.[73,74] For the photo-reduction method the mechanism of growth propose that silver ions that are around the nanoparticles in the solution start to reduce by the presence of light and TSC (see Figure 1.12). The process is allow by TSC that acts as an electron donor to the silver ion. After the reduction process TSC is degraded. Other
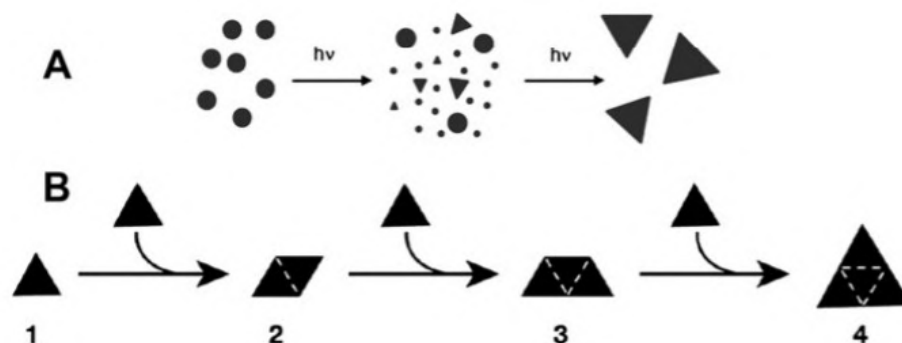
Figure 1.12: Mechanisms proposed for T-SNPs formation through photoinduced aggregation. A) Small silver nanoprisms and clusters are formed and subsequently silver nanoprisms act as seeds for growth whereas the small clusters are digested. B) Light-induced fusion of Ag nanoprisms, where four smaller nanoprisms join together in a stepwise fashion to form one larger nanoprism.

works have confirmed that TSC is not essential to photo-reduce AgNPs[3], however, similar structure-compounds have to be used in order to obtain the same results. The parameters that affect the size and shape are still in debated with different propolsal to explain the relation that exist between the light of irradiation and the final size of the nanoplate (Figure 1.12).

1.2.10   Controlling the size of Triangular Silver Nanoplates via photochemical method

In the photochemical method, several works have reported that the wavelength of irradiation has a direct influence on controlling the size and shape of T-SNPs.[2,10] Larger wavelengths create triangles with larger sides while shorter wavelengths create small triangles.[2] The growth of the nanoplates is controlled by the SPR generated by the incident light. In the beginning, the silver seeds are not in resonance with the irradiated light, e.g.(SPR from silver seed 400 nm and light source 475 nm). In this phase, the growth of the AgNPs is slow until AgNPs grow big enough to be in resonance with the incident wavelength. If the irradiation wavelength is small, e.g.(475nm blue light), the resonance state will be reached much faster. In resonance, SPR is at its maximum, which accelerates the photo-reduction and as consequences the growing process. This phase holds until the nanoparticles reach another size or shape that is no longer in resonance, which finally ends in the stop of the growing process.[75] Thus, AgNPs irradiated with shorter wavelengths not only will grow less but also the growth will happen faster than larger wavelengths.

1.2.11   Nanocomposites

Nanocomposites are heterogeneous materials from which their properties are determined by the same factors as in traditional composites, i.e., component properties, composition, structure, and interfacial interactions.[76] What differentiates nanocomposite materials from classical composites is the degree of control of fabrication, processing,

and performance that can be achieved nearly down to the atomic scale.[77] There exist polymer and non-polymer based nanocomposites. The metal-based nanocomposites are non-polymeric, and they include the use of metallic nanoparticles with other non-polymer material.

Metal-based nanocomposites are characterized by:

- Increased strength and hardness.

- Lesser melting points.

- Super plasticity.

- Increased miscibility of nonequilibrium components in alloying and solid solutions.

- Improved magnetic properties.

- Increased electrical resistivity (because of increased disordered grain surfaces).

Ag-graphene based nanocomposites can be used as efficient biosensors for the detection of biomolecules and bacterial cells. For example, a glucose biosensor (GOD immobilized on AgNPs-decorated functional-SiO_2/GO) with a low detection limit of 310×10^{-6} M but without ideal stability has beem reported[13]. In another work, the long-term stability of fabricated glucose biosensor was unsatisfactory (<5 days) as well. Excitingly, much work has been carried out to improve the stability of biosensor efficiently. In the area of catalysis, graphene nanosheets have been used to obtain Ag/graphene nanocomposite, which was employed as catalysts in the degradation of methylene blue (MB) using sodium borohydride as reductant. In the studies the reaction rate of Ag/graphene nanocomposite was 9.2 times larger than that of Ag nanoparticles colloid (Ag colloid), 34.6 times than that of graphene, indicating the excellent catalysis of the Ag/graphene nanocomposite.[78] Several modified electrodes have been fabricated using Ag-base nanocomposites. Each type of electrode fabricated to be sensible to an specific type of organic molecule or compound, for example, a multifunctional Ag nanoparticles (AgNPs)-polydopamine (Pdop)/graphene (GR) composite was prepared through the oxidation of dopamine on GR at room temperature and subsequent silver deposition by mildly stirring. The modified glassy carbon electrode (GCE) showed enhanced catalytic efficiency towards guanine and adenine oxidation in acetate buffer solution.[79] There exist many physical and electrochemical methods to modified glassy carbon or graphite electrodes. The fabrication complexity depends on which molecule is going to be identify by the sensor. Nevertheless, Ag-GR nanocomposites shows promising results in the area of electrochemical sensors and catalysis without mentioning their other properties that have accomplish to exceed several materials in their related areas.

Chapter 2

Motivation

AgNPs have been studied for several years due to its range of applications.[2,16,74] However, problems like oxidation and agglomeration have decreased its opportunity to be applied in electrochemistry and optical biosensors[2,3] Moreover, the influence of these problems is stronger in anisotropic structures due to LSPR present in sharp edges like nanotriangles, nanoprism, and nanorods. The study and synthesis of anisotropic nanoparticles is becoming more important over the years due to its enhance optical, electrical, and catalytic properties against spherical nanoparticles.[11] For its applications in electrochemistry and optical biosensors[2,3], silver nanoplates should be synthesized with a homogeneous distribution of shapes and sizes.

The synthesis method described here uses LED lights for the photo-coonversion of AgNPs into T-SNPs, thus, providing a low cost and green method. The method also shows great potential for scalability and large-production. Much effort is still needed to understand the photochemical conversion method, to find which variables play a role in the process, and to find the right parameters to control the growth to specific shapes and sizes. Therefore, GO is included in the synthesis provide certain stability to T-SNPs. Several groups have already deposited AgNPs on GO revealing the properties of GO as a support matrix for AgNPs, increasing stability, and improving the electrical and electrochemical properties of the nanocomposite.[16,80,81] T-SNPs/GO can be used in devices like optical and electrochemical biosensors, batteries, and supercapacitors.[13,82,83] The effects of GO in the photochemical reduction process needs to be investigated to determine the parameters that enhance T-SNPs yield and deposition on the GO surface. The research in this regard is crucial for its applications and to improve the properties of the nanocomposite and especially to solve the problems of stability and agglomeration that inhibit the use of this new materials in the industry.

The aim of this graduation project is to study the electrochemical properties of silver triangular nanoplates deposited on graphene oxide (T-SNPs/GO) nanocomposite and relate its shape-dependent properties to the behavior in physical and electrochemical systems. For that, first a characterization of the nanocomposites was done using several physical techniques to determine the final morphology of the synthesized samples. An explanation on the photochemical reduction process and growth of T-SNPs in the presence of GO is included base on the experimental observation to determine the causes of growth and deposition of the silver nanostructures. Later, Raman spectroscopy

is applied to study the optical properties of nanocomposite and determine the interaction between the GO flakes and the silver nanoplates. Finally, cyclic voltammetry was done in a graphite micro-electrode to compare the electrochemical behavior of the different samples and give some insights into the relation between shape-size of the planar silver structures.

2.1   Problem Statement

The photochemical synthesis of T-SNPs/GO nanocomposite by the (*Ex-situ* and *In-situ*) approach using the photo-reduction method at different wavelengths, promotes a higher yield of silver nanoplates on GO. This method improves the electrochemical behavior of the nanocomposite for its potential application as a sensor.

2.2   General and Specific Objectives

- Photochemical synthesis of T-SNPs on GO as a function of the wavelength of the light source.

- Studying the synthesis of T-SNPs/GO by the *Ex-situ* and *In-situ* approach and understanding its effect in the grow process.

- Characterize the nanocomposite by using SEM, TEM, UV-vis spectroscopy, Raman spectroscopy and Cyclic Voltammetry.

- Relate the structural properties with the electrochemical response.

- Studying the effect of GO as a substrate for the stabilization and growth of metallic nanostructures.

Chapter 3

Characterization Techniques

3.1 Electron Microscopy

3.1.1 Scanning Electron Microscope (SEM)
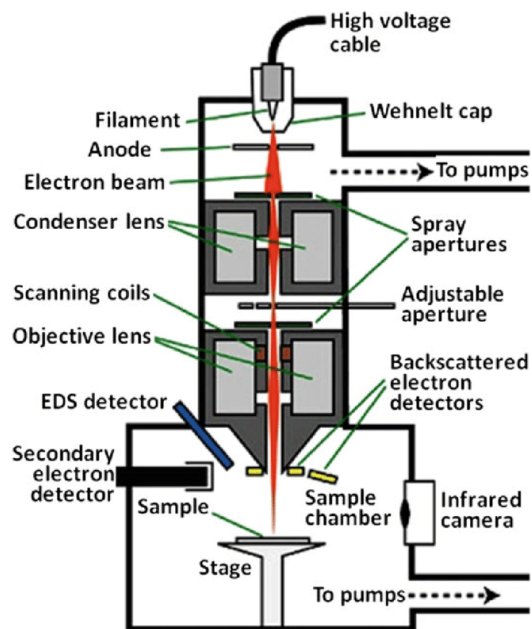
Figure 3.1: Schematics of components from a Scanning Electron Microscope (SEM). [84]

In the SEM, an electron beam is focused and raster-scanned over the sample. When the incident electrons interact

with the sample, several effects take place, such as the emission of secondary electrons. These effects are highly localized to the region directly under the electron beam and can be used to create an image of the sample. Secondary electrons are in special interest when topographic information is required. In addition, elemental analysis through energy dispersive or wavelength dispersive techniques can be done using other detectors. Another effect is the emission of backscattering electrons (BSD) that provides information about compositional contrast from the surface and, to some extent, the bulk of a material.[85] The principal components of SEM are: the electron gun that provide the electrons that will later scatter in the sample, the condensators which are formed by different sets of copper coils that work as electromagnetic lenses which focus the beam of electron into a single spot. Finally the sample chamber contain several detectors depending on the type of electrons that are going to be measure Figure 3.1. All the system operates in high vacuum to avoid accidental scattering of the electrons.

3.1.2   Transmission Electron Microscopy (TEM)
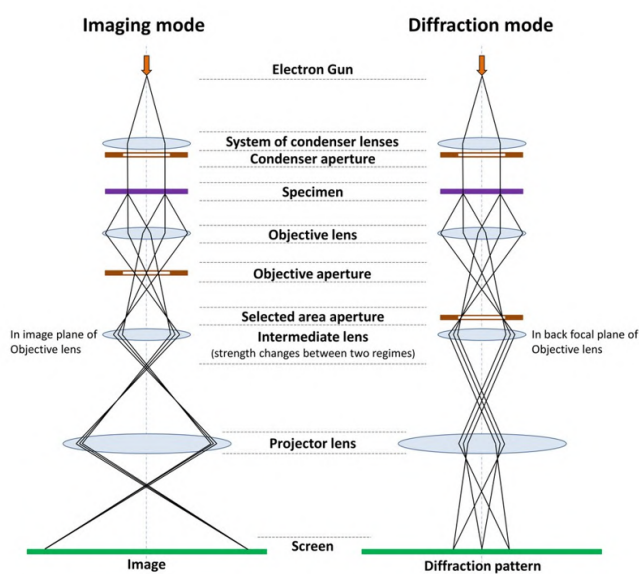
Figure 3.2: Schematics of two modes of operation from an transmission electron microscope (TEM). First one imaging mode, and second diffraction mode.[86]

Transmission Electron Microscopy (TEM) constitutes an essential technique for the characterization of nanomaterials. It is capable of imaging at a significantly higher resolution than light and SEM microscopes, owing to the smaller de Broglie wavelength of electrons. Thus, it enables the instrument to capture fine detail-even as small as a single column of atoms, which is thousands of times smaller than a resolvable object seen in a light microscope.[87] Been able to construct and see images from the nanoscale provides new information about morphology and structure

of material. TEM uses electrons that are provided from an electron gun at the top of the device. The electron gun shoots electrons which later are being aligned with electromagnetic lenses to form a single beam of electrons that will hit the sample. Sample can be moved and tilt respect to the electron beam allowing two observe the samples by two distinct modes called imaging and diffraction (Figure 3.2). In the TEM experiment, a thin or diluted sample has to be prepare to be bombarded under a high vacuum with a focused beam of electrons. TEM instruments boast an enormous array of operating modes, including conventional imaging, Scanning TEM imaging (STEM), diffraction, spectroscopy, and combinations of these. It allows imaging of individual atom columns combined with their spectroscopic analysis. In the imaging mode, electrons are transmitted through the material forming contrast patterns that reproduce the image of the sample. On the other hand, in diffraction mode electrons are treated as waves rather than particles because the wavelength of high-energy electrons is a few thousandths of a nanometer, and the spacing between atoms in a solid is about a hundred times larger, the electrons are diffracted, and the atoms act as a diffraction grating. The diffracted electrons give information about the lattice structure of the material.[87] Also, a diffraction mode is available to study the crystalline structure of a sample.

Scanning transmission electron microscopy is a powerful technique operating at the nanoscale providing qualitative information of a sample. It can be used in several parallel modes to study specific specimen areas: nano diffraction and imaging, X-ray microanalysis, and electron loss spectrometry are of particular interest in the Z-contrast mode, operating under incoherent imaging conditions.

3.2   UV-vis Spectroscopy
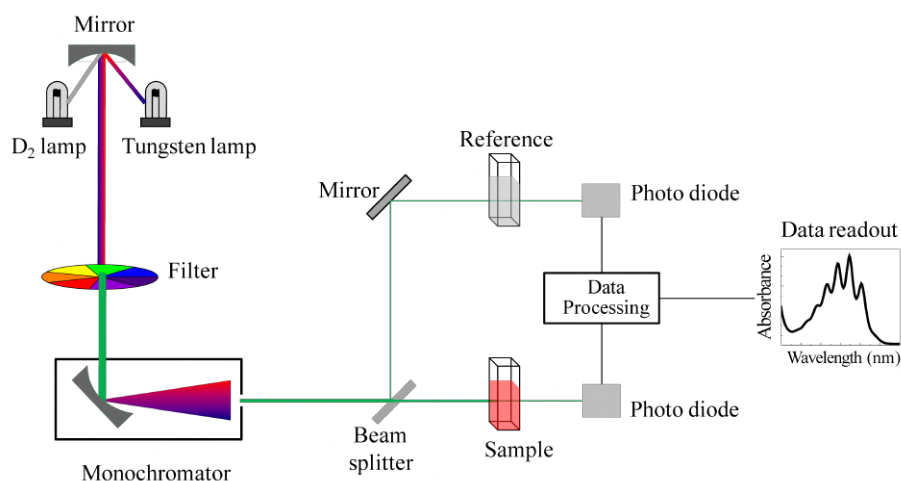
Figure 3.3: Schematics of operation from a UV-vis spectroscope and the tags from the most important components.[88]

UV-vis spectroscopy is one of the oldest methods in molecular spectroscopy. The definitive formulation of the Bouguer-Lambert Beer law in 1852 created the basis for the quantitative evaluation of absorption measurements

at an early date. This step led firstly to colorimetry, then to photometry, and finally to spectrophotometry. This evolution was parallel with the development of detectors for measuring light intensities, from the human eye via the photoelement and photocell, to the photo multiplier and from the photographic plate to the present silicon-diode detector both of which allow simultaneous measurement of the complete spectrum. For a UV-vis measurement, samples have to be preferentially a liquid that goes inside a plastic or quartz cuvette. Other spectrometers exists where a drop of the solution is only required. In both cases, the methodology is straight forward. The UV-vis spectra show an absorbance peak that represents the interaction of the light with the sample.[89]

UV-vis spectroscopy owes its importance, not least to its varied applications in chemistry, physics, and biochemistry where it can be used as a powerful tool to solve analytical problems, to the investigation of chemical equilibrium, and the kinetics of chemical reactions, including photo kinetics. UV-vis spectroscopy uses normally a tungsten lamp that produces light which will be filter or not depending on the experiment. The light will be later scatter using a monochromator and go through the sample after hitting the detector (Figure 3.3). Some equipments require to set a blank before starting the measurements, while other use a beam splitter and a reference to compare the differences between the sample. Regardless of these differences Uv-vis spectroscopy is a potent technique that should be present in any laboratory due to its low cost operation and facile sample preparation.

3.3   Raman Spectroscopy
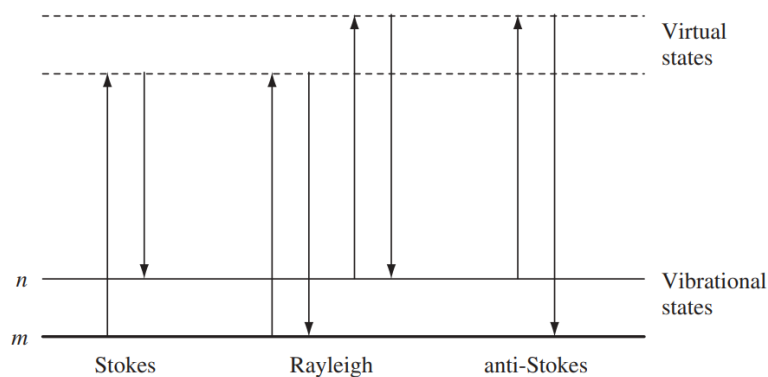
Figure 3.4: Diagram of the Rayleigh and Raman scattering processes. The lowest energy vibrational state m is shown at the foot with states of increasing energy above it. Both the low energy (upward arrows) and the scattered energy (downward arrows) have much larger energies than the energy of a vibration.[90]

Raman spectroscopy is based on the phenomenon of inelastic light scattering. When light interacts with matter, the photons may be absorbed or scattered, or may not interact with the material and may pass straight through it. Special cases occur when the energy of an incident photon is the same to the energy necessary to promote an electron from the ground state of a molecule to an excited state. In this case, the photon may be absorbed, and the molecule

promoted to the higher energy excited state (Figure 3.4). This change is measured in absorption spectroscopy by the detection of the loss of energy radiation from the light. However, it is also possible for the photon to interact with the molecule and scatter from it. In this case, there is no need for the photon to have an energy that matches the difference between the two energy levels of the molecule. The scattered photons can be observed by collecting light at an angle to the incident light beam, and provided there is no absorption from any electronic transitions which have similar energies to that of the incident light, the efficiency increases as the fourth power of the frequency of the incident light.[90]
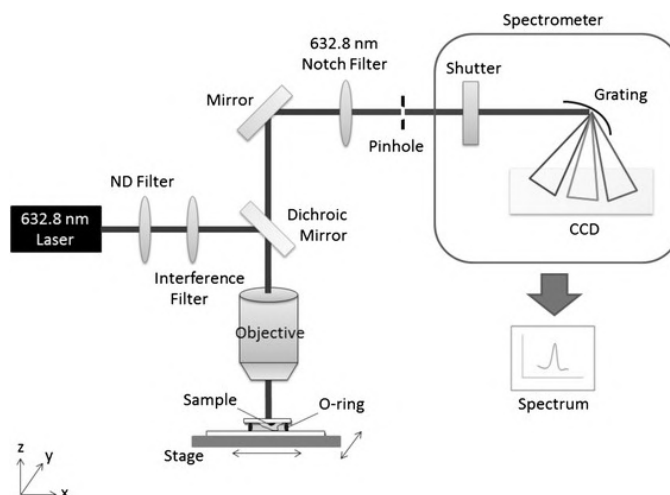
Figure 3.5: Schematics of parts and diagram of operation from a Raman Spectroscope.[91]

Typically, a sample is illuminated with a laser beam, and the electromagnetic radiation from the illuminated spot is collected with a lens and sent it through a monochromator. Elastically scattered radiation at the wavelength corresponding to the laser line (Rayleigh scattering) is filtered out by either a notch filter, edge pass filter, or a bandpass filter, while the rest of the collected light is dispersed onto a detector (Figure 3.4). Spontaneous Raman scattering is typically very weak; as a result, for many years, the main difficulty in collecting Raman spectra was separating the weak inelastically scattered light from the intense Rayleigh scattered laser light (referred to as "laser rejection").[92]

Raman spectroscopy is known as a non-destructive technique to characterize graphite materials, in particular to determine the defects and the ordered and disordered structures of graphene. Normally, the Raman spectra of powdery GO displays two prominent peaks at 1356 and 1596 cm^{-1}, corresponding to the well-documented D and G band. The Raman spectra of the obtained RGO also shows both D and G bands at 1347 and 1596 cm-1 with comparable D/G intensity ratios to that of powdery GO, which suggests that the skeleton structure of GO remains in the RGO. Also, the G line represents the in-plane bond stretching motion of the pairs of C sp^2 atoms (the E_{2g} phonons); while the D line corresponds to breathing modes of rings or j-point phonons of A_{1g} symmetry[93].

3.4   Cyclic Voltammetry
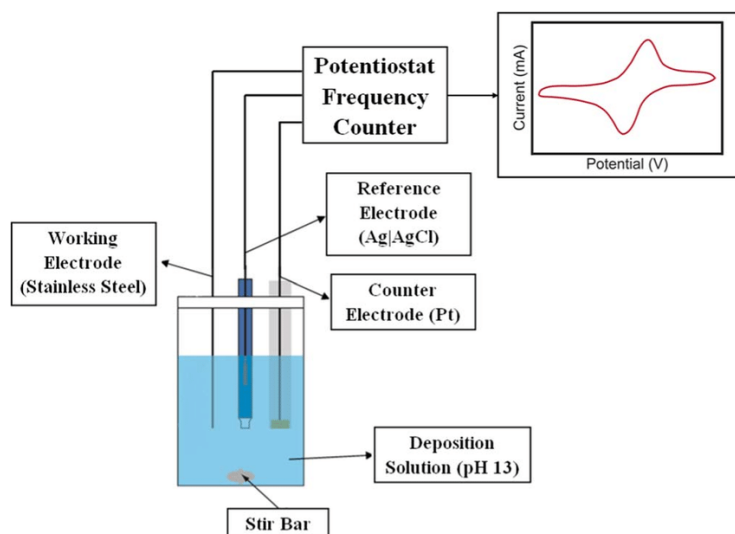
Figure 3.6: Schematics of operation from a Potenciostat to obtain a CV curve.[94]

Cyclic voltammetry (CV), is a reversal technique and potential-scan equivalent of double potential step chronoamperometry. It is obtained by measuring the current at the working electrode during the potential scans. Cyclic voltammetry has become a prevalent technique for initial electrochemical studies of new systems and has proven very useful in obtaining information about fairly complicated electrode reactions.[95] CV is also invaluable to study electron transfer-initiated chemical reactions, which includes catalysis.

A CV system consists of an electrolysis cell, a potentiostat, and a data acquisition system (Figure 3.6). The electrolysis cell consists of a working electrode, counter electrode, reference electrode, and a electrolytic solution (Figure 2.10). To perform a measurement, a specimen is introduced in the cell, where depending on the conditions, an electrolytic solution that acts as a support electrolyte should or not be added. Then, the potential of the working electrode is varied linearly with time, while the reference electrode maintains a constant potential. The counter electrode conducts electricity from the signal source to the working electrode. The purpose of the electrolytic solution is to provide ions to the electrodes during oxidation and reduction.[96][96]

The most common arrangement is the double step technique, in which the first step is used to generate a species of interest, and the second is used to examine it. The last step might be made to any potential within the working range, but usually is employed to reverse the effects of the initial step.

3.4.1   Cyclic Voltammetry Profile

The loop-lines in Figure 3.7 are called cyclic voltammograms. The x-axis represents a parameter that is imposed on the system, here the applied potential (V), while the y-axis is the response, here the resulting current (i) passed. The
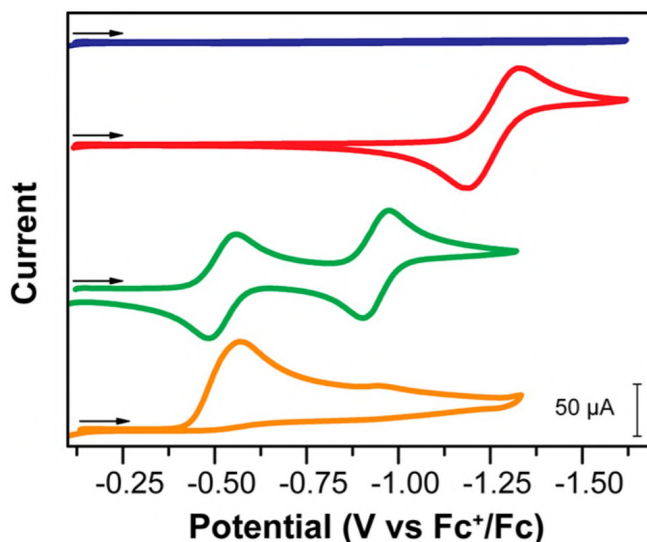
Figure 3.7: Voltammograms of a bare electrode under N_2 (blue trace); a bare electrode under air (red trace); [CoCp(dppe)(CH$_3$CN)](PF$_6$)$_2$ (dppe = diphenylphosphinoethane) under N_2 (green trace); [CoCp-(dppe)(CH$_3$CN)](PF$_6$)$_2$ under air (orange trace). Voltammograms recorded in 0.25 M [NBu$_4$][PF$_6$] CH$_3$CN solution at v = 100 mV/s with a 3 mm glassy carbon working electrode, a 3 mm glassy carbon counter electrode, and a silver wire pseudoreference electrode.[97]

current axis is sometimes not labeled (instead a scale bar is inset to the graph). Each loop-line contains an arrow indicating the direction in which the potential was scanned to record the data. The arrow indicates the beginning and sweep direction of the first segment (or "forward scan"), and the caption indicates the conditions of the experiment. A crucial parameter can be found in the caption of Figure 3.7: "v = 100 mV/s" . This value is called the scan rate (v). It indicates that during the experiment the potential was varied linearly at the speed (scan rate) of 100 mV per second.[97]

3.4.2 CV Importance and Applications

Cyclic voltammetry is a powerful electrochemical technique usually employed to study the reduction and oxidation processes of molecular species. When electron transfers occur and are coupled to chemical reactions, cyclic voltammetry can provide kinetic and mechanistic data. In many cases, these coupled reactions can be related to a unique sort of mechanism that has been previously illustrated, for example, a careful examination of a voltammogram can assist in diagnosing which homogeneous reaction mechanism is happening as well as the kinetics of these reactions. Several chemical reactions can give rise to voltammograms more intricate than the data seen for simple, reversible, one-electron transfer reactions. In the simplest cases, the voltammogram is changed by slow electron transfer or multielectron transfers, and CV can provide useful information for these pure electron transfer reactions.[98–100] Quan-

titative electrochemical analysis is a robust tool for exploring the electron transfer reactions putting groundwork for renewable energy technologies and essential mechanistic inorganic chemistry. Emerging investigators have an increasing interest to utilizing electrochemistry for the advance of their research due to the easy and straight forward methodology, inexpensive equipment, and the vast resource of data available to understand and use this technique.

Chapter 4

Methodology

4.1 Chemicals

Hydrogen peroxide (H_2O_2) 30 wt%, Trisodium citrate (TSC) 99% and Ammonium hydroxide (NH_4OH) 28 wt% were purchased at M&M representations. Silver nitrate ($AgNO_3$) 99%,Sodium borohydride ($NaBH_4$) 98% and Polyvinyl alcohol (PVA) were purchased from Sigma Aldrich. All chemicals were used as received. GO powder was obtained from Abalonyx Innovative Material with a C/O atomic ratio = 3.5-2.6.

4.2 Preparation of GO solution

GO was dispersed in distilled water to reach a concentration of 0.1 wt%. 13 mg of GO was weighed and mixed with 9.9 ml of distilled water. Later 100 μL of PVA (1wt%) were added to the solution. GO was sonicated at room temperature for a one hour till a homogeneous dispersion was visible noticing a brown color in the solution.

4.2.1 Wet chemical synthesis of silver nanoparticles

To perform the chemical synthesis, the following solutions were prepared: 10 mL $AgNO_3$ (0.05M), 10 mL TSC (75mM), 10 mL $NaBH_4$ (100mM). Hydrogen peroxide solution was used as received.
In a typical reaction, 29.35 mL of demineralized water was put into a 50 mL beaker. Then, 150μL of $AgNO_3$ and 400μL of TSC were added and vigorously stirred for 3 min. Then, 4μL of $NaBH_4$ was rapidly added, leading to a light yellow solution. After 2 min of stirring, 60μL of (H_2O_2) was added, converting the yellowish solution to a colorless one. Finally, 250μL of $NaBH_4$ was rapidly injected, leading to a fast change in colors that ended up in orange coloration. This final solution will be further referred to as a "seed" solution (Figure 4.1).
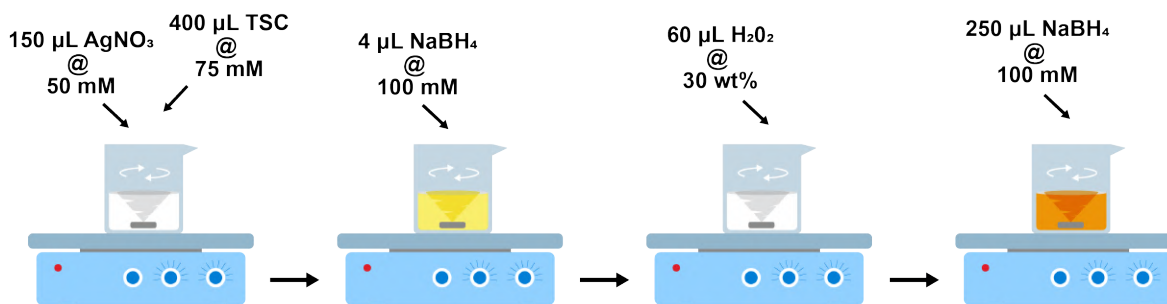
Figure 4.1: Wet chemical synthesis of silver "seeds"

4.3   Light cameras chambers fabrication

High power LED chambers were designed, taking into account the procedure done by Saade.[2] High power LEDs (5W) were used as the light source for the photoconversion. These chambers were made using PVC, aluminum foil, and high power LEDs. Construction materials and LEDs were purchased at a local store. PVC dimensions were 17 cm of longitude and 11.5 cm of diameter. Inside PCV tubes, six high power LEDs (connected in series) were placed equidistant, forming a ring at the bottom of the tube. To avoid external radiation from natural light, an aluminum foil was put at the bottom and top of the PVC tube and secured with tape. Four light chambers were created with a specific wavelength of irradiation. For instance, LED lights of 440 nm (blue), 540 nm (green), 650 nm (red) excitation wavelength was used in the assembling. Also, a warm white (3000 K) LED light was used to perform the photoconversion process.

4.4   Photochemical synthesis of T-SNPs

The photochemical reduction method will be described as a two-step process: wet chemical synthesis of silver nanoparticles and photo-reduction to T-SNPs.

4.4.1   Photo-reduction method

The "seed" solution synthesized in the wet chemical method was divided into five vials. Four of these vials were put inside the LED's chambers, and one was kept at dark as the control sample. The light chambers were connected parallel with a voltage of 5V and a current of 2A with emission centered at 440 nm, 540 nm, 650 nm, and 3000 K white light (Figure 4.2). The initial color of the seed solution was orange, but with some time inside the chambers, the solution starts to change color independence of the wavelength emitted from the LEDs. The samples were irradiated for 18 h in total. All irradiated samples ended with a different color for the solution than the initial orange one (Figure 4.3).
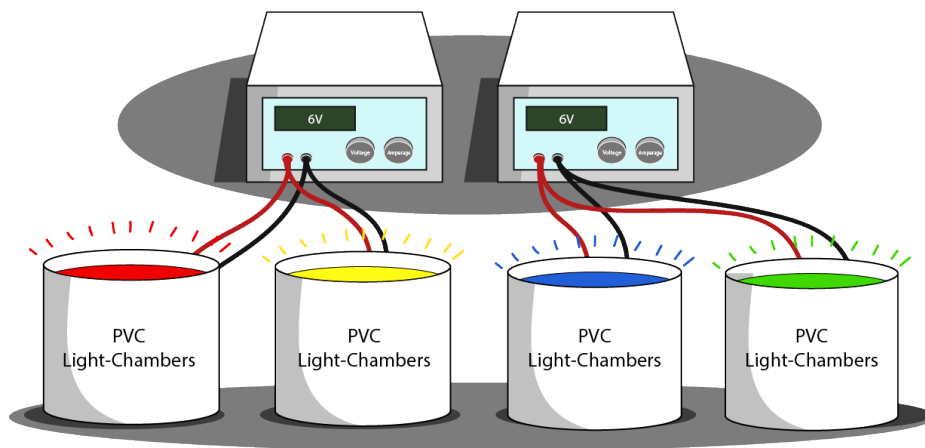
Figure 4.2: High power LED chambers setup. Two chambers were connected in parallel to a power supply.
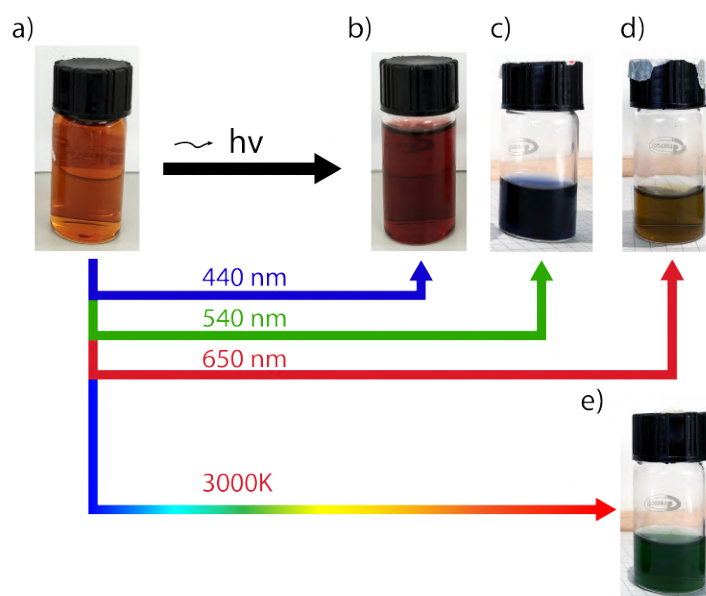
Figure 4.3: Samples prepared by the photochemical method at different wavelengths of irradiation. a) seed solution. b) blue sample irradiated with 440 nm (solution has a reddish color). c) green sample irradiated with 540 nm (solution has a bluish color). d) red sample irradiated with 650 nm (solution has a brownish color). e) white sample irradiated with 3000K warm white light (solution has a greenish color)

4.4.2   Synthesis of *Ex-situ* samples

Samples follow the methodology of the chemical-reduction and four vials of seed solution were prepared, then the vials were placed inside the light chambers (440 nm, 540 nm, 650 nm) and were left there for 18h to complete the photo-reduction process. After the solution change color, the photo-reduction was concluded. For each light source a different color of solution was obtain (Figure 4.3). Then, the new solutions were mixed with 244 μL of the GO solution and with 12,5 μL of NH_4OH. After this process the samples were separate in eppendorfs and stored at room temperature protected from sun radiation or any other light source (Figure 4.4).
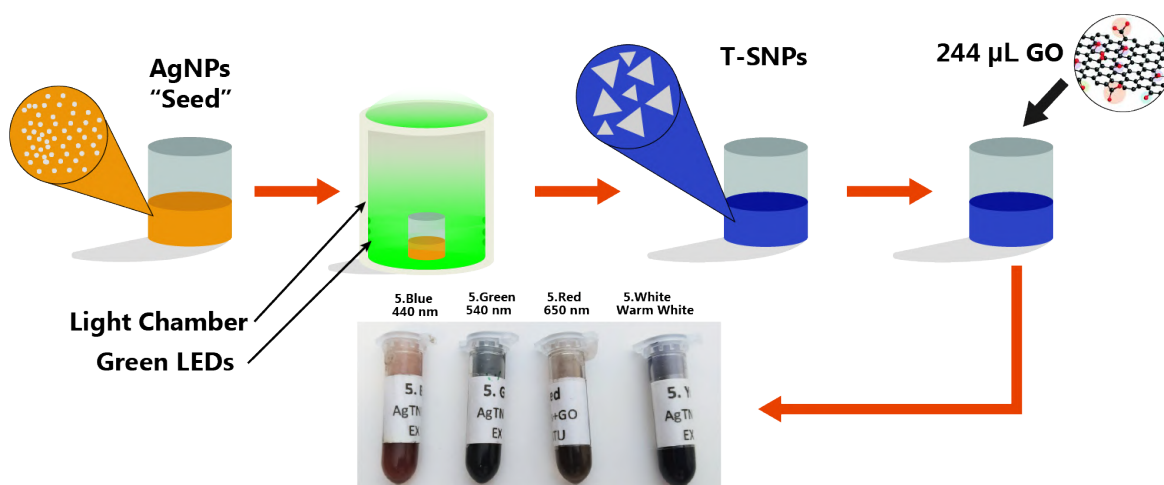
Figure 4.4: *Ex-situ* method and the different samples obtained at different wavelengths.

4.4.3 Synthesis of *In-situ* samples

Seed solution was mixed with 976 μL of the GO solution and, followed immediately by the addition of 50 μL of NH_4OH. Later, this new solution was separated into the four vials (7.5 mL each) and left inside the light chambers for 18h till the photoconversion was completed. Then, the samples were separated in eppendorfs and stored as described for the exsitu method (Figure 4.5).
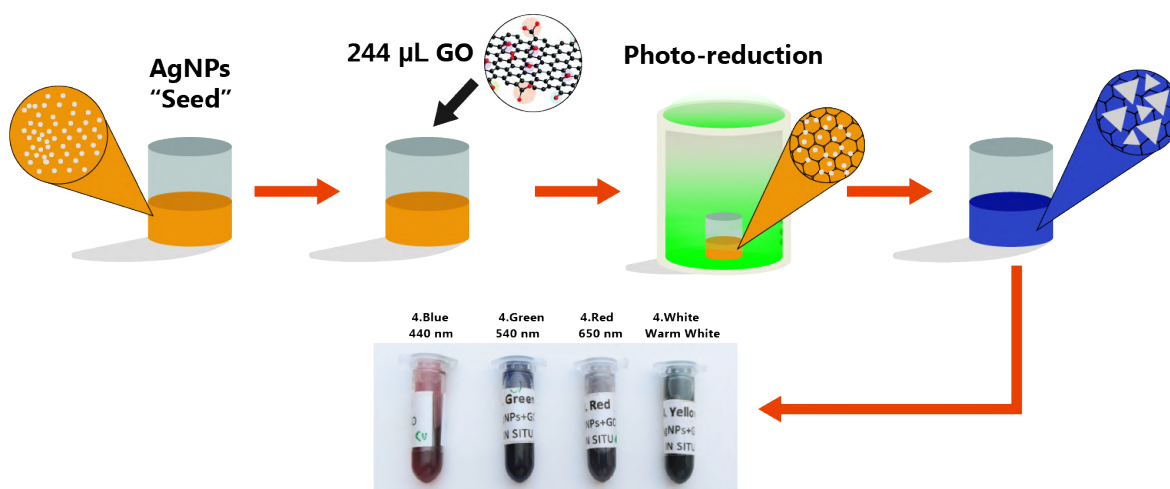
Figure 4.5: *In-situ* method and the different samples obtained at different wavelengths.

4.5 Sample Preparation and Characterization Techniques

4.5.1 UV-vis Spectroscopy

UV-vis spectroscopy was performed in a Horiba NanoLog (Figure 4.6) with a 450 W intense broadband cw xenon lamp for bright excitation from UV to near-IR. All samples were diluted 1:5 with distilled water. All measurements were obtained using a quartz cuvette to avoid signal contamination from polyacrylic cuvettes. Samples before and after CV were measured following the same procedure. The data obtained were analyzed and plotted using Origin Pro software. When storage, samples were kept in the dark to avoid changes due to the photo-reactivity of the samples.

Figure 4.6: Horiba NanoLog UV-vis spectrometer

4.5.2 Scanning Electron Microscopy and Transmission Electron Microscopy
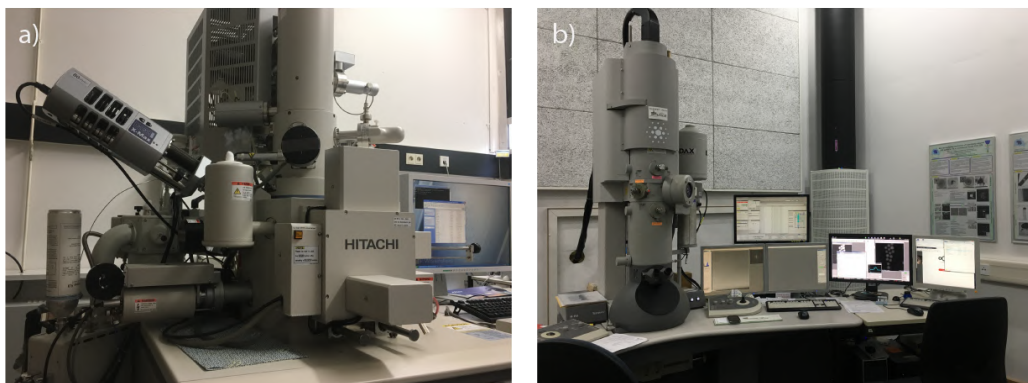
Figure 4.7: a) Hitachi SU8030 (SEM) microscope b) FEI Tecnai G2 (TEM) microscope

SEM images were obtained in a Hitachi SU8030 (Figure 4.7 a) with an accelerating applied potential of 15 kV. Several regions of the samples were analyzed and stored. A drop of the solution was placed in a SiO_2 wafer and left to dry at room temperature. It is necessary to mention that the same samples were also used in Raman spectroscopy with no further modification. TEM images were obtained in an FEI Tecnai G2 transmission electron microscope (TEM) (Figure 4.7 b) with an accelerating applied potential of 200 kV. A drop of T-SNPs/GO composites fabricated by the two methods was put in a carbon-coated copper grid and dried at room temperature. The grid was protected from light and sources of contamination.

4.5.3 Raman Spectroscopy

Raman Spectroscopy was obtained using an Olympus bx51 optical microscope equipped with an XploRA Nano Raman module with three laser green (532nm), red (675nm) and infrared (785nm) (Figure 4.8). The maximum intensities of the laser were 70mW, 28mW, and 30mW, respectively. For the observation and measurement, the samples were prepared in a SiO_2 wafer were a drop of solution was deposited and left to dry at 20°C in a clean environment. The measurements were perform using all the lasers available, however, a description of only the results obtained with the 675 nm laser are shown.
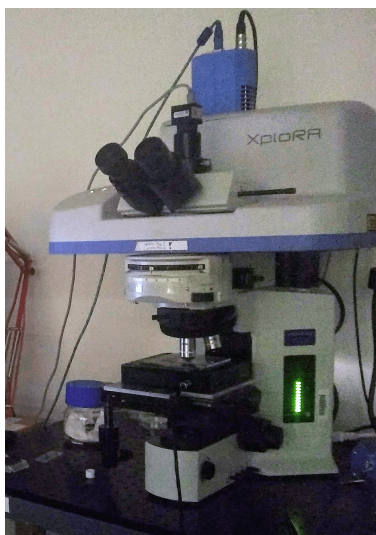
Figure 4.8: XploRA Nano Raman spectrometer

First, an optical microscope was used to locate a region in the sample to perform the analysis. Regions that show low agglomeration of GO flakes were preferred to be measured. In those regions, a grid of 11 by 13 units was created in the software to make a map and collect several spectra from different locations inside the grid for each sample (Figure 4.9). Mapping the region was necessary due to the dispersion of the T-SNPs and the agglomeration of GO flakes. It was necessary to distinguish any enhancement of the Raman signal and, determine the causes that

produces such enhancement. For instance, a higher concentration of GO, the SiO_2 substrate or the presence of silver nanoplates are direct causes that can induce a signal enhancement. Green laser was set to 1% of the total intensity to perform the measurements. From the grid, 12 points were analyzed to obtain 12 spectra of the same region. Then, an average of spectra was calculated to obtain the final Raman spectrum for each sample. The data obtained was analyzed using Horiba LabSpec 6 software, and plots were generated using Origin Pro software.
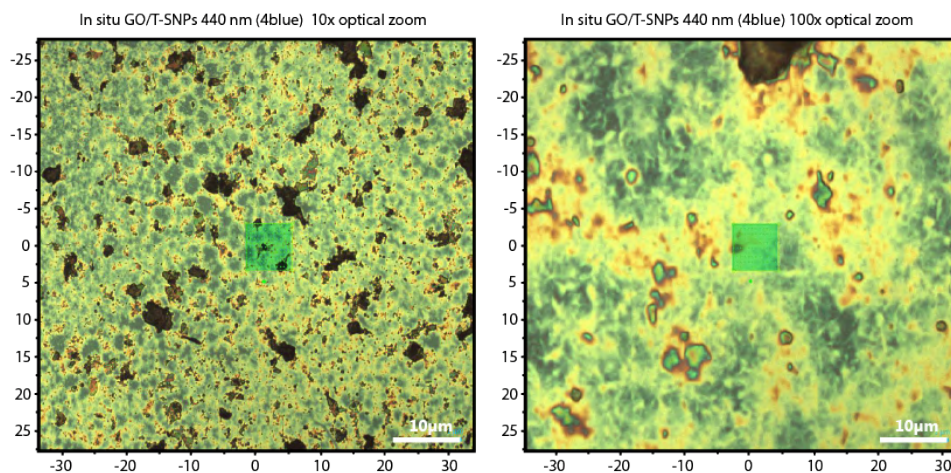
Figure 4.9: Optical image of T-SNPs/GO nanocomposite synthesized with 440 nm irradiation wavelength.

4.5.4 Cyclic Voltammetry (CV)
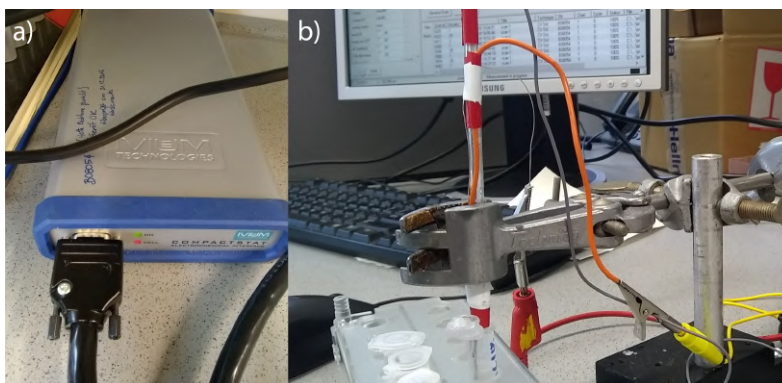
Figure 4.10: a) IVIUM Compactstat. b) Experimental set up. Eppendorf use as microcell with 2 ml of the sample solution.

Cyclic Voltammetry was performed in an IVIUM Compactstat, working in a micro-cell with a three-electrode set-up (Figure 4.10). Ag/AgCl as the reference electrode, Platinum (Pt) wire as the counter-electrode, and graphite pencils leads were used as working electrodes (Figure 4.11). Each Pencil leads was used once to perform calibration, deposition, and measurement. First, the working electrode was conditioned in a H_2SO_4 solution at 0.5M with a sweep potential between -0.5 V to 1.0 V at a scan rate of 500 mV/s. At least 20 sweeps were done to guarantee the graphite stability and homogeneous surface. Next, the electrochemical deposition of T-SNPs/GO to produce the T-SNPs/GRA/GO electrode was done with a sweep potential between 0 V to -1.0 V with a scan rate of 100 mV/s, for this case 25 sweeps were performed to deposit the different samples. After deposition, the modified electrode was measured in a NaCl solution at 1% with sweep potential between -0.5V and 1.0V at a voltage rate of 100mV.
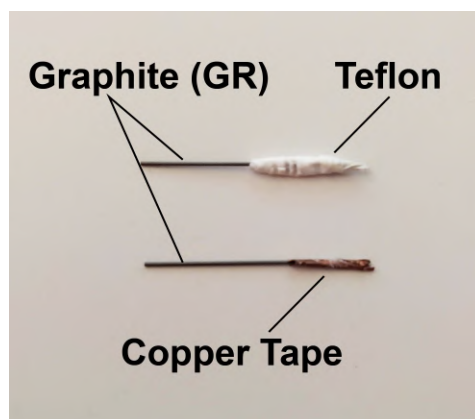
Figure 4.11: Fabricated electrodes use for the electrochemical deposition.

Chapter 5

Results & Discussion

5.1 UV-vis Spectroscopy

The wet chemical synthesis of the silver "seeds" follows a typical synthesis of AgNPs were reagents like $AgNO_3$, TSC, and $NaBH_4$ were used. The procedure is based on a reduction reaction where TSC acts as a stabilizer and capping agent, then NaBH4 reduces silver ions to metallic silver forming AgNPs. After the reduction, quasi-spherical nanoparticles were obtained which show a plasmon peak located at around 400 nm (not shown). The next part of the synthesis is based on the results obtained by Zhang[3] where H_2O_2 was used to increase the degree of anisotropy and increasing the yield of T-SNPs. H_2O_2 is used as an etching agent to promote the formation of planar twinned seeds which are a specific type of metallic nanoparticle that contain [111] twin planes and stacking faults which are key factors influencing particle shape.[21] After the addition of H_2O_2 the yellow solution turn transparent. This observation indicates the oxidation of the quasi-spherical nanoparticles. Later, NaBH4 was added again and the solution turns dark and transparent several times till it reaches a yellowis color that slowly turns orange (Figure 4.3 a). The chemical reaction at this point is complex but what can be expected is a competition between H2O2 and NaBH4 with the oxidant and reductant effect respectively. The resultant solution shows a peak and a shoulder around 500 nm and 650 nm (Figure 5.1 a). The red-shift on the plasmonic band already suggests that H2O2 promotes the formation of anisotropic structures.

On the other hand, the growth process of T-SNPs is based on a seed-mediated approach in which previously formed seeds are irradiated in the presence of Ag^+ and TSC to grow and form nanoplates. The color and plasmon wavelength are changed according to the excitation light. The irradiated silver "seeds" produce colloids with different colors as can be viewed in (Figure 4.3) and the Uv-vis spectra are shown in (Figure 5.1 b). Depending on the sample, several plasmon peaks can be observed each one related to a different LSPR. For example, the sharp and narrow peak in the region 330 and 350 nm correspond to out-of-plane quadrupole plasmon which is particularly important because it confirms the anisotropic nature of the structures since quadrupoles are not observed in spherical metallic nanoparticles.[10]

The next plasmons bands correspond to in-plane dipolar plasmons in which their positions depend, among other
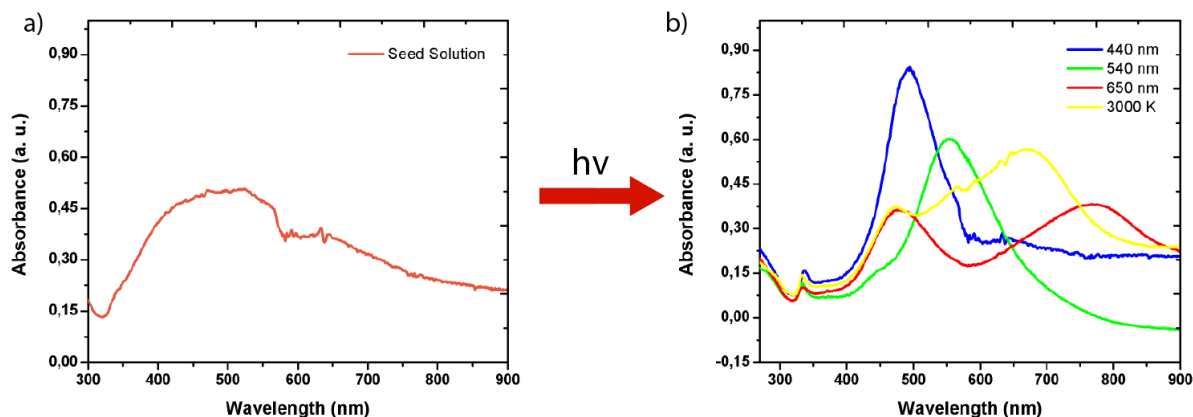
Figure 5.1: (a) UV-vis spectra of the seed solution and (b) irradiated at 440 nm (blue), 540 nm (green), 650 nm (red) and 3000 nm (warm white).

parameters, on particle size, or to be more precise on the ratio between lateral dimension and thickness (aspect ratio). Since the growth is controlled by the excitation light, the dipole plasmons for all the samples appear at regions near the original wavelengths of irradiation. For example, the blue light (440 nm) shows to create a dipole plasmon between 450 and 550 nm, the other lights of irradiation reveal to contribute with a plasmon position around the specific light wavelength. According to other works[2,21] and computational models[10], T-SNPs should be smaller when irradiated with light sources of high frequency and grow larger in the presence of low-frequency lights.
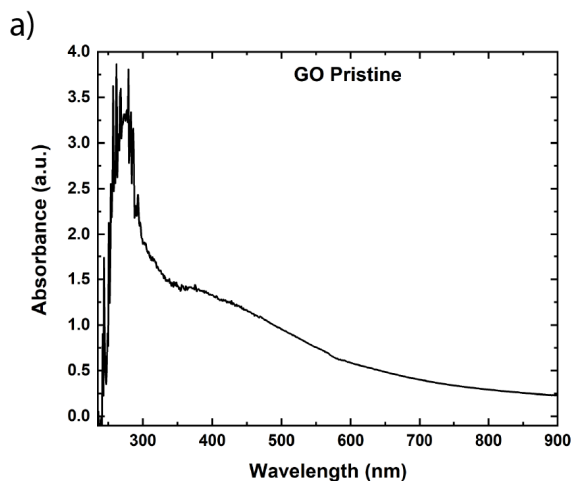
Figure 5.2: a) UV-vis spectrum evolution of AgNPs during 8h of irradition. b) UV-vis spectrum of Graphene Oxide (GO).

UV-vis spectrum of pristine GO solution was measured to have an idea of the initial state of the GO in the solution, and also to discard any not desired effects like contamination or degradation. The Uv-vis spectrum of GO show to be in agreement with the literature with a red shift that could be related to the agglomeration of GO flakes. GO reveals a peak in the region of 250-300 nm that determines the degree of remaining conjugation ($\pi - \pi^*$ transition).[101,102] The shoulder around $\approx$400 nm can be ascribed to the $n - \pi^*$ transition of carbonyl groups Figure 5.2 b). The presence of GO shows to have shifted the dipole plasmon depending on the method studied on this work. This change can be observed in (Figure 5.3) where In-situ samples have their absorption band near the light wavelength of irradiation whereas Ex-situ shows in some cases a shift of the absorption peak related to the dipole plasmon. For instance, in the case of the green and red *Ex-situ* the absorption peaks do not correspond to the wavelength of irradiation. Green *Ex-situ* sample show a large out-of-plane dipole plasmon around 400 - 500 nm. The same peak is observed in the red sample and the white show a shoulder in this region. The in-plane dipole plasmons for the green and red *Ex-situ* samples is red shifted in comparison with the *In-situ* while the contrary observation can be observed for the white *Ex-situ sample*. Nonetheless, the $\approx$ 340 nm peak still appears for both methodologies assuring the anisotropy of the samples. These results suggest that adding Amnonia and GO after the formation of T-SNPs (Ex-situ) is changing the morphology especially in the samples irradiated with a light source of higher wavelengths suggesting that bigger plates are more unstable and may have reacted with GO or NH_3.
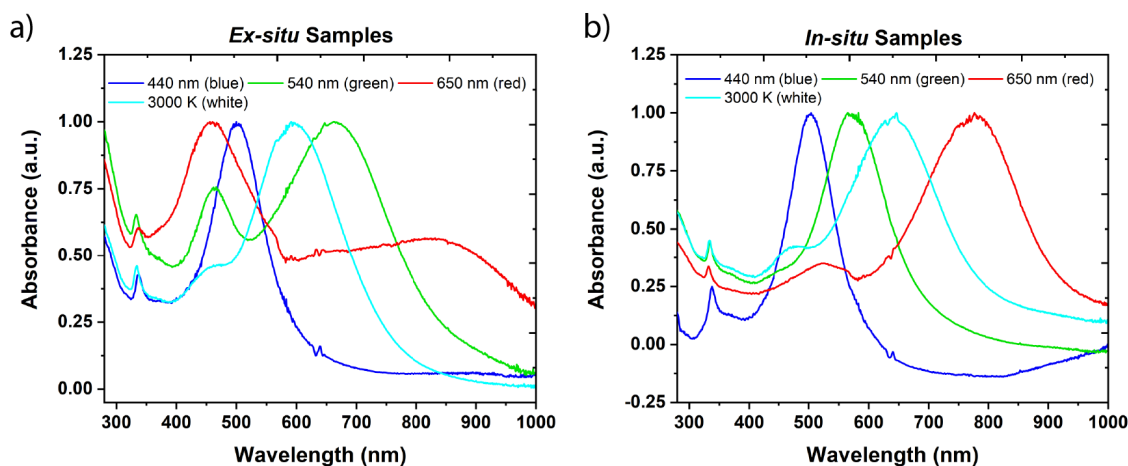
Figure 5.3: UV-vis spectra of T-SNPs/GO after 18 h of irradition. a) *Ex-situ* samples b) *In-situ* samples.

The aim of this study is to find the effects of GO in the photochemical process using the dispersed GO flakes to one-atom-thick flakes are dispersed in solution. The flakes will act as support matrix that will later promote and stabilize the T-SNPs. The UV-vis spectra of the several samples between *In-situ* and *Ex-situ* methods is different; this difference is consistent between all samples that were irradiated with several distinct wavelengths (Figure 5.3). The solutions had the same composition and were irradiated in the same way. Table 5.1 summarized the position of the characteristic peak for all the irradiated samples comparing its position in the UV-vis spectrum. The seed solution

located at 490 nm represent the reference point in which the characteristic peak gets shifted. We can observe that as the wavelength of irradiation increases the characteristic peak gets more red-shifted. T-SNPs produced by the 440 nm light (blue) show no displacement of the absorption peak, however, the absorption peak of T-SNPs/GO by the same light get shifted 10 to 20 nm. It is important to notice, that for T-SNPs/GO the characteristic peak gets more red-shifted for all sample irradiated with a single wavelength, especially in the case of *Ex-situ* samples showing that the addition of GO to the photochemical method has increased the size of nanoplates.On the other hand, the 3000 K LED had the opposite effect where the characteristic peak of T-SNPs/GO is less red-shifted than the sample with only T-SNPs. It is not clear why the 3000 K light produce the opposite effect but the fact that is a light source with multiple wavelengths should be suspect to be the cause of the atypical behaviour.

T-SNPs			
Light irradiation	Out-of-plane quadrupole	Out-of-plane dipole	In-plane dipole
440 nm (Blue)	≈ 340	-	≈ 500
540 nm (Green)	≈ 340	-	≈ 560
650 (Red)	≈ 340	≈ 495	≈ 775
3000 K (White)	≈ 340	≈ 495	≈ 690
T-SNPs/GO *In-situ*			
Light irradiation	Out-of-plane quadrupole	Out-of-plane dipole	In-plane dipole
440 nm (Blue)	≈ 345	-	≈ 500
540 nm (Green)	≈ 345	-	≈ 565
650 (Red)	≈ 345	≈ 530	≈ 650
3000 K (White)	≈ 345	≈ 475	≈ 780
T-SNPs/GO *Ex-situ*			
Light irradiation	Out-of-plane quadrupole	Out-of-plane dipole	In-plane dipole
440 nm (Blue)	≈ 345	-	≈ 500
540 nm (Green)	≈ 345	≈ 455	≈ 665
650 (Red)	≈ 345	≈ 455	≈ 600
3000 K (White)	≈ 345	≈ 455	≈ 850

Table 5.1: Absorption peaks positions of the samples obtained from the UV-vis spectra.

If from the absorption peaks we consider the distance between the points on the y-axis which are half the maximum amplitude and measure the distance between them we obtain what is know as full width at half maximum (FWHM), we can notice that the characteristic peak of *Ex-situ* samples is wider than *In-situ*, indicating a more disperse distribution of sizes and shapes. Also, SPR interactions depend on the size and shape of the particles, if the position of the peaks is shifted, then that implies a direct change in size or shape. These results reveal that

both methods have indeed created T-SNPs, however, the presence of GO in both methods has altered the growth of the silver nanostructures making a more uniform dispersion of sizes while also increasing the sizes of nanoplates regarding pristine T-SNPs, this is demostrated in the higher intensity, shorter FWHM and more red-shifted position of the characteristic peaks from the UV-vis spectrum of the In-situ samples. Many works[3,21] that worked with the photochemical method have reported bimodal distribution of sizes of T-SNPs due to the possible fusion between nanoplates.[4] In this case, the UV-vis spectra of the samples show only one characteristic peak meaning that a unimodal distribution of T-SNPs should be present. Nevertheless, more characterization technique is needed to corroborate these results.

5.2 Electron Microscopy

5.2.1 Scanning Electron Microscopy (SEM)

GO flakes can be distinguished by its crumpled paper look. From the images, several sheets of GO can be observed in Figures 5.4, 5.5, 5,6, 5.7, 5.8, 5.9 and 5.10. The size of GO differ from each sample but an average size of $20\mu m$ can be obtain. The SEM images were acquired using secondary electrons. AgNPs were deposited by all the samples indicating an electrostatic affinity between silver and GO. However, the results not show the presence of T-SNPs and in many ways are variable and do not show any correlation with the light of irradiation, perhabs the sizes difference between samples is small and not visible for SEM.
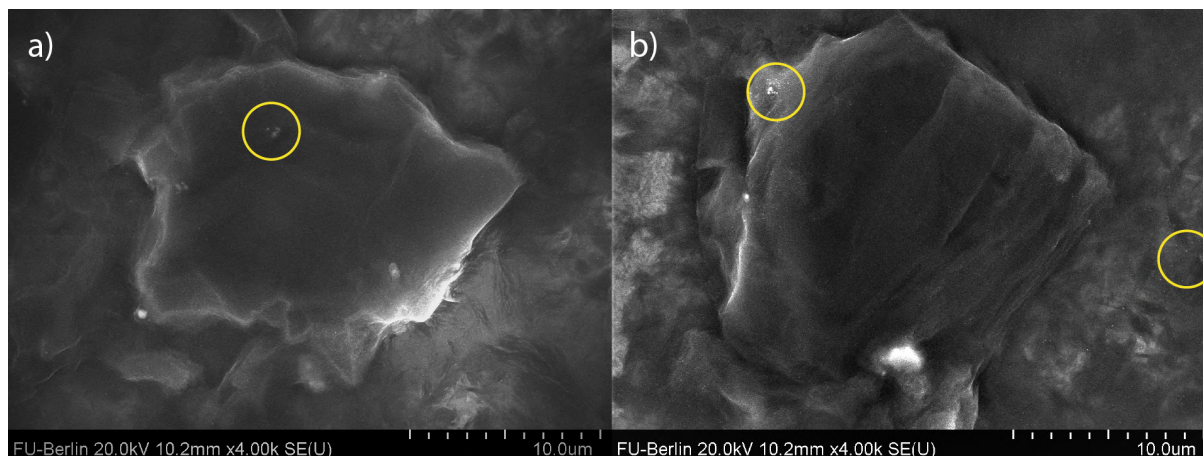
Figure 5.4: SEM images of T-SNPs/GO composite. a) and b) *In-situ* sample irradiated with a 440 nm irradiation light wavelength (blue) Yellow circles indicate regions of silver nanoparticles.

Some samples show larger deposited nanoparticles when the *In-situ* method was applied (Figures 5.7 a and Figure 5.8), but in rest of cases seem to be the other way around. A clear bimodal distribution of sizes can be seen in (Figure 5.8) where T-SPNs are not observed, however anisotropic polyhidral particles are visible in a region of
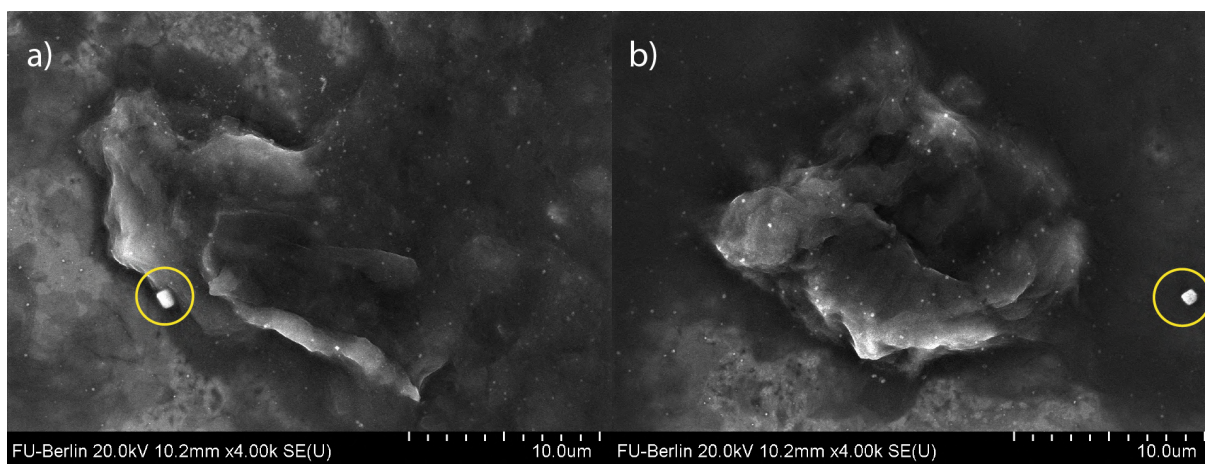
Figure 5.5: SEM images of T-SNPs/GO composite. a) and b) *Ex-situ* sample irradiated with a 440 nm irradiation light wavelength (blue) Yellow circles indicate regions of agglomerates.
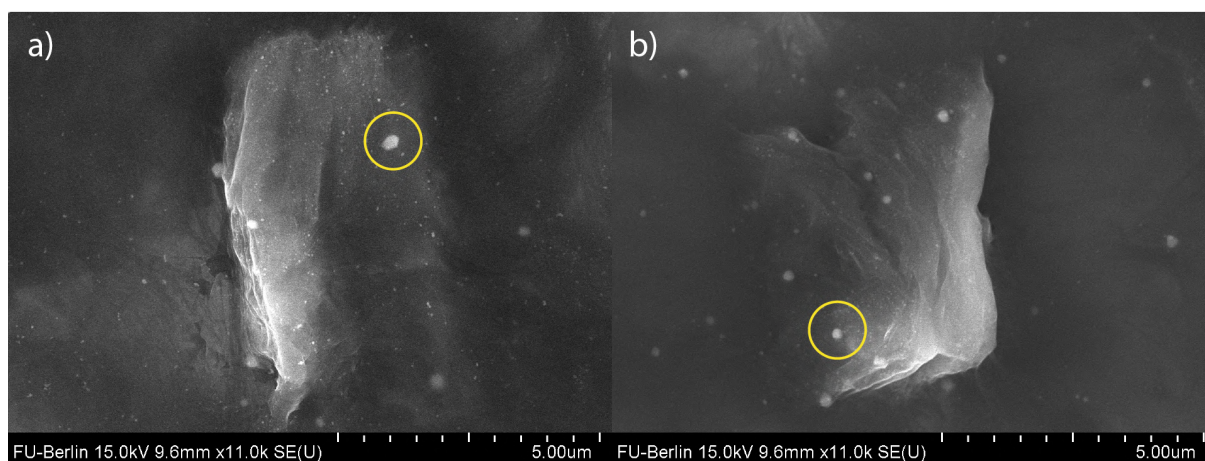
Figure 5.6: SEM images of T-SNPs/GO composite. a) *In-situ* sample irradiated with a 540 nm irradiation light wavelength (green) Yellow circles indicate regions of silver nanoparticles with large size difference. b) *Ex-situ* sample irradiated with a 5400 nm irradiation light wavelength (green).

the GO flake (Figure 5.8 b1), near the same region spherical nanoparticles with a smaller size can be observed. This observation can be applied for the rest samples since similar larger particles are observed surrounded by smaller ones. A particular case of high degree of agglomeration is observed (Figure 5.7 a). It seems difficult to attribute the size difference to the light of irradiation due to the lack of patterns or any sign of T-SNPs. Some samples show on average a difference on size between methods but other samples like the green or red show the opposite. The
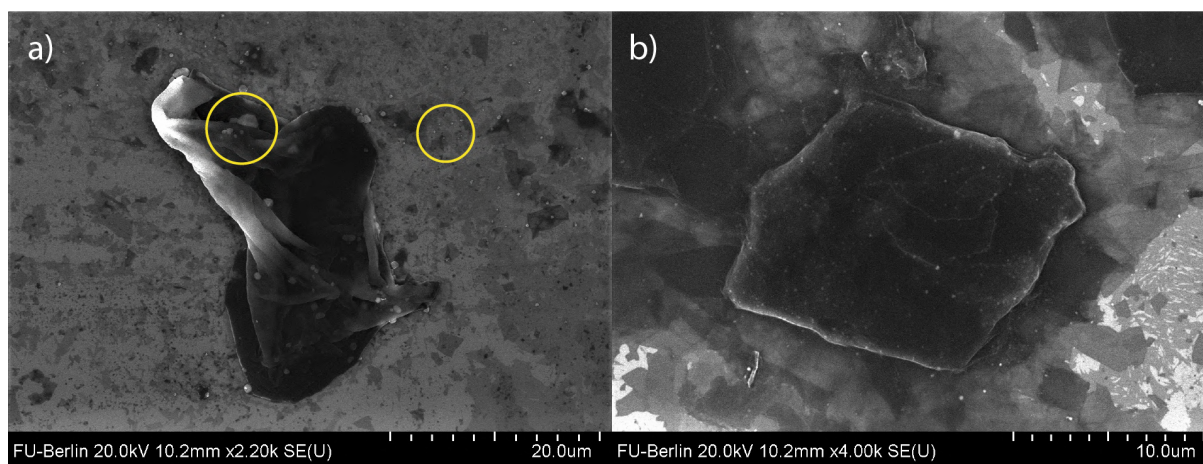
Figure 5.7: SEM images of T-SNPs/GO composite. a) *In-situ* sample irradiated with a 650 nm irradiation light wavelength (red) Yellow circles indicate regions of silver nanoparticles with large size difference. b) *Ex-situ* sample irradiated with a 650 nm irradiation light wavelength (red).
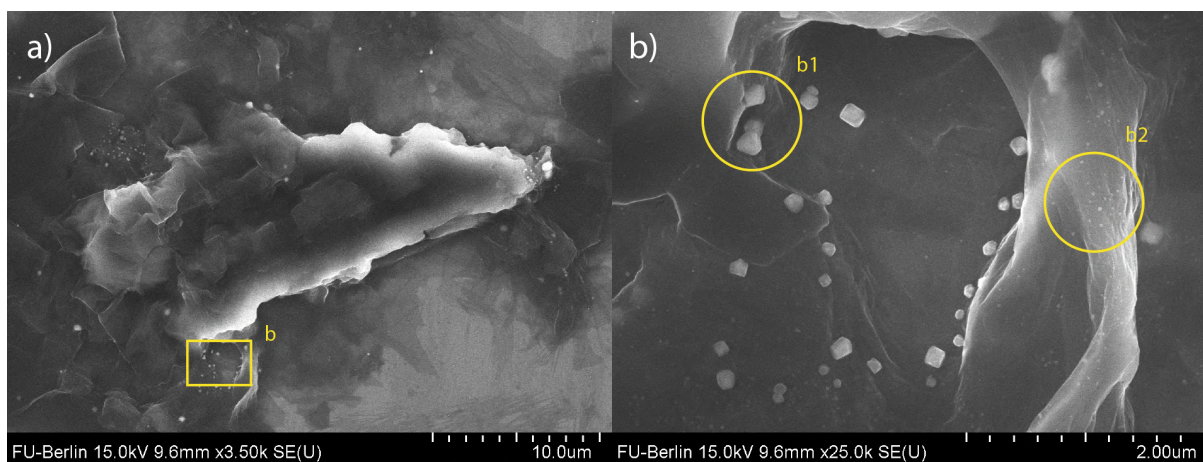
Figure 5.8: SEM images of T-SNPs/GO composite. a) Correspond to the *In-situ* irradiated with 3000 K white light. b) Close up view from the region indicated in a) the circle indicates nanoparticles with different sizes

observed AgNPs in some cases show to be anisotropic but in others the distinction is not clear. GO seem to have play a key role in the agglomeration of the AgNPs perhabs GO was not equally disperse between samples which led to the agglomeration of AgNPs. The agglomerates are observed in a less or higher degree among all samples and their formation can be more attributed to the GO presence than the light of irradiation.

Also, it is visible in the images that the edges of the GO flakes are brighter than any other part of the flake,
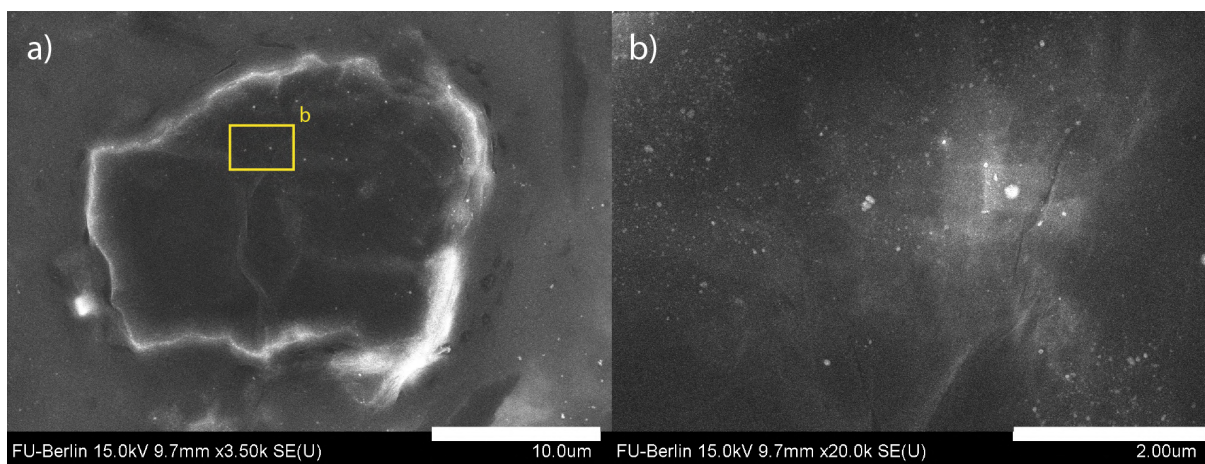
Figure 5.9: SEM images of T-SNPs/GO composite. a) Correspond to the *Ex-situ* irradiated with 3000 K white light. b) Close up view from the region indicated in a) the circle indicates nanoparticles with different size
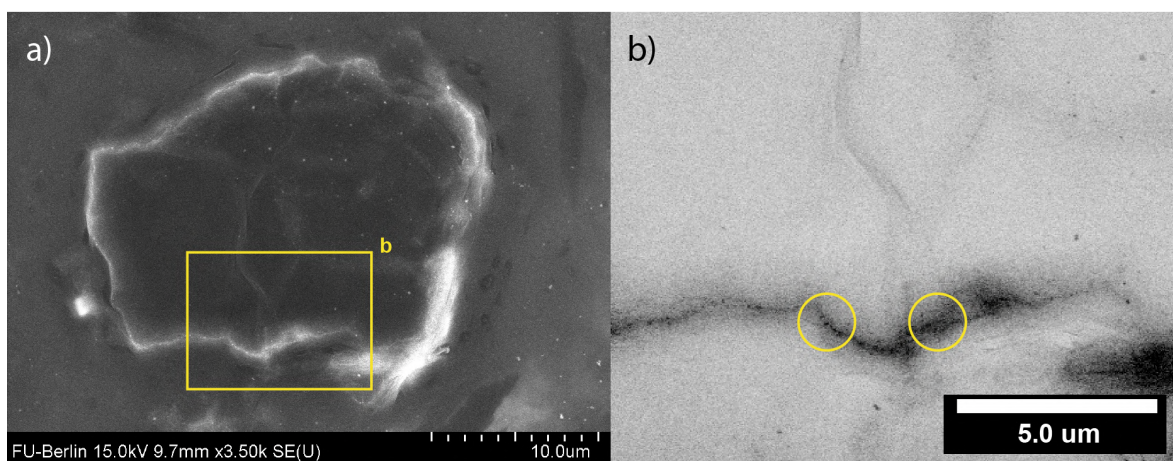
Figure 5.10: SEM images of T-SNPs/GO composite. a) Correspond to the *Ex-situ* irradiated with 3000 K white light. b) Close up view from the region indicated in a) the color of the image has been inverted to show more clearly the AgNPs at the edges of the GO flake.

bright regions appear due to two effects (i) accumulation of electrons (charge) due to the low conductivity of GO and the SiO_2 substrate that was used. (ii) High concentration of AgNPs or nanoplates suggesting a more aggressive deposition around edges (Figure 5.10 b). This explanation considers the fact that GO edges are more unstable and reactive, thus facilitating the reduction of remaining Ag^+ and some silver nanoparticles around those regions and increasing in this way the concentration of silver.

The avoidance of agglomeration of AgNPs is desired to enhance the surface area. Thus, improving catalytic and sensing properties of the nanocomposite. The SEM images are not conclusive to show the real dispersion of sizes and shapes of AgNPs or silver nanoplates, and how their size and shape distribution should be different for each sample due to the use of different wavelengths. More analysis is needed to confirm this hypothesis. Also, the wavelength of irradiation shows to act differently for both methods, but more analysis over the interaction between light, GO, and the AgNPs is needed to understand this process entirely. Regardless of the irradiation wavelength or synthesis method, samples show signs of agglomeration with large particles $\approx$ 500 nm.

5.2.2   Transmission Electron Microscopy (TEM)

TEM images show in more detail the dispersion and shape of silver nanoplates including T-SNPs that are deposited on GO flakes. Due to the previous analysis of SEM and the UV-vis spectra, only blue and green (*In-situ* and *Ex-situ*) samples are analyzed. The micrographs show overall the deposition of T-SNPs over the surface of GO flakes, although each sample shows different dispersion and concentration of the silver related nanostructures.

TEM images of the *Ex-situ* blue sample Figure 5.11 show only GO flakes. In Figure 5.11 a) a GO flake of around 20 μm is visible revealing several dark regions. This regions indicate the stacking of several flakes. In Figure 5.11 b) is more clear the stacking of the several layers. For this sample TEM show no adhesion of T-SNPs or AgNPs even though UV-spectra indicates the presence of these structures.
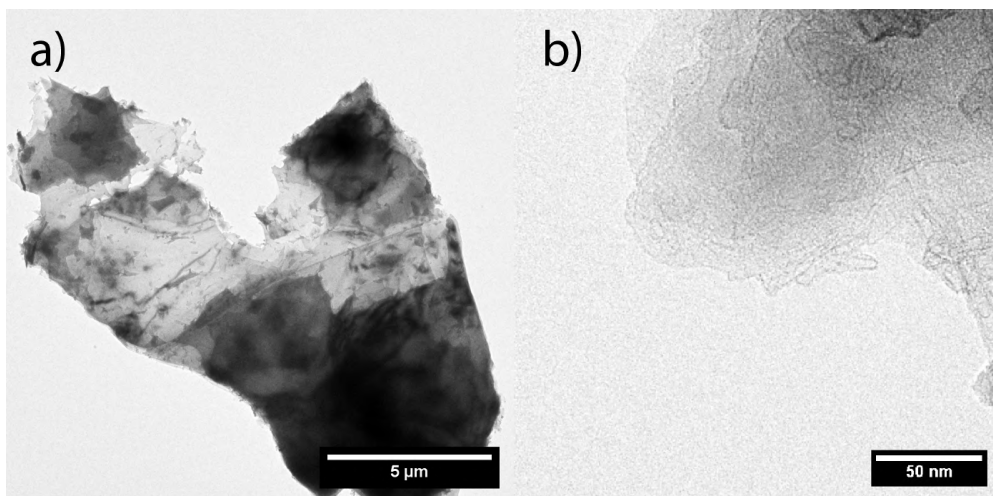
Figure 5.11: TEM images of *Ex-situ* blue sample. a) show an GO flake with different layers b) correspond to a close up view of the flake.

On the other hand, the *In-situ* blue sample shows the presence of the nanoparticles on GO with a size between 2-3 nm. Moreover, no T-SNPs were observed, it is important to note that even though the T-SNPs are not observed in these micrographs (*In-situ* and ex-sit blue), they could be present in some other parts of the sample due to the UV-vis spectrum obtained from the sample which corroborates the presences of silver nanoplates (Figure 5.3). Another indicator is the color of the solution. Typically AgNPs with sizes between 2-10 nm produce a yellowish solution, but the final color of this sample had a reddish color Figure 4.2, which is in agreement with what has been reported.[2,21] As mentioned before, optical properties are dependent on the size and shape of the silver nanostructures. Thus, a change in color is a qualitative indicator of a change in size and morphology.

Another TEM images of the *In-situ* blue sample (Figure 5.12) suggest the observation of silver nanoplates. The high atomic number of silver create dark spots when observed allowing an easy identification in this case since no other heavy elements are present. Knowing that the dark spots are silver nanoplates or nanoparticles, an assumption

Figure 5.12: TEM images of T-SNPs/GO composite from the *In-situ* blue. a) wide view of the GO flakes with the decoration of the silver nanoparticles b) and c) Silver nanoparticles on top GO surface d) Size distribution of the particles.

can be made considering that the thickness of the nanoparticles should also alter the visible darkness displayed by the nanoparticle in the TEM images. In Figure 5.13 several nanoparticles can be observed. However, some nanoparticles display grayer shades than others. Those which are darker could indicate a higher thickness. In this way, one can argue that darker spots represent spherical nanoparticles whereas grayer spots indicate a narrow thickness and therefore suggest a possible identification of nanoplates. Other factors like the presence of GO and other reagents and the possible stacking of several nanoparticles could also change the aspect of the observed spot. A side view or AFM image of the sample should be required to determine the thickness of the observed nanoparticles.

It is important to point out that both structures were found in the *In-situ* blue sample. Figure 5.12 b) and c)

showed spherical nanoparticles between 2 to 5 nm deposited on GO surface. Regarding these results, GO seem to have play both roles as substrate and promoter of the growth of AgNPs. Both roles occur simultaneity at different regions of the flakes causing a more heterogeneous dispersion of sizes. It is notice that flat regions on the GO flakes allowed the stabilization of the AgNPs Figure 5.12 b) and c), while region where flakes are wrinkled and folded tend to agglomerate the nanoparticles Figure 5.16. From Figure 5.12 a) the same tendency can be observed with Some clusters of nanoparticles in wrinkled regions. Nevertheless, the observed region shows a homogeneous dispersion of AgNPs in Figure 5.12. The presences of the AgNPs show that the photo-reduction process is not complete. Moreover, it suggests that GO has been acting as a substrate and stabilizer for the AgNPs blocking the photo-reduction and the conversion to T-SNPs.
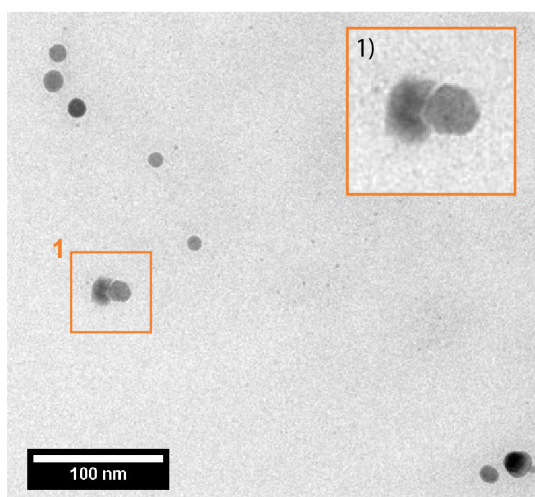
Figure 5.13: TEM images of *Ex-situ* blue sample showing silver nanoplates in solution.

The green *Ex-situ* sample shows more silver nanoplates than previous ones in which the sizes and shapes are heterogeneous (Figure 5.14 b and c). Structures with size 25 and 30 nm are abundant with a heterogenous distribution of sizes. T-SNPs with AgNPs are observed in this sample. Moreover, more agglomeration is visible at certain regions, and the concentration of T-SNPs and other nanostructures is higher than in previous results. Planar structure can be seen at the surface of GO showing the decoration of GO with silver and how GO can support metallic nanostructures. Next, the green *In-situ* sample shows again the presence of planar silver nanostructures larger than 20 nm and a clear distinction between shapes (Figure 5.15 b and c). Several morphologies can be seen deposited over a multilayer GO flake. The size distribution is between 10 ± 5 nm, and the dispersion is homogeneous. Figure 5.16 a) show that T-SNPs are located over GO, and also many are free showing low sign of agglomeration. In a small region of the two green samples, minor differences can be observed between the two methods where T-SNPs are present with other planar shapes (Figure 5.17). This can be explain by considering that those nanoplates possibly growth in the absence of GO since they are found in the solution. Less T-SNPs and other planar structures are found on GO than in solution. The TEM images suggest that multilayers of GO flakes with rugged sufaces promotes the agglomeration of
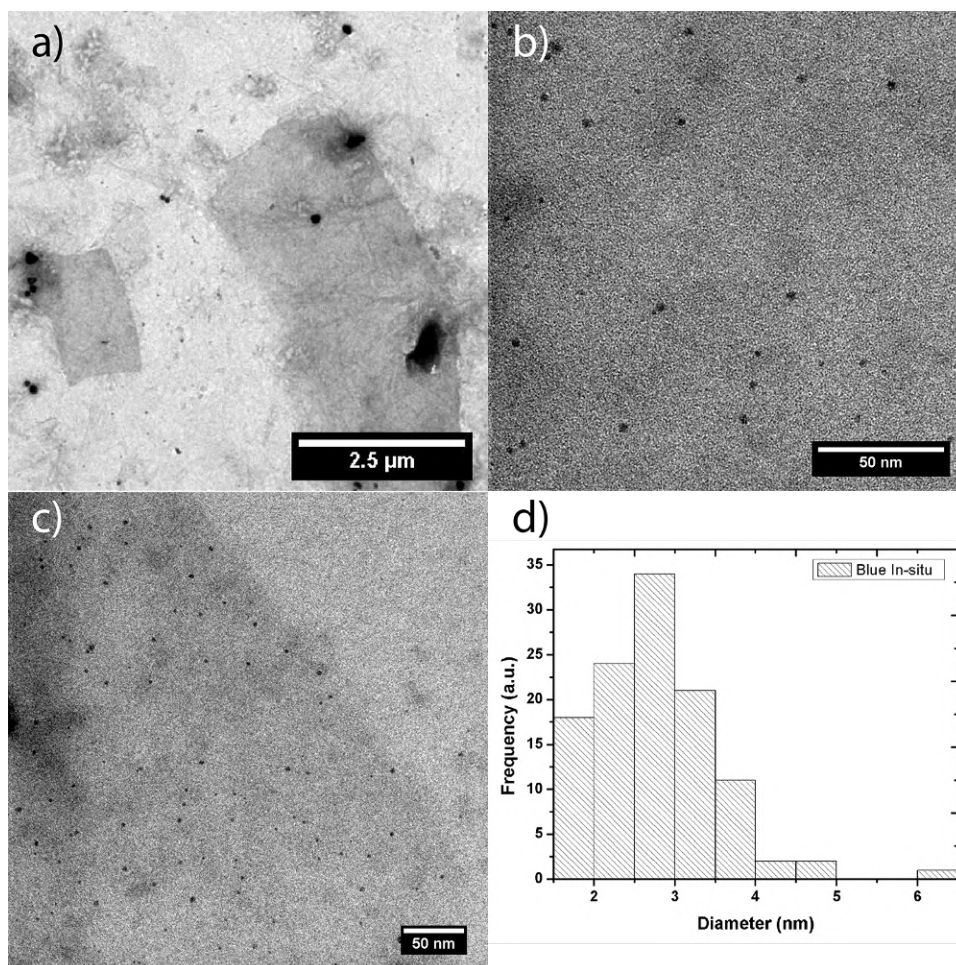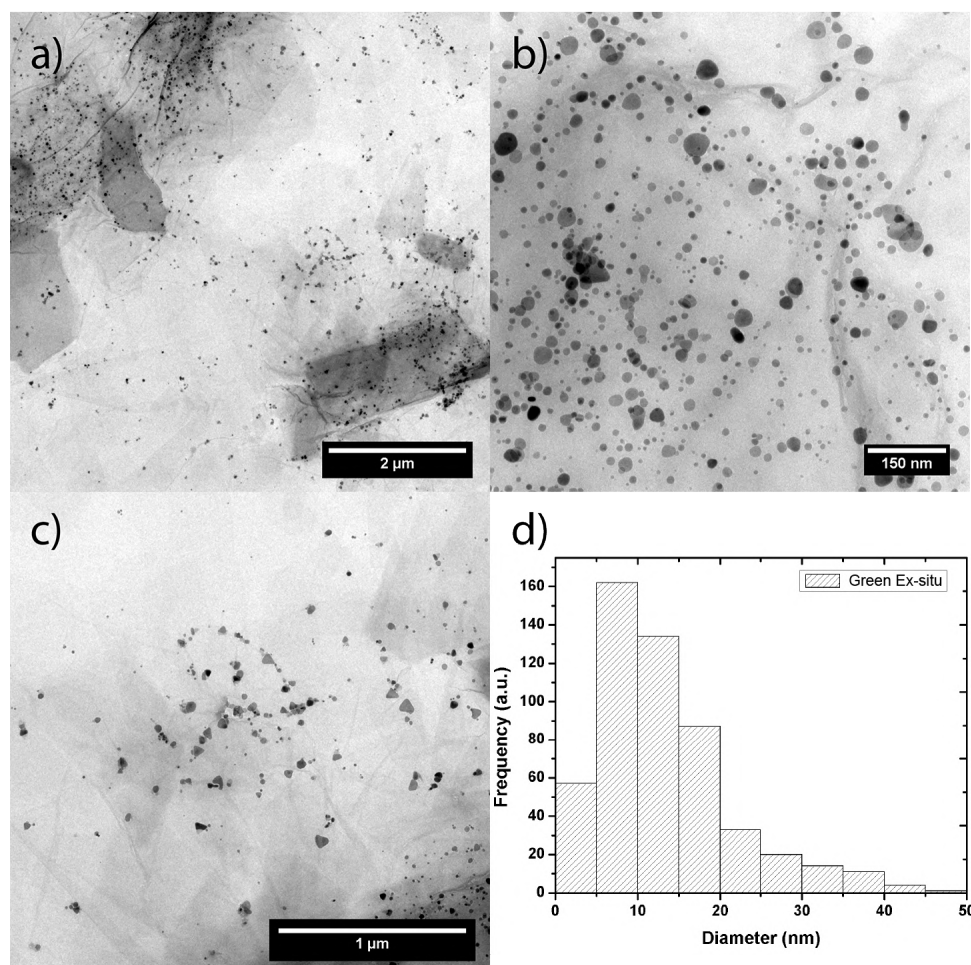
Figure 5.14: TEM images of T-SNPs/GO composite from the *Ex-situ* green. a) wide view of the GO flakes with the decoration of the T-SNPs b) and c) Silver nanoplates of different shapes including the triangular one d) Size distribution of the particles.

AgNPs and inhibit the formation of planar structures. T-SNPs and other nanoplates can be seem on the GO surfaces in areas where GO is smooth and single layer.

Several differences are found in both methods used so far, for instance, The *In-situ* process for green and blue samples shows to lead into a different dispersion of sizes and shapes than the *Ex-situ* method even though the color of the solution was almost the same. From all the data presented, the *In-situ* method promotes the growth of more T-SNPs, compared to the *Ex-situ* method, although many efforts need to be taking into account to improve the yield and stability of T-SNPs. UV-vis spectroscopy has shown that *In-situ* samples have a better yield due to the presence of a stronger signal, but these results cannot be confirmed by TEM microscopy. Here the observation suggests
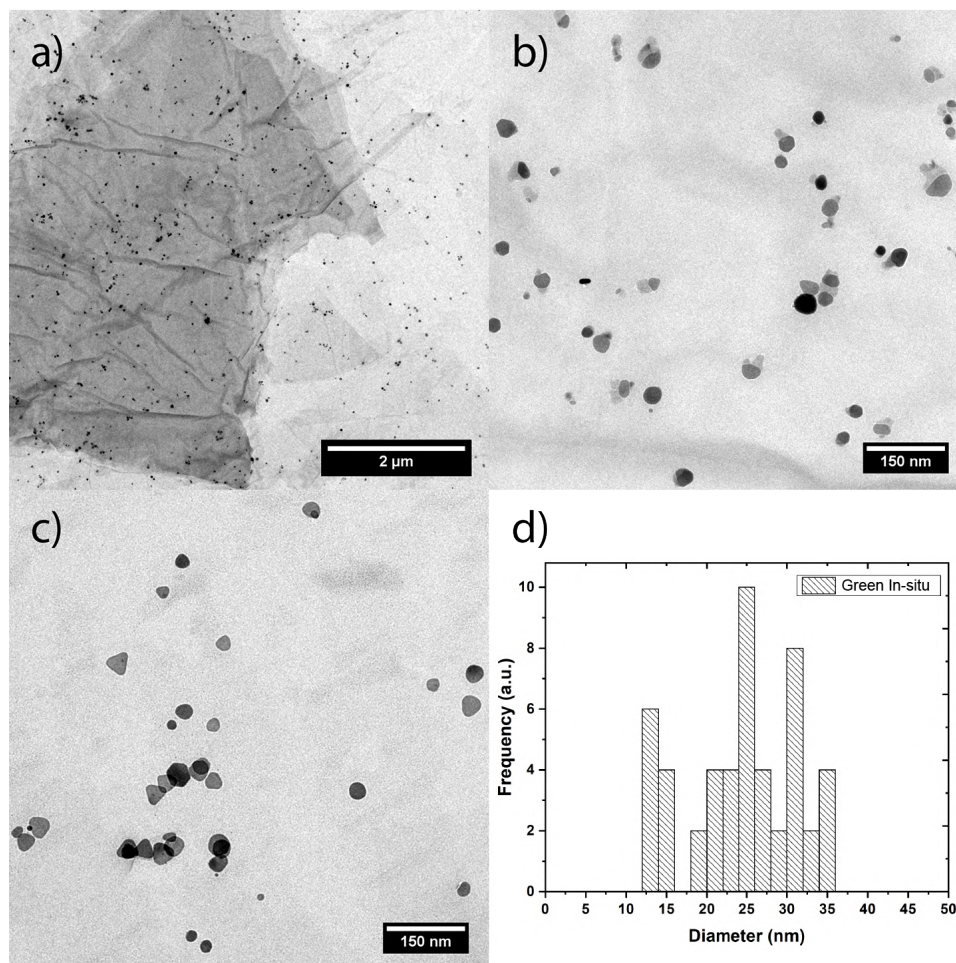
Figure 5.15: TEM images of T-SNPs/GO composite from the *In-situ* green. a) wide view of the GO flakes with the decoration of the T-SNPs b) and c) Silver nanoplates of different shapes including the triangular one d) Size distribution of the particles.

that GO is acting as a support matrix for AgNPs, then the nanoparticles start to grow due to the presence of Ag$^+$ ions that are still a presence in the solution. The deposited nanoparticles are fixed a have more controlled growth. However, as the size of the nanoparticles increases, the electrostatic interaction between GO and AgNPs cannot hold, and the nanoplates that grow will just separate from the GO matrix. Another possible explanation is that the low concentration of AgNPs limits the observation of these structures in all GO flakes, obtaining flakes were the presence of silver is very low. This behavior can be observed in the case of the green sample were UV-vis show more presence in the *In-situ* sample; however, in the TEM images, the opposite is observed. Further analysis needs to be done to find the effect caused by the addition of GO in the photochemical process.
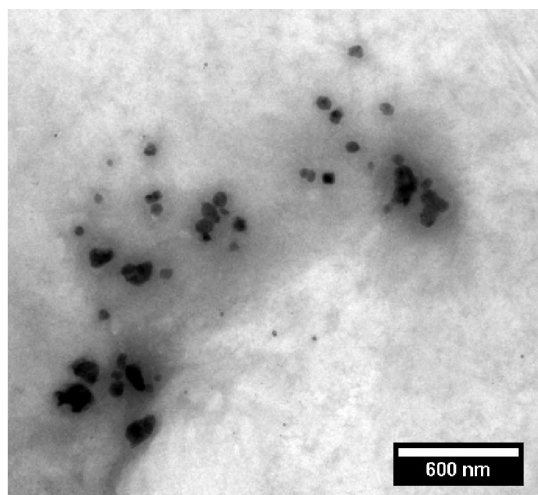
Figure 5.16: TEM images of *Ex-situ* blue sample showing agglomerates of silver nanoparticles on the GO surface.
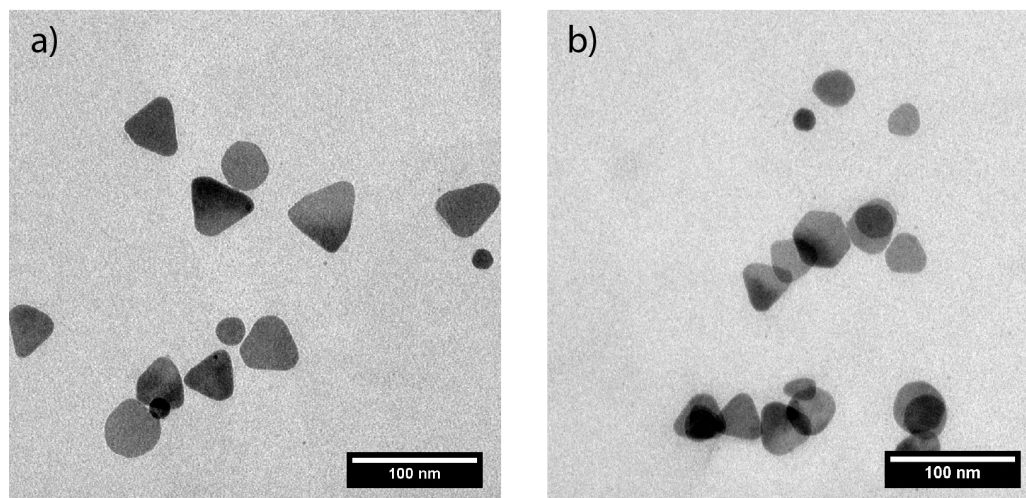
Figure 5.17: TEM images of T-SNPs/GO composite from the *In-situ* green sample.

5.3   Raman Spectroscopy

Raman Spectroscopy was employed to investigate the potential correlations between the absorption band and surface-enhanced Raman scattering (SERS) activity of T-SNPs on top of the GO surface. Also, understand the effect of the size and shape of the metallic structures and their influence in sensing for electrochemical sensors.

The Raman spectra of GO obtained was in agreement with the literature.[103] Normally GO shows two main peaks that correspond to the G and D bands. The G band peak is located at $\approx 1340 \ cm^{-1}$ and a D band located at ≈ 1600 cm^{-1}. The Raman intensities for D and G band of GO are greatly enhanced compared with that of pristine GO due to the electromagnetic enhancement of the decorated T-SNPs.[81] This happens regardless of the sample. However, size or shape effects are noticeable due to the different enhance factors that the samples show (Figure 5.18).
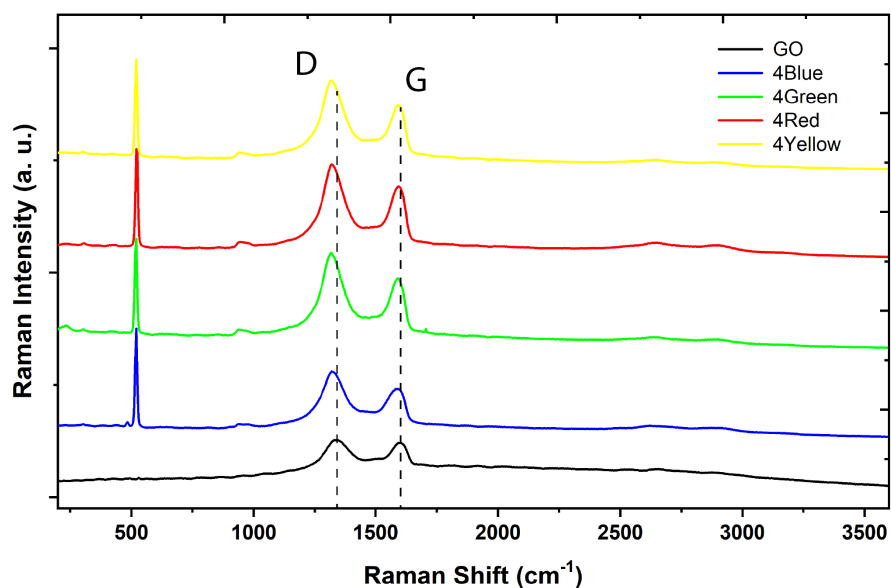
Figure 5.18: Raman Spectra of *In-situ* T-SNPs/GO and Pristine GO on top of a silicon wafer exited with a 637 nm laser.

When analyzing the D and G bands, the D peak shows a shift of about $\approx 20 \ cm^{-1}$, which indicates a partial reduction of the GO by the photochemical method. Also, the increase in intensity shows that there is a physical interaction between GO and the T-SNPs. The results obtained from Raman measurements imply that, on the one hand, AgNPs provides a strong electromagnetic enhancement to amplify Raman signal of GO.[104] while T-SNPs improve the signal even further. Figure 5.18 and 5.19 shows the Raman spectra of GO, *Ex-situ* and *In-situ* samples with the respectively D and G band. First, the sample irradiated with white light has almost the same intensity, followed by an increase by the red, blue, and finally the green samples. The Raman spectra of GO for the *Ex-situ* samples indicate to have distinct intensities of the D and G bands regarding each irradiation wavelength whereas the

behavior of *In-situ* samples show similar intensities despite the light source with the blue sample as an exception Figure. The intensity of D an G band is higher for the *In-situ* samples. Raman signal should be more intense in the presence of nanoparticles, nanodisk, or T-SNPs where its shape induces LSPR that are in resonance with the excitation light.
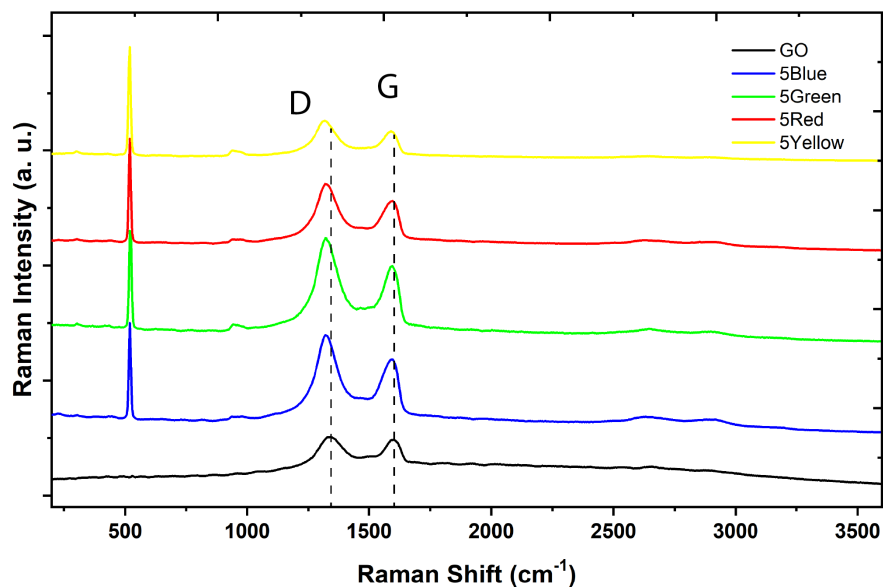
Figure 5.19: Raman Spectra of *Ex-situ* T-SNPs/GO and Pristine GO on top of a silicon wafer exited with a 637 nm laser.

	Intensity Ratio I_D/I_G	
GO Pristine	1.053	
(IR) Samples	*In-situ*	*Ex-situ*
440 nm (blue)	1.335	1.302
540 nm (green)	1.350	1.348
650 nm (red)	1.389	1.291
3000 K (white)	1.372	1.334

Table 5.2: Intensity Ratio I_D/I_G for all samples including GO pristine.

For example, T-SNPs that were prepared by green light should promote higher Raman intensities when the sample is measured with a green laser, that should be the case for red samples with red laser and the blue with a blue laser and so forth. However, this tendency is not observed; for instance, *Ex-situ* and *In-situ* samples indicate that the green light provides the highest enhancement in the Raman signal, and for the *In-situ* samples only, the Raman

signal from the red and white irradiated samples has the same intensity as the green one. TEM images show that green irradiated samples have more planar structures and bigger sizes, which agrees with the Raman results. Thus, indicating that more planar structures were deposited in the green samples. These results reveal that many T-SNPs were not deposited and that the enhancement of the signal comes from AgNPs and T-SNPs that were able to stay deposited on GO. Before, Uv-spectroscopy demonstrates that the silver seeds were photo-converted in relation to the wavelength employed. Additionally, the results show to agree with other works[2,3]. It is not clear how T-SNPs were deposited frequently in this case than other samples. However, results indicate that more T-SNPs were deposited by the *In-situ* method.
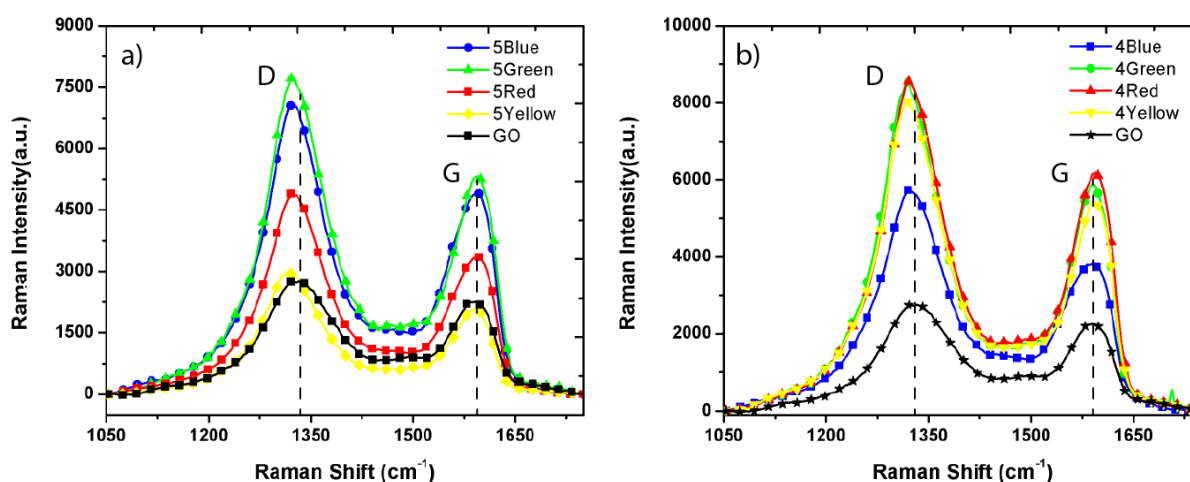
Figure 5.20: Normalized Raman Spectra of T-SNPs/GO and Pristine GO showing the D and G bands. a) *Ex-situ* samples, b) *In-situ* samples

The *In-situ* samples show to have further enhanced the signal that *Ex-situ* ones (Figure 5.20). The samples from the green, red, and white from the *In-situ* method display the maximum enhancement. UV-vis spectroscopy, SEM and TEM images have shown that planar silver structures and T-SNPs have been produced by both photochemical methods, but they were consistent to show that the *In-situ* method has produced more planar structures and, has also shown that the control in size and shape was more effective by the use of this methodology. Therefore, the Raman analysis is also in agreement with the hypothesis that GO works as a cite of nucleation, allowing the growth and stabilization of silver nanostructures. Several sites of the sample were analyzed to show that the enhancement of the Raman signal is not only produced by a higher concentration of the silver nanoplates at a specific region but to prove that with the same concentration an even further enhancement can be made by adjusting the size and shape of the silver nanoplates. The results show that the anisotropy of the silver nanoplate has a stronger enhancement factor for the Raman signal since three samples from the *In-situ* method obtain very similar Raman intensities. Uv-spectra of these samples show that the characteristic peak of each sample was located at a different position, indicating the difference in sizes obtained, it is important to notice that there exist some correlation of size between these three

samples; however, this is minimal in comparison with the rest of sizes that should be present in the GO surface also, if we compare with the *Ex-situ* samples we see that green and blue do not correlate well in the UV-vis spectra. However, the behavior in the Raman analysis is very similar.
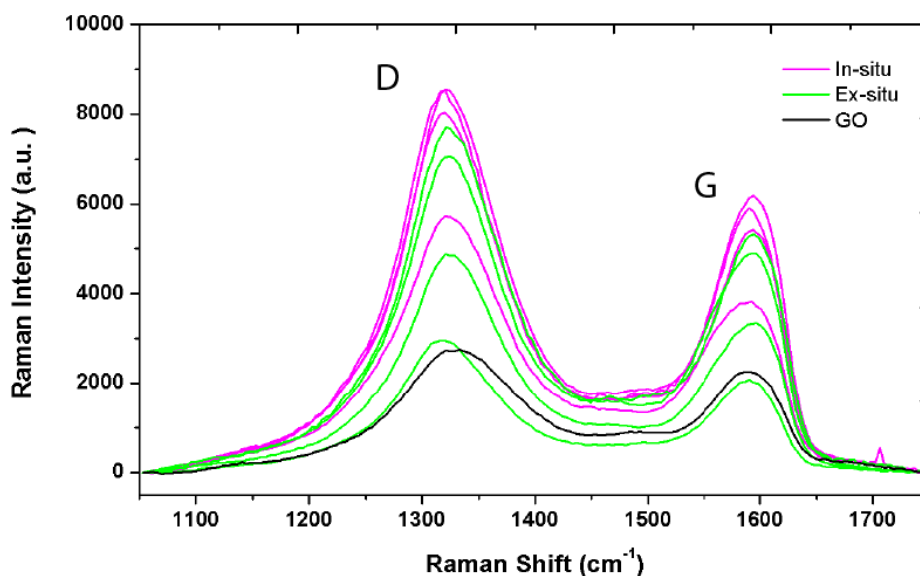
Figure 5.21: Raman Spectra of all T-SNPs/GO.

Figures 5.20 and 5.21 shows the Raman peaks that correspond to the D and G bands, respectively. The D band gives information about the disorder of the GO atomic structure. By comparing the ratio of the areas of the D and G peaks, it is possible to know if more defects have been introduced into the structure[105]. The intensity ratio I_D/I_G of the GO pristine is 1.05 showing the lowest ratio, then when the T-SNPs are present, the nanoparticles start to change the oxidation state of the GO thus introducing more defects to the structure causing the intensity ratio I_D/I_G to differ. Table 5.2 summaries the intensities ratio for all samples. By comparing all the intensity ratios, it is clear that the T-SNPs have introduced more defects in the GO structure. The intensity ratio between *Ex-situ* and *In-situ* samples that where exited with the same wavelength show similar values. *In-situ* samples show to have increased more the defects of the surface due to its higher intensity ratio I_D/I_G, which in part was expected, due early interaction of GO with silver ions and its presence in the photochemcial reduction process. These results seem to confirm the interaction between the T-SNPs and the GO surface at least regarding inelastic scaterring of light and the enhancement of the Raman signal. Also, the *In-situ* method has a more significant enhancement, which indicates that more interaction occurs in this case. This effect can be explained by considering that more particles are deposited in the GO surface, causing a greater signal, but also the same effect can be produced by the specific enhancement that is produced by a specific shape and size.

5.4   Cyclic Voltammetry

Cyclic voltammetry was employed to study the electrochemical properties of T-SNPs/GO nanocomposite. The measurements were performed as described above in the methodology. The results show that a potential range from -1.0 V to 0.0 V was not able to reduce GO since no reduction peak related with GO was observer in the measurments (Figure 5.22 a). On the other hand, reduction of silver was obtain, showing that for each cycle the reduction potential is decreasing suggesting an catalytic effect (Figure 5.22 b). Silver reduction suggest the indirect deposition of GO at the GRA surface. This was later confirmed by analyzing the GRA electrode using Raman spectroscopy (Figure 5.28). All the samples observed the reduction peak. Due to previous analysis, only the deposition of the green and blue samples is shown to compare both methods.
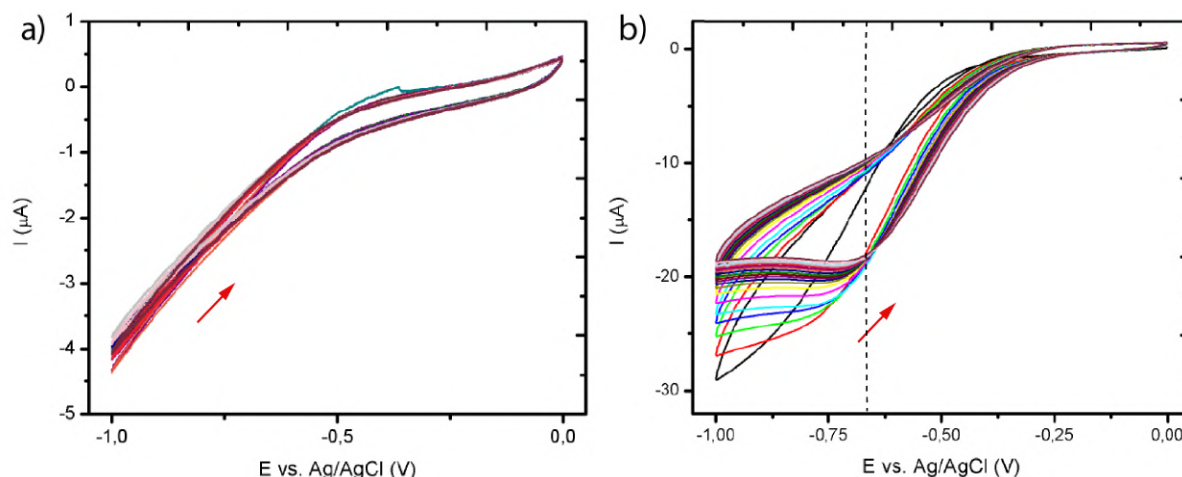
Figure 5.22: CVs curve between -1.0v to 0.0v a) CV of the GRA electrode in a GO solution. b) CV of the electrochemical deposition of T-SNPs/GO (blue-exsitu sample)

Figure 5.23 show that there is not a defined position of the cathodic peak. The potential at which the reduction happends is varied for each sample. The variations,however, are minimal and the potential is always colse to a -0.75 V pontential. Regarding the current, it is visible that in the CV curve of the blue *In-situ* sample the current is lower that the *Ex-situ*. However, the opposite effect is demostrated by the green sample. Another aspect to be noticiable is the faster decay of the reduction peak in the *Ex-situ* sample. Nonetheless, this behavior is visible for all the deposition curves. The explanation of this observation occurs due to stacking process of the nanocomposite that occurs at the graphite surface. When the first flake of the nanocomposite is deposited in the graphite surface it needs more energy to get reduced, then the next layer will find certain affinity to the preexisting layer thus reducing the energy neccesary to reduce that layer so the oxidation peak gets reduced by each cycle.

In the NaCl at 1% the oxidation of silver is confirm by the appearance of the oxidation peak (Figure 5.24). The lack of an reduction peak in this system indicates that the reaction is irreversible suggesting that after the oxidation the silver ions are forming sodium chloride (AgCl) with the Cl^- ions that dissolve in the solution. Figure 5.24 show
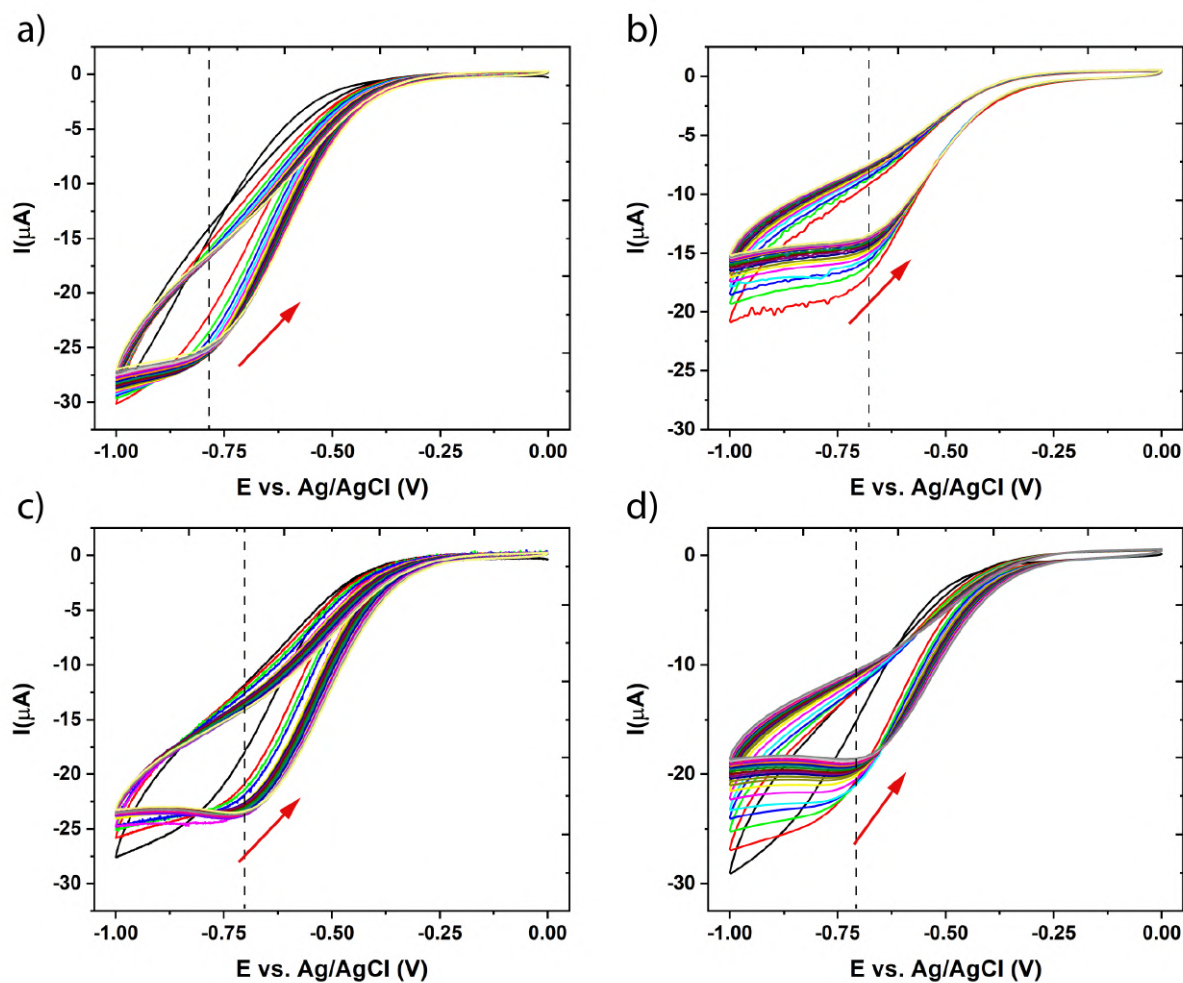
Figure 5.23: CVs curves of 25 cycles between -1.0v to 0.0v a) and c) CV curve of the electrochemical deposition of T-SNPs/GO (blue sample) a) *In-situ* c) *Ex-situ*. b) and d) CV of the electrochemical deposition of T-SNPs/GO (green) b) *In-situ* d) *Ex-situ*

the maximum current of the oxidation achieved at the first cycle. Between all the samples, the green *In-situ* shows the highest current but all the irradiated samples show an increase in the current intensity compared with silver seeds and pristine GO. The only case that reflect the opposite result is for the *In-situ* blue which has a lower current than the silver seeds Figure 5.24. It is important to notice that the oxidation peak has been shifted. The green *In-situ* samples have the lowest voltage in contrast with the blue *In-situ* which has the highest, both samples correlate the highest current with the lowest voltage and vice-versa. If the oxidation peak shifts to lower potential, it shows that the

reaction has been catalyzed. [12] showing some catalytic potential for the green *in-situ* sample. For the case of *Ex-situ* samples the relatio is not well stablish, however, the green sample is still the one with the highest current. Table 5.3 summaries the maximum current registrated for samples revealing that in general *In-situ* samples had higher current than *Ex-situ*. For the case of, Red and White *Ex-situ* samples no oxidation peak was observed.The absence of the peaks suggest that in the electrochemical deposition phase no silver was deposited on the graphite surface. Finally, Figures 5.25 and 5.26 show the evolution of the reduction peak of the green and blue samples revealing that every sample has a much higher current at the first cycle which drops drastically at the second. Then, the current start to decrease almost linearly until of the silver is oxidized for the electrode surface.

	Current (μA)		**Voltage (V)**	
Seed (AgNPs)	33.51		0.158	
(IR) Samples	In-situ	Ex-situ	In-situ	Ex-situ
440 nm (blue)	28.43	10.42	0.160	0.149
540 nm (green)	72.22	66.45	0.136	0.150
650 nm (red)	53.76	-	0.157	-
3000 K (white)	54.06	-	0.151	-

Table 5.3: Maximum current and voltage of the samples obtained at the first cycle in a 1 % NaCl solution.

We have seen silver oxidizing to lower potential. This effect is more dominant in the green *In-situ* sample, which as studied by TEM, SEM and UV-vis spectroscopy shows a higher amount of T-SNPs among other planar structures. On the other hand, we can see that the blue sample and silver seed show similar behavior. For instance, in this case, no improvement has been made by the adhesion of GO and the photo-conversion process. However, these results and the previous ones suggest that for this sample, T-SNPs have been produced, however, the deposition to GO is shallow, with only a few nanoparticles deposited and no sign of T-SNPs or other related planar structures is found at the GO flakes. Then, if we study the behavior of the oxidation peak, we can notice that the first cycle that has higher current does not behave the same as the other peaks. The potential at which this peak is located is a bit higher than the other, in which the other show to increase their potential and reduce its intensity by each cycle. In the case of the green *In-situ* sample, the oxidation peak shows overall lower potential than the *Ex-situ* green sample, and higher current, especially at the first cycle (Figure 5.23). Next, the blue sample shows no difference in the position of the oxidation peak between the two methods, but a higher current was obtained by the *In-situ* method in the first cycle.

Figure 5.24: CVs of GR/T-SNPs/GO electrode in 1% NaCl as the analysis medium. a) CVs of GR/T-SNPs/GO from the *In-situ* method. c) CVs of GR/T-SNPs/GOs from the *Ex-situ* method. b) and d) are close up views of a) and b) respectively at the oxidation peak.

Figure 5.25: CVs of GR/T-SNPs/GO electrode in 1% NaCl as the analysis medium. a) CVs of GR/T-SNPs/GO from the *In-situ* method green sample. b) CVs of GR/T-SNPs/GO from the *In-situ* method green sample. c) and d) are close up views of a) and b) respectively in the oxidation peak. e) and f) current vs cycles from the *In-situ* and *In-situ* green sample.
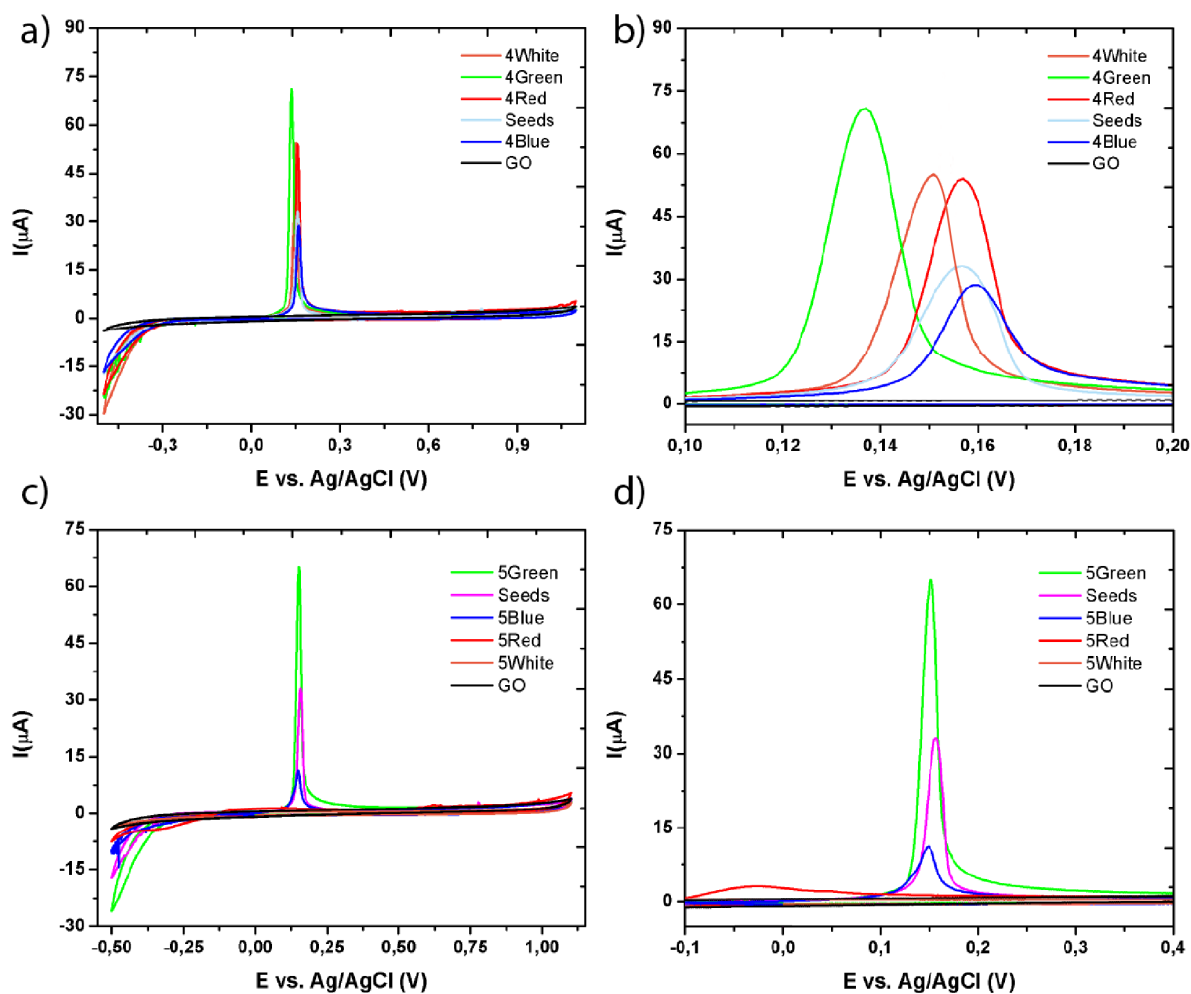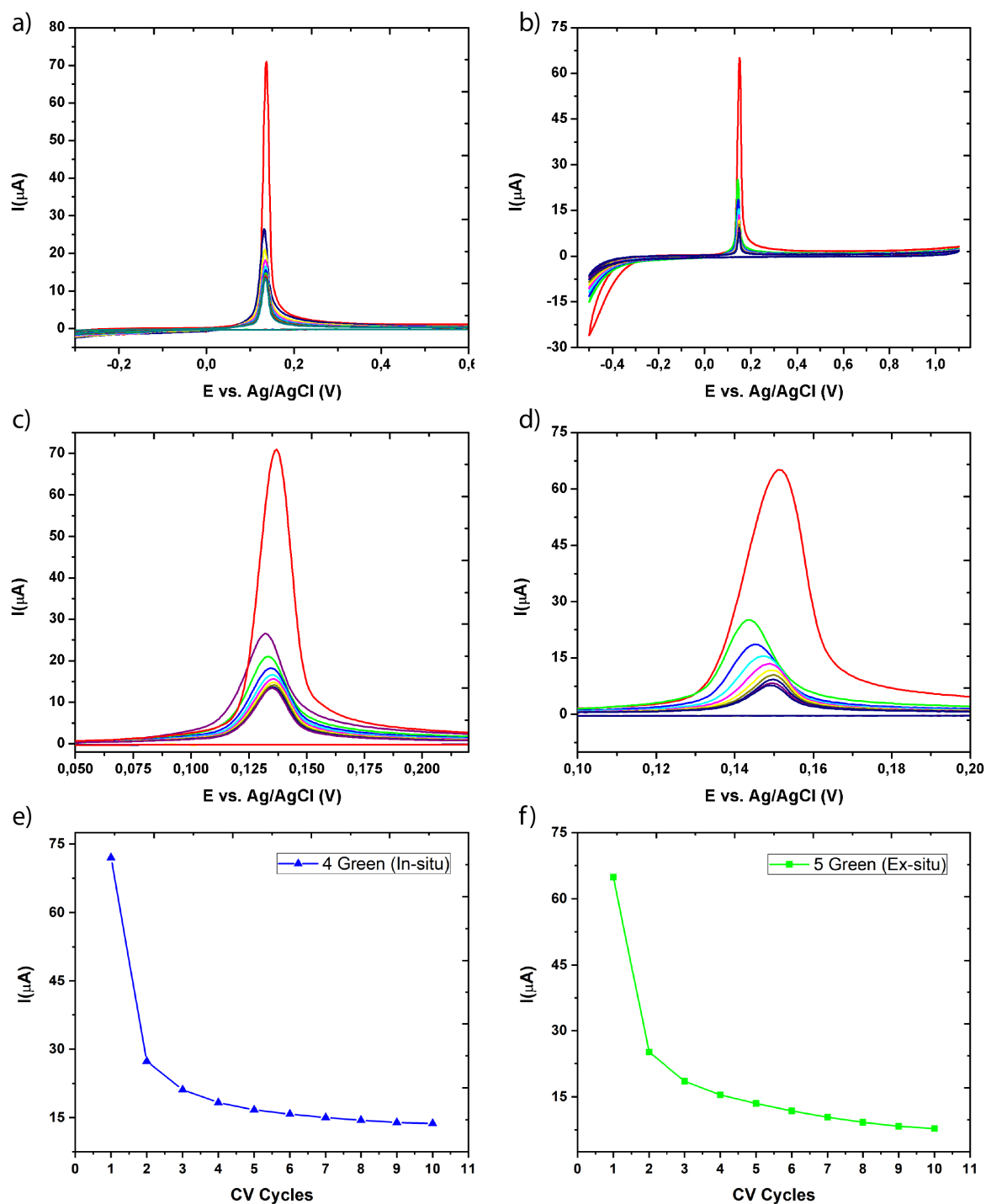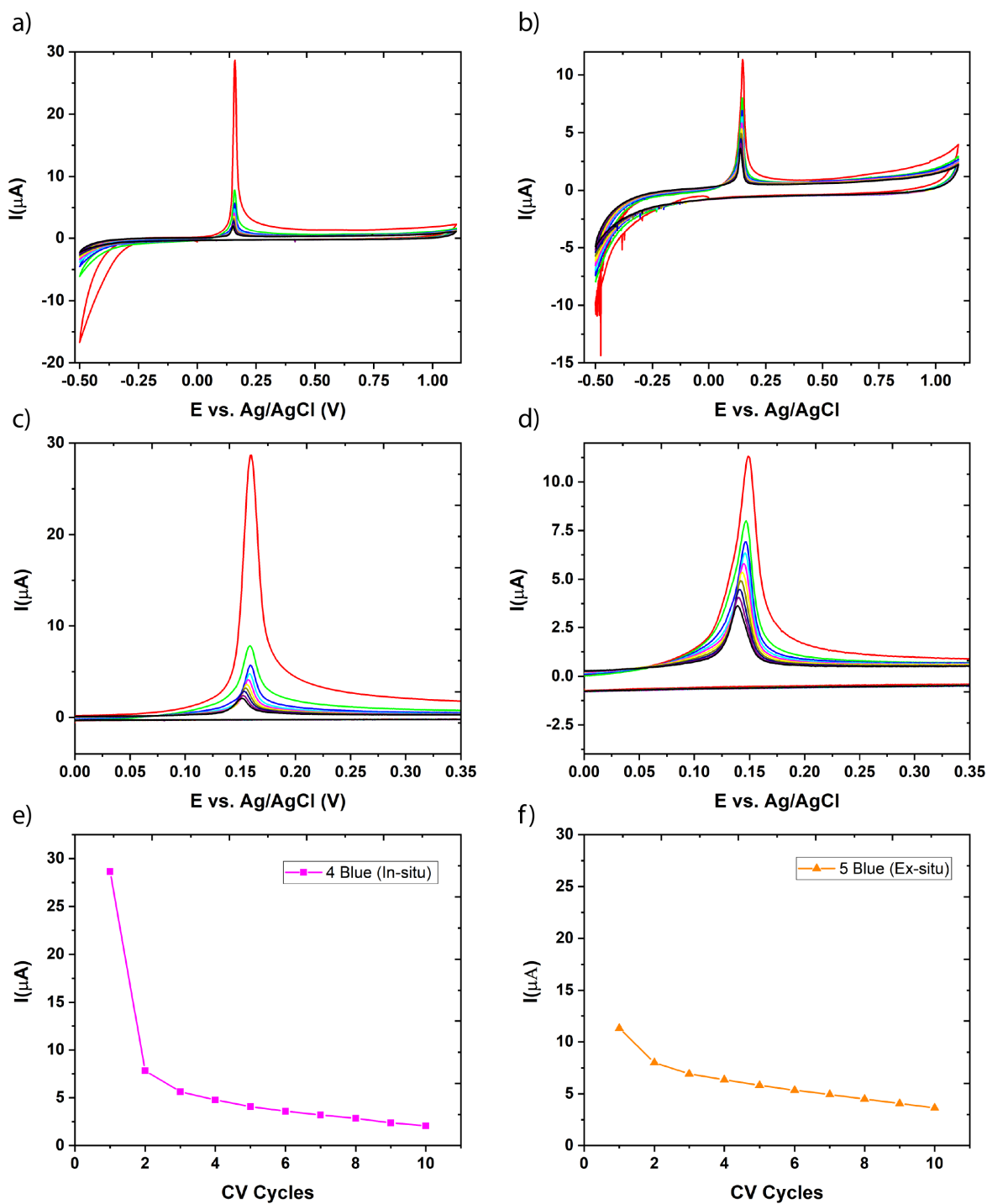
Figure 5.26: CVs of GR/T-SNPs/GO electrode in 1% NaCl as the analysis medium. a) CVs of GR/T-SNPs/GO from the *In-situ* method blue sample. b) CVs of GR/T-SNPs/GO from the *In-situ* method blue sample. c) and d) are close up views of a) and b) respectively in the oxidation peak. e) and f) current vs cycles from the *In-situ* and *In-situ* green sample.

5.5 Further Analysis

UV-vis spectra of the samples after the electrochemical deposition show that the morphology of the samples has changed. If we compare the spectra before and after, we can see that, first, the intensity of the 330 nm peak and the characteristic peak was decreased, and second, the characteristic peaks have been red-shifted (Figure 5.27 a). This result indicates a change in morphology. The decrease of intensity of the 330 nm shows that less anisotropic (or planar) structures are present in the solution. Moreover, the decrease of dipolar plasmon peak shows that less silver has the proper size and shape to interact with light and have the characteristic LSPR behavior. Thus, indicating that AgNPs, T-SNPs, and other related structures have been oxidized, and the concentration of those structures has decreased. For instance, in the case of the red sample synthesized by the *Ex-situ* method, an almost complete flattening of both absorption peaks is observed indicating the destruction of the T-SNPs and AgNPs.
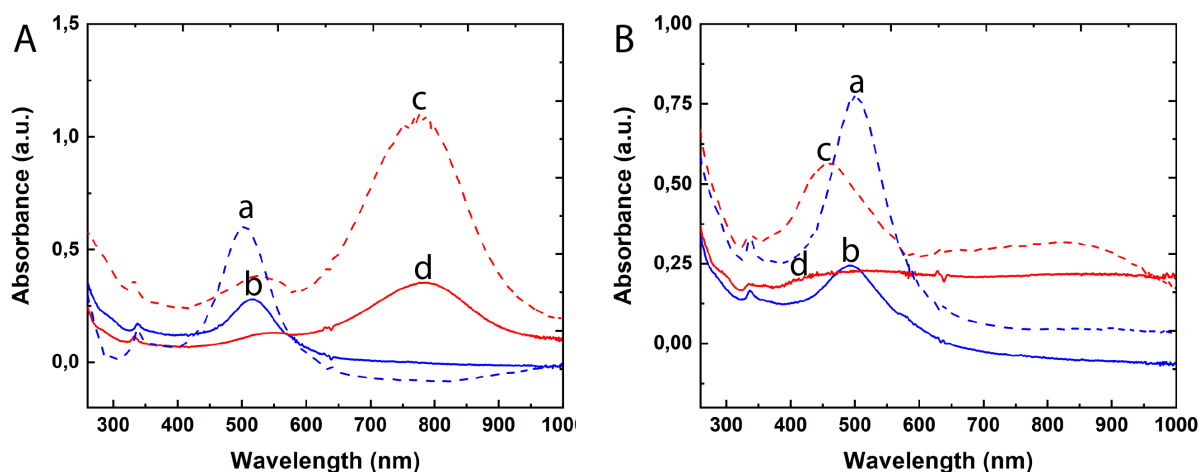
Figure 5.27: (A) UV-vis spectrum of *In-situ* blue and red samples before and After CV. Before CV (dashed line), After CV (solid line). a) and b) blue sample. c) and d) red sample. (B) UV-vis spectrum of *Ex-situ* blue and red samples before and After CV. Before CV (dashed line), After CV (solid line). a) and b) blue sample. c) and d) red sample.

Raman Spectra of the samples was performed before and after the electrochemical deposition of T-SNPs/GO nanocomposite. We can see that after the deposition and oxidation of T-SNPs the Raman spectrum shows that the original sample is just graphite, contrary to what we can see in the spectrum before the deposition and oxidation. This indicates the deposition of the nanocomposite at the surface of the electrode. It is important to point out that these measurements were carried after the electrochemical analysis, so the concentration of the nanocomposite should be much higher just after the electrochemical deposition. Further studies are required to compare both Raman spectra. In figure 5.28 b) the combined signal of GO and GRA can be seen. We can see how the G band gets enhanced due to the present of GO and Graphite, this is also true for the 2D band in which GO shows a narrow peak, but with the

addition of Graphite, the peak at 2720 cm^-1 gets enhance due to the sum of both signals. It is important to notice, that the signal of Graphite has a background, this due to a high fluorescence response of the graphite source since the graphite use was not pure but instead, it was a pencil lead that contains clay and some other polymer to give a more flexible structure. The fluorescence signal should be coming from those other compounds since graphite typically doesn't show this type of signal.
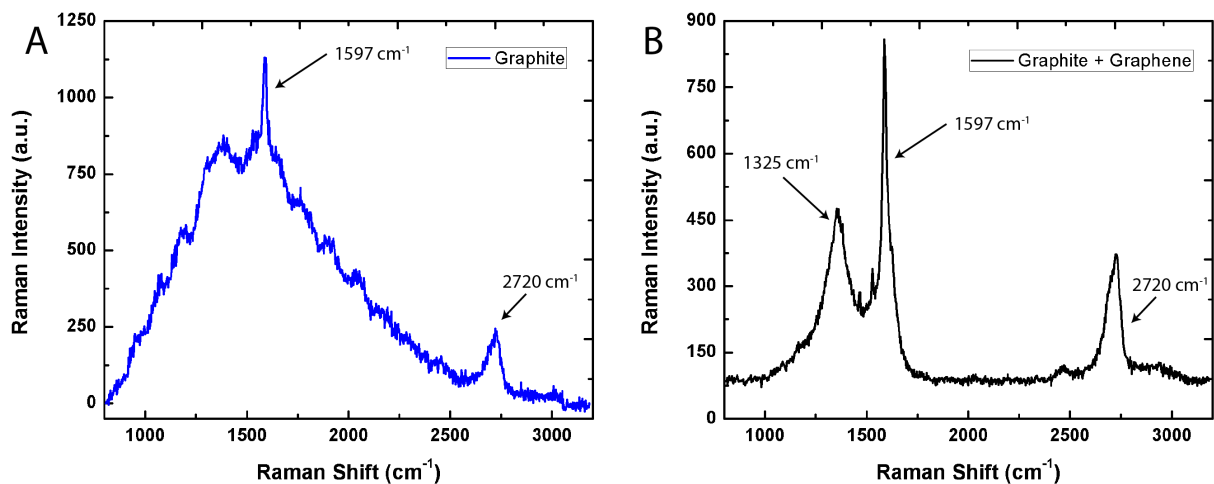
Figure 5.28: (A) Raman spectrum of the GRA electrode (B) Raman spectrum of GO + GRA electrode

Chapter 6

Conclusions & Outlook

T-SNPs/GO nanocomposite has been successfully synthesized by the photochemical conversion method. The characterization of the nanocomposite has shown that the In-situ method promotes the growth of more T-SNPs, with less size dispersion compare to the Ex-situ method. Also, the use of different wavelengths of irradiation has proved that have an effect on the control of size and shape of the T-SNPs on GO. UV-vis spectra have revealed the reduction of the 400 nm band and the appearance of the 330 nm characteristic peaks indicators of the photoconversion of AgNPs into T-SNPs. Both approaches demonstrate to have successfully converted from the spherical seeds (AgNPs) to T-SNPs. The higher intensity of the characteristic peaks observed using the *In-situ* method indicates a qualitative higher yield of the T-SNPs. SEM and TEM micrographs reveal the presence of T-SNPs on the GO surface. The results indicate more deposition of silver nanoplates in the case of the *In-situ* samples where AgNPs were converted using the green light at 540 nm. Nevertheless, further studies are needed to understand the effect of GO in the growing process and to determine the relationship between GO and the wavelength employed for the photochemical reduction.

Raman Spectra of the T-SNPs has shown an enhancement of the GO Raman signal demonstrating that T-SNPs are deposited on the GO surface. D and G bands of GO are considerably enhanced due to the SPR and LSPR effect produce by T-SNPs and other structures. It is important to point out that further enhancement is obtained in general by the *In-situ* method. Thus, indicating more deposition of T-SNP. AgNPs that were converted with the size and shape sufficient to have the SPR in resonance with the wavelength of the laser of excitation prove to have an even further improvement of the Raman signal. This result implies that the *In-situ* sample irradiated with the green light have deposited more silver nanoplates than the other lights used in this work. The analysis using Cyclic Voltammetry indicates that T-SNPs on GO improve the electrochemical properties. The large surface area compared with AgNPS due to the high anisotropy of T-SNPs where the width is dominant in contrast to the height allows the diffusion of the electrons. However, much work still needs to be done to improve the yield of T-SNPs on GO by the photochemical method to use as a potential sensor and understand how the wavelength affects the growth of the T-SNPs. The *In-situ* method show to provide a better yield of T-SNPs on GO as well to less size dispersion, improving the electrochemical properties and offering a low cost and efficient method to synthesized this type of nanocomposites.

Bibliography

[1] Rashid, M. H.; Mandal, T. K. Synthesis and Catalytic Application of Nanostructured Silver Dendrites. *The Journal of Physical Chemistry C* **2007**, *111*, 16750–16760.

[2] Saade, J.; de Araújo, C. B. Synthesis of silver nanoprisms: a photochemical approach using light emission diodes. *Materials Chemistry and Physics* **2014**, *148*, 1184–1193.

[3] Zhang, Q.; Li, N.; Goebl, J.; Lu, Z.; Yin, Y. A systematic study of the synthesis of silver nanoplates: is citrate a "magic" reagent? *Journal of the American Chemical Society* **2011**, *133*, 18931–18939.

[4] Zhang, J.; Langille, M. R.; Mirkin, C. A. Photomediated synthesis of silver triangular bipyramids and prisms: the effect of pH and BSPP. *Journal of the American Chemical Society* **2010**, *132*, 12502–12510.

[5] Zhong, L.; Gan, S.; Fu, X.; Li, F.; Han, D.; Guo, L.; Niu, L. Electrochemically controlled growth of silver nanocrystals on graphene thin film and applications for efficient nonenzymatic H_2O_2 biosensor. *Electrochimica Acta* **2013**, *89*, 222–228.

[6] Alexis Loiseau, G. B.-A. M. L. M. S., Victoire Asila; Boujday, S. Silver-Based Plasmonic Nanoparticles for and Their Use in Biosensing. *Biosensors* **2019**, *9*, 78.

[7] Mayer, K. M.; Hafner, J. H. Localized Surface Plasmon Resonance Sensors. *Chemical Reviews* **2011**, *111*, 3828–3857.

[8] Shen, H. Plasmonic nanoparticles: Towards the fabrication of biosensors. *IOP Conf. Series: Materials Science and Engineering* **2015**, *87*.

[9] Sarah Unser, J. H., Ian Bruzas; Sagle, L. Localized Surface Plasmon Resonance Biosensing: Current Challenges and Approaches. *Sensors* **2015**, *15*, 15684–15716.

[10] Kelly, K. L.; Coronado, E.; Zhao, L. L.; Schatz, G. C. The Optical Properties of Metal Nanoparticles: The Influence of Size, Shape, and Dielectric Environment. *J. Phys. Chem.* **2003**, *107*, 668–677.

[11] Pastoriza-Santos, I.; Liz-Marzán, L. M. Colloidal silver nanoplates. State of the art and future challenges. *Journal of Materials Chemistry* **2008**, *18*, 1724–1737.

[12] Bansal, V.; Li, V.; O'Mullane, A. P.; Bhargava, S. K. Shape dependent electrocatalytic behaviour of silver nanoparticles. *CrystEngComm* **2010**, *12*, 4280–4286.

[13] Lu, W.; Luo, Y.; Chang, G.; Sun, X. Synthesis of functional SiO_2-coated graphene oxide nanosheets decorated with Ag nanoparticles for H_2O_2 and glucose detection. *Adv. Mater.* **2006**, *18*, 2807.

[14] Bansal, V.; Li, V.; O'Mullane, A. P.; Bhargava, S. K. Shape dependent electrocatalytic behaviour of silver nanoparticles. *CrystEngComm* **2010**, *12*, 4280–4286.

[15] Huang, Z.; Jiang, X.; Guo, D.; Gu, N. Controllable synthesis and biomedical applications of silver nanomaterials. *Journal of nanoscience and nanotechnology* **2011**, *11*, 9395–9408.

[16] Zhang, Y.; Yuan, X.; Wang, Y.; Chen, Y. One-pot photochemical synthesis of graphene composites uniformly deposited with silver nanoparticles and their high catalytic activity towards the reduction of 2-nitroaniline. *J. Mater. Chem.* **2012**, *22*, 7245.

[17] Allen, M. J.; Tung, V. C.; Kaner, R. B. Honeycomb Carbon: A Review of Graphene. *Chem. Rev.* **2010**, *110*, 132–145.

[18] Bai, J.; Zhong, X.; Jiang, S.; Huang, Y.; Duan, X. Graphene nanomesh. *Nature Nanotechnology* **2010**, *5*, 190–194.

[19] Rongchao Jin, E. H. G. S. M. t. G. C. S. . C. A. M., Y. Charles Cao Controlling anisotropic nanoparticle growth through plasmon excitation. *Nature* **2003**, *425*, 487–490.

[20] Mathieu Maillard, P. H.; Brus, L. *Nano Lett.* **2003**, *3*, 1611–1615.

[21] Can Xue, J. E. M., Gabriella S. Mé traux; Mirkin, C. A. Mechanistic Study of Photomediated Triangular Silver Nanoprism Growth. *J. AM. CHEM. SOC.* **2008**, *130*, 8337–8344.

[22] Sun, Y.; Xia, Y. Triangular Nanoplates of Silver: Synthesis, Characterization, and Use as Sacrificial Templates for Generating Triangular Nanorings of Gold. 2003, *15*, 694–699.

[23] Jia Li, D. Z. D. Y. J. G. J. W., Lanlan Liu Fabrication of polyaniline/silver nanoparticles/multi-walled carbonnanotubes composites for flexible microelectronic circuits. *Synthetic Metals* **2014**, *192*, 15–22.

[24] Saptarshi Dhibar, C. K. D. Electrochemical performances of silver nanoparticles decorated polyaniline/graphene nanocomposite in different electrolytes. *Journal of Alloys and Compounds* **2015**,

[25] F. Ahour, M. A. An electrochemical label-free and sensitive thrombin aptasensor based on graphene oxide modified pencil graphite electrode. *Biosensors and Bioelectronic* **2016**,

[26] Fang, Y.; Guo, S.; Zhu, C.; Zhai, Y.; Wang, E. Self-assembly of cationic polyelectrolyte-functionalized graphene nanosheets and gold nanoparticles: a two-dimensional heterostructure for hydrogen peroxide sensing. *Langmuir* **2010**, *26*, 11277–11282.

[27] Scheuermann, G. M.; Rumi, L.; Steurer, P.; Bannwarth, W.; MuÌĹlhaupt, R. Palladium nanoparticles on graphite oxide and its functionalized graphene derivatives as highly active catalysts for the Suzuki- Miyaura coupling reaction. *Journal of the American Chemical Society* **2009**, *131*, 8262–8270.

[28] Putta, C.; Sharavath, V.; Sarkar, S.; Ghosh, S. Palladium nanoparticles on β-cyclodextrin functionalised graphene nanosheets: a supramolecular based heterogeneous catalyst for C–C coupling reactions under green reaction conditions. *RSC Advances* **2015**, *5*, 6652–6660.

[29] Muszynski, R.; Seger, B.; Kamat, P. V. Decorating graphene sheets with gold nanoparticles. *The Journal of Physical Chemistry C* **2008**, *112*, 5263–5266.

[30] Pasricha, R.; Gupta, S.; Srivastava, A. K. A facile and novel synthesis of Ag–graphene-based nanocomposites. *Small* **2009**, *5*, 2253–2259.

[31] Xu, W.-P.; Zhang, L.-C.; Li, J.-P.; Lu, Y.; Li, H.-H.; Ma, Y.-N.; Wang, W.-D.; Yu, S.-H. Facile synthesis of silver graphene oxide nanocomposites and their enhanced antibacterial properties. *Journal of Materials Chemistry* **2011**, *21*, 4593–4597.

[32] Zhang, Z.; Xu, F.; Yang, W.; Guo, M.; Wang, X.; Zhang, B.; Tang, J. A facile one-pot method to high-quality Ag-graphene composite nanosheets for efficient surface-enhanced Raman scattering. *Chemical Communications* **2011**, *47*, 6440–6442.

[33] Tang, X.-Z.; Cao, Z.; Zhang, H.-B.; Liu, J.; Yu, Z.-Z. Growth of silver nanocrystals on graphene by simultaneous reduction of graphene oxide and silver ions with a rapid and efficient one-step approach. *Chemical communications* **2011**, *47*, 3084–3086.

[34] Shen, J.; Shi, M.; Yan, B.; Ma, H.; Li, N.; Ye, M. One-pot hydrothermal synthesis of Ag-reduced graphene oxide composite with ionic liquid. *Journal of Materials Chemistry* **2011**, *21*, 7795–7801.

[35] Thomas, S.; Rafiei, S.; Maghsoodlou, S.; Afzali, A. *Foundations of Nanotechnology, Volume Two: Nanoelements Formation and Interaction*; AAP Research Notes on Nanoscience and Nanotechnology; Apple Academic Press, 2014.

[36] Kuno,; Kenneth, M. Introduction to nanoscience and nanotechnology: a workbook. 2005.

[37] Buzea, C.; Pacheco, I. I.; Robbie, K. Nanomaterials and nanoparticles: sources and toxicity. *Biointerphases* **2007**, *2*, MR17–MR71.

[38] Kent, J. A. *Handbook of Industrial Chemistry and Biotechnology*; Springer, 2012.

[39] Commission, E. *Nanosciences and Nanotechnologies: An action plan for Europe 2005-2009*; European Communities, 2005.

[40] McMullan, D. Scanning electron microscopy 1928-1965. *Scanning* **1995**, *17*, 175–185.

[41] Kroto, H. W.; Heath, J. R.; O'Brien, S. C.; Curl, R. F.; Smalley, R. E. C_{60}: Buckminsterfullerene. *nature* **1985**, *318*, 162–163.

[42] Geim, A. K.; Novoselov, K. S. *Nanoscience and technology: a collection of reviews from nature journals*; World Scientific, 2010; pp 11–19.

[43] Gong, J. R. *Graphene âĂŞ Synthesis, Characterization, Properties and Applications*; InTech, 2011.

[44] Wong, H.-S. P.; Akinwande, D. *Carbon nanotube and graphene device physics*; Cambridge University Press, 2011.

[45] Novoselov, F. V. I. C. L. G. P. R. S. M. G. . K. K., K. S. A roadmap for graphene. *Nature* **2012**, *490*, 192–200.

[46] Dirac cones in graphene. `https://ocw.tudelft.nl/course-readings/dirac-cones-graphene/`.

[47] Partoens, B.; Peeters, F. From graphene to graphite: Electronic structure around the K point. *Physical Review B* **2006**, *74*, 075404.

[48] Jing-Han, Y.; Wei-Wei, J.; Er-Qiang, L.; Tian-Song, P.; Yuan-Yuan, Z.; Hui, W. Fifth-nearest-neighbor tight-binding description of electronic structure of graphene. *Communications in Theoretical Physics* **2010**, *53*, 1172.

[49] Ray, S. C. In *Applications of Graphene and Graphene-Oxide Based Nanomaterials*; Ray, S. C., Ed.; Micro and Nano Technologies; William Andrew Publishing: Oxford, 2015; pp 39 – 55.

[50] Ray, S. *Applications of graphene and graphene-oxide based nanomaterials*; William Andrew, 2015.

[51] Eftekhari, A.; Shulga, Y. M.; Baskakov, S. A.; Gutsev, G. L. Graphene oxide membranes for electrochemical energy storage and conversion. *International Journal of Hydrogen Energy* **2018**, *43*, 2307 – 2326.

[52] Singh, D. P.; Herrera, C. E.; Singh, B.; Singh, S.; Singh, R. K.; Kumar, R. Graphene oxide: An efficient material and recent approach for biotechnological and biomedical applications. *Materials Science and Engineering: C* **2018**, *86*, 173 – 197.

[53] yan Chen, C.; ya Guo, X.; qiang Lu, G.; Pedersen, C. M.; Qiao, Y.; lin Hou, X.; xiong Wang, Y. Graphene oxide: a novel acid catalyst for the synthesis of 2,5-dimethyl-N-phenyl pyrrole by the Paal-Knorr condensation. *New Carbon Materials* **2017**, *32*, 160 – 167.

[54] Wong, H.-S. P. *Carbon Nanotube and Graphene Device Physics*, 1st ed.; Cambridge University Press, 2010.

[55] Sasha Stankovich, G. H. B. D. K. M. K. E. J. Z. E. A. S. R. D. P. S. T. N. . R. S. R., Dmitriy A. Dikin Graphene-based composite materials. *Nature* **2006**, *442*, 282–286.

[56] Chen, H.; Müller, M. B.; Gilmore, K. J.; Wallace, G. G.; Li, D. Mechanically strong, electrically conductive, and biocompatible graphene paper. *Advanced Materials* **2008**, *20*, 3557–3561.

[57] Park, S.; Dikin, D. A.; Nguyen, S. T.; Ruoff, R. S. Graphene Oxide Sheets Chemically Cross-Linked by Polyallylamine. *The Journal of Physical Chemistry C* **2009**, *113*, 15801–15804.

[58] Cheng, Q.; Wu, M.; Li, M.; Jiang, L.; Tang, Z. Ultratough Artificial Nacre Based on Conjugated Cross-linked Graphene Oxide. *Angewandte Chemie International Edition* **2013**, *52*, 3750–3755.

[59] Brodie, B. C. XIII. On the atomic weight of graphite. *Philosophical Transactions of the Royal Society of London* **1859**, 249–259.

[60] Staudenmaier, L. Verfahren zur darstellung der graphitsäure. *Berichte der deutschen chemischen Gesellschaft* **1898**, *31*, 1481–1487.

[61] Hummers Jr, W. S.; Offeman, R. E. Preparation of graphitic oxide. *Journal of the american chemical society* **1958**, *80*, 1339–1339.

[62] others,, *et al.* Silver nanoparticles: synthesis, properties, toxicology, applications and perspectives. *Advances in Natural Sciences: Nanoscience and Nanotechnology* **2013**, *4*, 033001.

[63] Panáček, A.; Kvitek, L.; Prucek, R.; Kolář, M.; Večeřová, R.; Pizúrová, N.; Sharma, V. K.; NevěcÌŇná, T. â.; Zbořil, R. Silver colloid nanoparticles: synthesis, characterization, and their antibacterial activity. *The Journal of Physical Chemistry B* **2006**, *110*, 16248–16253.

[64] Li, A.; Liu, J.; Liu, G.; Zhang, J.; Feng, S. Design and synthesis of fluorescent core–shell nanoparticles with tunable lower critical solution temperature behavior and metal-enhanced fluorescence. *Journal of Polymer Science Part A: Polymer Chemistry* **2014**, *52*, 87–95.

[65] Henglein, A.; Giersig, M. Formation of colloidal silver nanoparticles: capping action of citrate. *The Journal of Physical Chemistry B* **1999**, *103*, 9533–9539.

[66] Raether, H. *Surface plasmons on smooth and rough surfaces and on gratings*; Springer, 1988; pp 4–39.

[67] Willets, K. A.; Van Duyne, R. P. Localized surface plasmon resonance spectroscopy and sensing. *Annu. Rev. Phys. Chem.* **2007**, *58*, 267–297.

[68] Maier, S. A. *Plasmonics: fundamentals and applications*; Springer Science & Business Media, 2007.

[69] Rodríguez-Sánchez, L.; Blanco, M. C.; López-Quintela, M. Electrochemical Synthesis of Silver Nanoparticles. *The Journal of Physical Chemistry B* **2000**, *104*.

[70] Seney, C. S.; Gutzman, B. M.; Goddard, R. H. Correlation of Size and Surface-Enhanced Raman Scattering Activity of Optical and Spectroscopic Properties for Silver Nanoparticles. *J. Phys. Chem. C.* **2009**, *113*, 74–80.

[71] Shi, W.; Ma, Z. Amperometric glucose biosensor based on a triangular silver nanoprisms/chitosan composite film as immobilization matrix. *Biosensors and Bioelectronics* **2010**, *26*, 1098 – 1103.

[72] Xu, R.; Wang, D.; Zhang, J.; Li, Y. Shape-Dependent Catalytic Activity of Silver Nanoparticles for the Oxidation of Styrene. *Chemistry - An Asian Journal* **2006**, *1*, 888–893.

[73] Zhang, Q.; Hu, Y.; Guo, S.; Goebl, J.; Yin, Y. Seeded growth of uniform Ag nanoplates with high aspect ratio and widely tunable surface plasmon bands. *Nano letters* **2010**, *10*, 5037–5042.

[74] Tao, A. R.; Habas, S.; Yang, P. Shape control of colloidal metal nanocrystals. *small* **2008**, *4*, 310–325.

[75] Rocha, T. C.; Winnischofer, H.; Westphal, E.; Zanchet, D. Formation kinetics of silver triangular nanoplates. *The Journal of Physical Chemistry C* **2007**, *111*, 2885–2891.

[76] Hári, J.; Pukánszky, B. In *Applied Plastics Engineering Handbook*; Kutz, M., Ed.; Plastics Design Library; William Andrew Publishing: Oxford, 2011; pp 109 – 142.

[77] Puglia, D.; Kenny, J. In *Thermosets (Second Edition)*, second edition ed.; Guo, Q., Ed.; Elsevier, 2018; pp 231 – 276.

[78] Wen, C.; Shao, M.; Zhuo, S.; Lin, Z.; Kang, Z. Silver/graphene nanocomposite: Thermal decomposition preparation and its catalytic performance. *Materials Chemistry and Physics* **2012**, *135*, 780–785.

[79] Huang, K.-J.; Wang, L.; Wang, H.-B.; Gan, T.; Wu, Y.-Y.; Li, J.; Liu, Y.-M. Electrochemical biosensor based on silver nanoparticles–polydopamine–graphene nanocomposite for sensitive determination of adenine and guanine. *Talanta* **2013**, *114*, 43–48.

[80] Huang, L.; Hou, K.; Jia, X.; Pan, H.; Du, M. Preparation of novel silver nanoplates/graphene composite and their application in vanillin electrochemical detection. *Materials Science and Engineering* **2014**, *38*, 39–45.

[81] Ren, W.; Fang, Y.; Wang, E. A Binary Functional Substrate for Enrichment and Ultrasensitive SERS Spectroscopic Detection of Folic Acid Using Graphene Oxide/Ag Nanoparticle Hybrids. *ACS Nano* **2011**, *5*, 6425–6433, PMID: 21721545.

[82] Xiong, S.; Xi, B.; Zhang, K.; Chen, Y.; Jiang, J.; Hu, J.; Zeng, H. C. Ag nanoprisms with Ag 2 S attachment. *Scientific reports* **2013**, *3*, 2177.

[83] Usman, M.; Pan, L.; Sohail, A.; Mahmood, Z.; Cui, R. Fabrication of 3D vertically aligned silver nanoplates on nickel foam-graphene substrate by a novel electrodeposition with sonication for efficient supercapacitors. *Chemical Engineering Journal* **2017**, *311*, 359–366.

[84] Prasad, N. E.; Wanhill, R. J. *Aerospace materials and material technologies*; Springer, 2017; Vol. 3.

[85] K, P.; Toshiaki, E.; R, R. *Graphene And Its Fascinating Attributes*; World Scientific Publishing Company, 2011.

[86] Pensoft.net, tem—transmission-electron-microscopy. `http://nanofase.eu/show/tem---transmission-electron-microscopy_1454/`.

[87] Wikipedia contributors, Transmission electron microscopy — Wikipedia, The Free Encyclopedia. 2020; `https://en.wikipedia.org/w/index.php?title=Transmission_electron_microscopy&oldid=935086092`, [Online; accessed 10-January-2020].

[88] Commons, W. File:Schematic of UV- visible spectrophotometer.png — Wikimedia Commons, the free media repository. 2016; `https://commons.wikimedia.org/w/index.php?title=File:Schematic_of_UV-_visible_spectrophotometer.png&oldid=218744938`, [Online; accessed 7-February-2020].

[89] PERKAMPUS, H.-H. *Uv-vis Spectroscopy and Its Applications*; Springer, 1992.

[90] Smith, E.; Dent., G. *Modern Raman Spectroscopy - A Practical Approach*; John Wiley Sons, 2005.

[91] Hung, P.-S.; Kuo, Y.-C.; Chen, H.-G.; Chiang, H.-H. K.; Lee, O. K.-S. Detection of osteogenic differentiation by differential mineralized matrix production in mesenchymal stromal cells by Raman spectroscopy. *PloS one* **2013**, *8*.

[92] Wikipedia contributors, Raman spectroscopy — Wikipedia, The Free Encyclopedia. 2020; `https://en.wikipedia.org/w/index.php?title=Raman_spectroscopy&oldid=935025654`, [Online; accessed 10-January-2020].

[93] others,, *et al.* Large-scale exfoliation of inorganic layered compounds in aqueous surfactant solutions. *Advanced materials* **2011**, *23*, 3944–3948.

[94] Khalil, M.; Wang, S.; Yu, J.; Lee, R. L.; Liu, N. Electrodeposition of iridium oxide nanoparticles for pH sensing electrodes. *Journal of The Electrochemical Society* **2016**, *163*, B485–B490.

[95] Bard, A. J.; Faulkner, L. R. *Electrochemical Methods Fundamentals and Applications*; John Wiley & Sons, 2001.

[96] Skoog, F. C. S., D.; Holler *Principles of Instrumental Analysis*; Cengage Learning; 6 edition, 2006.

[97] Elgrishi, N.; Rountree, K. J.; McCarthy, B. D.; Rountree, E. S.; Eisenhart, T. T.; Dempsey, J. L. A practical beginnerâĂŹs guide to cyclic voltammetry. *Journal of Chemical Education* **2018**, *95*, 197–206.

[98] Faulkner, L. R.; Bard, A. J. *Electrochemical methods: fundamentals and applications*; John Wiley and Sons, 2002.

[99] Savéant, J.-M. Elements of molecular and biomolecular electrochemistry. *Willey-VCH, New Jersey* **2006**,

[100] Elgrishi, N.; McCarthy, B. D.; Rountree, E. S.; Dempsey, J. L. Reaction pathways of hydrogen-evolving electrocatalysts: Electrochemical and spectroscopic studies of proton-coupled electron transfer processes. *ACS Catalysis* **2016**, *6*, 3644–3659.

[101] Marcano, D. C.; Kosynkin, D. V.; Berlin, J. M.; Sinitskii, A.; Sun, Z.; Slesarev, A.; Alemany, L. B.; Lu, W.; Tour, J. M. Improved synthesis of graphene oxide. *ACS nano* **2010**, *4*, 4806–4814.

[102] Li, D.; Müller, M. B.; Gilje, S.; Kaner, R. B.; Wallace, G. G. Processable aqueous dispersions of graphene nanosheets. *Nature nanotechnology* **2008**, *3*, 101.

[103] Kaniyoor, A.; Ramaprabhu, S. A Raman spectroscopic investigation of graphite oxide derived graphene. *Aip Advances* **2012**, *2*, 032183.

[104] Jing, C.; Fang, Y. Experimental (SERS) and theoretical (DFT) studies on the adsorption behaviors of L-cysteine on gold/silver nanoparticles. *Chemical physics* **2007**, *332*, 27–32.

[105] Jorio, A.; Ferreira, E. H. M.; Moutinho, M. V. O.; Stavale, F.; Achete, C. A.; Capaz, R. B. Measuring disorder in graphene with the G and D bands. *Phys. Status Solidi* **2010**, *11-12*, 2980–2982.